Study of the multi-strange resonance $\Xi(1530)^0$ production with ALICE at the LHC energies

Jihye Song

Contents

List of Figures **4**

List of Tables **8**

1 The physics of relativistic heavy-ion collisions **9**
1.1 Standard model . . . 9
1.2 QCD and Quark-Gloun plasma . . . 10
1.3 Heavy Ion Collisions . . . 15

2 Theoretical models **17**
2.1 Thermal statistical model . . . 17
2.1.1 Calculations . . . 19
2.1.2 Results and comparison with data . . . 19
2.2 EPOS, UrQMD . . . 21

3 Production of resonance with strangeness **23**
3.1 Strange quark and hyperons . . . 25
3.2 Resonance production . . . 27

4 A Large Ion Collider Experiment at the LHC **29**
4.1 The Large Hadron Collider . . . 29
4.2 The ALICE project . . . 32
4.2.1 ALICE detector . . . 32
4.2.2 Data Acquisition (DAQ) and trigger system . . . 42
4.2.3 ALICE offline software frame work . . . 44

5 Measurement of $\Xi(1530)^0$ production in p–Pb and Pb-Pb **46**
5.1 $\Xi(1530)^0$ -reconstruction . . . 46
5.1.1 Data sample and event selection . . . 46
5.1.2 Track and topological selection . . . 50
5.1.3 Particle identification . . . 53
5.1.4 Signal extraction . . . 56
5.2 Efficiency correction . . . 65
5.3 Corrected p_{T}-spectra . . . 68
5.4 Systematic uncertainties . . . 70
5.5 $\Xi(1530)^0$ transverse momentum spectra . . . 75

6 Further results and discussion **78**
6.1 Mean transverse momentum . . . 78
6.2 Particle yield ratios . . . 82

6.2.1 Integrated yield ratios of excited to ground-state hadrons 82
6.3 Integrated yield ratios to pion 85

References **89**

List of Figures

1 QCD coupling constant as a function of momentum transfer. Experimental data and also theoretical prediction are presented. [1] 13
2 Hydrodynamic evolution of a heavy ion collision with and without the formation of a QGP. 16
3 Grand canonical thermal fit of 0-10% central Pb-Pb collisions, with 3 models (THERMUS, GSI, SHARE). Excluded volume correction implemented in THERMUS and GSI with rh = 0.3 fm μ_B fixed to 0, γ_s fixed to 1, γ_c fixed to 20 (THERMUS and GSI) 17
4 Ratio of baryonic and mesonic resonances over their stable partner as a function of temperature. 20
5 Ratio of resonances over their stable partner as a function of $\sqrt{(s)}$. 21
6 The $J^P = 1/2^+$ ground state baryon octet 24
7 The $J^P = 3/2^+$ baryon decuplet 24
8 Enhancements in the rapidity range $|y|$ <0.5 as a function of the mean number of participants $\langle N_{part} \rangle$, showing LHC (ALICE, full symbols), RHIC and SPS (open symbols) data. Boxes on the dashed line at unity indicate statistical and systematic uncertainties on the pp or p-Be reference. Error bars on the data points represent the corresponding uncertainties for all the heavy-ion measurements and those for p–Pb at the SPS. 26
9 Hadronic phase 27
10 The CERN accelerator complex [2] 30
11 The ALICE detector 34
12 Schematic view of the ITS [3] 35
13 Track impact parameter resolution in the transverse plane (rϕ) vs $p_{\mathrm{T}}$for charged particle 36
14 Schematic view of the TPC 37
15 Specific energy loss (dE/dx) in the TPC vs. particle momentum in Pb–Pb collisions at $\sqrt{s_{\mathrm{NN}}}$= 2.76 TeV. The lines show the parametrisations of the expected mean energy loss. 38
16 Correlation between the sum and difference of signal times in V0A and V0C. Three classes of events collisions at (8.3 ns, 14.3 ns), background from Beam 1 at (-14.3 ns, -8.3 ns), and background from Beam 2 at (14.3 ns, 8.3 ns) can be clearly distinguished. 40
17 Distribution of the V0 amplitude (sum of V0A and V0C in top, V0A in bottom). The inset shows a magnified version of the most peripheral region. 41
18 The overall architecture of the ALICE DAQ and the interface to the HLT system. 42
19 Schematic view of the AliRoot framework 45

20 Vertex-z coordinate distribution of the accepted events in p–Pb collision(Left) and in Pb–Pb collisions(Right). The red dashed line indicates vertex cut . 48
21 Multiplicity distribution of accepted events in p–Pb collision in percentile. The each color and labels define the four intervals in which the analysis in performed. 48
22 Centrality distribution of three different trigger classes. 49
23 Sketch of the decay modes for Ξ^{*0} and depiction of the track and topological selection criteria. 51
24 TPC $\mathrm{d}E/\mathrm{d}x$ as function of transverse momentum for total (top) and selected first emitted π in 3σ (bottom) 53
25 TPC $\mathrm{d}E/\mathrm{d}x$ as function of transverse momentum for total (top) and selected second emitted π in 3σ(bottom) 53
26 TPC $\mathrm{d}E/\mathrm{d}x$ as function of transverse momentum for total (top) and selected last emitted π in 3σ(bottom) 54
27 TPC $\mathrm{d}E/\mathrm{d}x$ as function of transverse momentum for total (top) and selected proton in 3σ(bottom) 54
28 TPC $\mathrm{d}E/\mathrm{d}x$ as function of transverse momentum for total (top) and selected first emitted π in 3σ (bottom) 54
29 TPC $\mathrm{d}E/\mathrm{d}x$ as function of transverse momentum for total (top) and selected second emitted π in 3σ(bottom) 55
30 TPC $\mathrm{d}E/\mathrm{d}x$ as function of transverse momentum for total (top) and selected last emitted π in 3σ(bottom) 55
31 TPC $\mathrm{d}E/\mathrm{d}x$ as function of transverse momentum for total (top) and selected proton in 3σ(bottom) 56
32 The $\Xi^{\mp}\pi^{\pm}$ invariant mass distribution (Same-event pairs) in $1.8< p_{\mathrm{T}}<2.2$ GeV/c and for the multiplicity class 20-40%. The background shape, using pairs from different events (Mixed-event background), is normalised to the counts in $1.49 < M_{\Xi\pi} < 1.51$ GeV/c^2 and $1.56 < M_{\Xi\pi} < 1.58$ GeV/c^2 57
33 The $\Xi^{\mp}\pi^{\pm}$ invariant mass distribution (Same-event pairs) in $3.0< p_{\mathrm{T}}<3.5$ GeV/c and for the centrality class 0-10%. The background shape, using pairs from different events (Mixed-event background), is normalised to the counts in $1.49 < M_{\Xi\pi} < 1.51$ GeV/c^2 and $1.56 < M_{\Xi\pi} < 1.58$ GeV/c^2 58
34 The invariant mass distribution after subtraction of the mixed-event background in p–Pb collisions. The solid curve represents the combined fit, while the dashed line describes the residual background. 59
35 The invariant mass distribution after subtraction of the mixed-event background in Pb–Pb collisions. The solid curve represents the combined fit, while the dashed line describes the residual background. 60
36 σ fit parameters as a function of p_{T}in MB in p–Pb collisions (top) and in Pb–Pb collisions (bottom). 62

37 $\Xi(1530)^0$ -mass obtained from fit of the Voigtian peak as a function of p_{T}in each multiplicity classes in p–Pb collisions (top) and the different centrality classes in Pb–Pb (bottom). 63
38 $\Xi(1530)^0$ -raw spectra obtained from fit of the Voigtian peak and a polynomial residual background for different multiplicities in p–Pb collisions (top) and Pb–Pb collisions (bottom). Only the statistical error is reported. 64
39 $\Xi(1530)^0$ -raw spectra obtained from fit of the Voigtian peak and a polynomial residual background for different multiplicities. Only the statistical error is reported. 65
40 Real corrected $\Xi(1530)^0$ spectrum (black) for the minimum bias with Levy fit (black curve). Also shown are the unweighted generated (blue) and reconstructed (red) $\Xi(1530)^0$ spectra. 66
41 Efficiency as a function of p_{T}in minimum bias events in p–Pb collisions. . . 67
42 Efficiency as a function of p_{T}in different centrality classes in Pb–Pb collisions 68
43 Corrected p_{T}-spectra of $\Xi(1530)^0$ in NSD and different multiplicity classes in p–Pb collisions. 69
44 Corrected p_{T}-spectra of $\Xi(1530)^0$ in different centrality classes in Pb-Pb collisions. 69
45 Summary of the contributions to the systematic uncertainty in minimum bias events in p–Pb collisions. The dashed black line is the sum in quadrature of all the contributions. 73
46 Systematic uncertainties for each multiplicity classes in p–Pb collisions. . . 73
47 Summary of the contributions to the systematic uncertainty in minimum bias events in Pb–Pb collisions. The dashed black line is the sum in quadrature of all the contributions. 74
48 Systematic uncertainties for each multiplicity classes. 74
49 Corrected yields as function of p_{T} in NSD events and multiplicity dependent event classes in p–Pb collision system. Statistical uncertainties are presented as bar and systematical uncertainties are plotted as boxes. 76
50 Corrected yields as function of p_{T} in different centrality classes in Pb–Pb collision system. Statistical uncertainties are presented as bar and systematical uncertainties are plotted as boxes. 77
51 Mean transverse momenta $\langle p_{\mathrm{T}} \rangle$ of Λ, Ξ^-, $\Sigma^{*\pm}$, Ξ^{*0} and Ω^- in p–Pb collisions at $\sqrt{s_{\mathrm{NN}}}$= 5.02 TeV as a function of mean charged-particle multiplicity density $\langle \mathrm{d}N_{\mathrm{ch}}/\mathrm{d}\eta_{\mathrm{lab}} \rangle$, measured in the pseudorapidity range $\mid \eta_{\mathrm{lab}} \mid < 0.5$. The results for Λ, Ξ^- and Ω^- are taken from [4, 5, 6]. Statistical and systematic uncertainties are represented as bars and boxes, respectively. The Ω^- and Ξ^- points in the 3rd and 4th lowest multiplicity bins are slightly displaced along the abscissa to avoid superposition with the $\Xi(1530)^0$ points. 79

52 Mass dependence of the mean transverse momenta of identified particles for the $0-20\%$ V0A multiplicity class and with $-0.5 < y_{\mathrm{CMS}} < 0$ in p–Pb collisions at $\sqrt{s_{\mathrm{NN}}}$= 5.02 TeV [4, 6], and in minimum-bias pp collisions at $\sqrt{s} = 7$ TeV [7] with $|y_{\mathrm{CMS}}| < 0.5$. Additionally, D^0 and J/ψ results are plotted. The D^0 and J/ψ were measured in different rapidity ranges: $|y_{\mathrm{CMS}}| < 0.5$ [8] ($|y_{\mathrm{CMS}}| < 0.9$ [9]) for D^0 (J/ψ) in pp and $-0.96 < y_{\mathrm{CMS}} < 0.04$ [8] ($-1.37 < y_{\mathrm{CMS}} < 0.43$ [10]) for D^0 (J/ψ) in p–Pb. Note also that the results for D^0 and J/ψ in p-Pb collisions are for the 0-100% multiplicity class. 80

53 Ratio of $\Xi(1530)^0$ to Ξ^- measured in pp [7], p–Pb [4, 6] and Pb–Pb collisions as a function of $\langle \mathrm{d}N_{\mathrm{ch}}/\mathrm{d}\eta_{\mathrm{lab}} \rangle$ measured at midrapidity. Statistical uncertainties (bars) are shown as well as total systematic uncertainties (hollow boxes) and systematic uncertainties uncorrelated across multiplicity (shaded boxes). A few model predictions are also shown as lines at their appropriate abscissa. 83

54 Ratio of ρ/π(Up), K*/K, ϕ/K(Left bottom) and $\Lambda*/\Lambda$ with system size measured at mid-rapidity. Statistical uncertainties (bars) are shown as well as total systematic uncertainties (hollow boxes) and systematic uncertainties uncorrelated across multiplicity (shaded boxes). A few model predictions are also shown as lines at their appropriate abscissa. 84

55 Ratio of $\Xi(1530)^0$ to $\pi^{\pm}$, measured in pp [11] and p–Pb [7] collisions, as a function of the average charged particle density ($\langle \mathrm{d}N_{\mathrm{ch}}/\mathrm{d}\eta_{\mathrm{lab}} \rangle$) measured at mid-rapidity. Statistical uncertainties (bars) are shown as well as total systematic uncertainties (hollow boxes) and systematic uncertainties uncorrelated across multiplicity (shaded boxes). A few model predictions are also shown as lines at their appropriate abscissa. 86

56 Particle yield ratios to pions of strange and multi-strange hadrons normalized to the values measured in pp collisions, both in pp and in p–Pb collisions. The common systematic uncertainties cancel in the double-ratio. The empty boxes represent the remaining uncorrelated uncertainties. The lines represent a simultaneous fit of the results with the empirical scaling formula in Equation **??**. 87

57 p_{T}-integrated yield ratios of strange and multi-strange hadrons to $(\pi^+ + \pi^-)$ as a function of $\langle \mathrm{d}N_{\mathrm{ch}}/\mathrm{d}\eta_{\mathrm{lab}} \rangle$ measured in the rapidity interval $|\eta| < 0.5$. The empty and dark-shaded boxes show the total systematic uncertainty and the contribution uncorrelated across multiplicity bins, respectively. The values are compared to calculations from MC models and to results obtained in Pb–Pb and p–Pb collisions at the LHC. 88

List of Tables

1 Constituents of matter in the Standard Model 9
2 Fundamental forces 10
3 Parameters used in the thermal-model calculations. 18
4 Properties of particles used in the ratio calculations. 19
5 Difference of mass (ΔM), baryon number (ΔB), strangeness (ΔS) and charge (ΔQ) of the ratios. The values of the slopes needs to be checked!!!! . 21
6 Quantum numbers and masses associated to the three lighter quarks: u, d and s 23
7 Lifetime of hadronic resonances 25
8 Number of accepted and analyzed events per multiplicity/centrality interval 50
9 Track selections common to all decay daughters and primary track selections applied to the charged pions from decays of Ξ^{*0}. 50
10 Topological and track selection criteria. 51
11 Summary of the systematic uncertainties on the differential yield, $\mathrm{d}^2N/(\mathrm{d}p_\mathrm{T}\mathrm{d}y)$. Minimum and maximum values in all p_T intervals and multiplicity classes in p–Pb, centrality classes in Pb–Pb are shown for each source. 75

1 The physics of relativistic heavy-ion collisions

The main objective of relativistic heavy ion physics is to study the nuclear matter under extreme conditions which are high temperature and energy density. In these conditions, the Standard Model anticipates that the nuclear matter undergo a new phase, where the quarks and the gluons are expected to be de-confined called quark-gluon plasma (QGP) and to freely move.

1.1 Standard model

If one have question "what the world is made of", our current answer to the question is Standard Model (SM) families [12] reported in Table 1. The SM explains the way how those basic blocks of matter interact and how they are ruled by four fundamental forces. In this explanation, the matter consist of 12 particles, which have a spin of 1/2 (fermions) and can be categorized in accordance with way how they interact or equivalently to what charges they carry. The basic particles are six quarks (up, down, charm, strange, top and bottom) that carry fractional charge of $+\frac{2}{3}e$ or $-\frac{1}{3}e$, and six leptons (electron, electron neutrino, muon, muon neutrino, tau, tau neutrino) with integer charge.

	Quaks			Leptons		
Family	Name	Charge[e]	Mass	Name	Charge[e]	Mass
1	u	2/3	$2.2^{+0.6}_{-0.4}$ MeV/c^2	e^-	$-e$	0.511 MeV/c^2
	d	-1/3	$4.7^{+0.5}_{-0.4}$ MeV/c^2	ν_e	0	$<$ 2 eV/c^2
2	c	2/3	$1.27^{\pm 0.03}$GeV/c^2	μ^-	$-e$	105.66 MeV/c^2
	s	-1/3	96^{+8}_{-4}MeV/c^2	ν_μ	$-e$	$<$ 0.19 eV/c^2
3	t	2/3	173.21$\pm$1.22GeV/c^2	τ^-	$-e$	1.777 GeV/c^2
	b	-1/3	$4.18^{+0.04}_{-0.03}$GeV/c^2	ν_τ	$-e$	$<$ 18.2 MeV/c^2

Table 1: Constituents of matter in the Standard Model

The interactions between elementary particles are described by the exchange of gauge bosons(gluon, photon, Z-boson, W-boson), reported in Table 2 together with their relative coupling strengths. The leptons are governed the weak force and the electromagnetic force. Quarks have color property which is the character of charge in the strong force. The color could take one out of three possible values (conventionally red, green and blue). The color can not be appeared freely. After they are confined they come out in the form of hadron which are colorless. Further explaination on color is described in Section 1.2. Then, the hadrons are grouped into baryon and mesons. Baryons consist of three quarks, qqq or $(\bar{q}\bar{q}\bar{q})$ while mesons consist of two quarks $(q\bar{q})$.

The models that describe these interactions are listed as follows:

Force	Strength	Gauge Boson(s)	Applies on
Strong force	1	8 Gluons(g)	Quarks, gluons
Electromagetic force	$\simeq 10^{-2}$	Photon (γ)	All charged particles
Weak force	$\simeq 10^{-7}$	$W^{\pm}$, Z^0	Quarks, leptons
Gravitation	$\simeq 10^{-39}$	Gravitons	All particles

Table 2: Fundamental forces

Quantum Electro-Dynamics (QED) is a quantum field theory of the electromagnetic force and describes how light and matter interact. This is the first theory where full agreement between quantum mechanics and special relativity is achieved. It explains mathematically not only all interactions of light with matter but also those of charged particles with one another.

Electroweak Theory (EW) is the unified description of two of the four known fundamental interactions of nature: electromagnetism and the weak interaction. The first measurement of the existence of the weak bosons W^+, W^- and Z^0 was performed in 1983, when they were produced and directly observed in S$p\bar{p}$S collisions at CERN.

Quantum Chromo-dynamics (QCD) is the theory of the strong interaction (color force), describing the interactions between quarks and gluons which make up the hadrons. Starting from the classification of the large amount of particles discovered during the fifties, the original idea of the quark model by Gell-Mann (Nobel Prize in 1969) has been developed during the sixties until 1973, when David J. Gross, H. David Politzer and Frank Wilczek discovered the asymptotic freedom property of the strong nuclear interaction.

1.2 QCD and Quark-Gloun plasma

As the number of known particle species became large, the idea that these could be the elementary constituents of matter was replaced by the notion that these species could in fact be composite objects made up of fewer, more elementary particles, in a similar way to what had already happened to the elements of Mendeleev's Periodic Table. The original idea by Gell-Mann (1964) was that the hadrons could be obtained as combination of the fundamental representation of an $SU_f(3)$ group, where three different flavors of quark (q = u, d, s) combine to build mesons ($q\bar{q}$) and hadrons (qqq). However, when cataloging hadrons using the $SU_f(3)$ group, there are anomalous states, such as the Ω^-(sss) and the Δ^{++}(uuu), that are combinations of three quarks of the same flavor, in clear contrast with the Pauli exclusion principle for fermions. A solution was proposed in 1965 by Moo-Young Han with Yoichiro Nambu and Oscar W. Greenberg, who independently solved the problem by proposing that quarks possess an additional SU(3) gauge quantum number,

later called color charge. This new quantum number may assume three states, represented by the three primary colors: red, green and blue (denoted symbolically by R, G and B, respectively). The introduction of this new quantum number also provides an explanation to other empirical evidence, such as the fact that no qq, $\bar{q}q$ or the single quark have never been observed directly. On the other hand, the existence of color charge gives rise to the possible existence of differently colored states for each particle. Thus, we could have many states for the proton, such as $\mathrm{u}_R\mathrm{u}_G\mathrm{d}_B$, $\mathrm{u}_R\mathrm{u}_G\mathrm{d}_G$, $\mathrm{u}_B\mathrm{u}_R\mathrm{d}_R$, and so on. The fundamental rule that solves such contradictions is that all the particle states observed in nature are "colorless" or "white" (or, to be more precise, unchanged under $\mathrm{SU}_c(3)$ rotations). The dynamics of the quarks and gluons are controlled by the gauge invariant QCD Lagrangian:

$$\mathcal{L}_{QCD} = \underbrace{i\delta_{ij}\bar{\Psi}_q^i\gamma^\mu\partial_\mu\Psi_q^j}_{\mathcal{L}_1} + \underbrace{g_s\bar{\Psi}_q^i\gamma^\mu t_{ij}^a A_\mu^a\Psi_q^j}_{\mathcal{L}_2} + \underbrace{m_q\bar{\Psi}_q^i\Psi_q^j}_{\mathcal{L}_3} + \underbrace{\frac{1}{4}F_{\mu\nu}^a F^{a\mu\nu}}_{\mathcal{L}_4} \tag{1}$$

where the coloured gluon field tensor, $F_{\mu\nu}^a$ (with color index a) and the squared gauge coupling parameter, g_s^2 (associated to the strong coupling constant α_s) are defined as:

$$F_{\mu\nu}^a = \partial_\mu A_\nu^a - \partial_\nu A_\mu^a + g_s f^{abc} A_\mu^b A_\nu^c \tag{2}$$

and

$$g_s^2 = 4\pi\alpha_s \tag{3}$$

where:

- Ψ_q^i: the quark field with flavor q and color index i $\in$ [1;3], such as $\Psi_q = (\Psi_{qR}, \Psi_{qG}, \Psi_{qB})^T$ and A_μ^a is the gluon field with color index a (adjoint representation)
- γ^μ: Dirac matrices that express the vector nature of the strong interaction, with μ being the Lorentz vector associated index
- m_q: quark mass, a priori not equal to zero (resulting from the Higgs mechanism or equivalent)
- t_{ij}^a: generator matrices of the group $\mathrm{SU}_c(3)$, proportional to the Gell-Mann matrices, that perform revolutions in color space, representing interaction of quarks and gluons
- f^{abc}: structure constant of QCD

Each of the four terms of the QCD Lagrangian expresses and aspect of the interaction, specifically:

- $\mathcal{L}_1$: gives the kinetic energy of the quark field Ψ_q^i

- $\mathcal{L}_2$: gives the interaction between quarks (fermions) and gluons (the bosons of the interaction)
- $\mathcal{L}_3$: gives the mass of the quarks
- $\mathcal{L}_4$: gives the kinetic energy of the gluons

The terms of this equation, together with the fundamental parameters α_s and m_q, summarize in just one expression all the features of the strong interaction. The first three terms describe the free propagation of quarks and gluons and the quark-gluon interaction. The remaining two terms show the presence of three and four gluon vertices in QCD and reflect the fact that gluons themselves carry color charge. This is a consequence of the non-abelian4 character of the gauge group. This peculiarity of the QCD interaction imposes the evolution of the strong coupling constant, α_s. The corresponding trend has been measured experimentally, and compared in Figure 1 with predictions. A practical consequence of this behavior is that the corresponding potential has a completely different shape than the other fundamental interactions and can be expressed by the following equation:

$$V(r) = -4\frac{\alpha_s}{3r} + kr \tag{4}$$

where r is the separation distance between the two quarks and k is a constant that is approximately 1 GeV/fm.

Three are main properties of the QCD interaction:

Confinement At large distances between quarks and gluons (i.e. small values of transferred momentum Q in Figure 1) the coupling constant is large and the associated force is strong enough to keep these elementary con- stituents (usually called partons) confined in bounded states. As expressed in the Equation 4, the attractive potential increases with the increasing of the relative distance between the two partons preventing the separation of an individual quark or gluon. This explains the meaning of the term "confinement" adopted to describe this energy regime. From the theoretical point of view, the large value of α_s make impossible any perturbative approach in the solution of the Hamilton equation of the system. A successful solution is to perform the study of the system on a discrete space. Such techniques are known as lattice QCD and are based on numerical Monte Carlo simulations. The challenge for the calculations is to reduce the lattice spacing in order to approach the continuum.

Asymptotic freedom Reducing the distance between quarks and gluons (i.e. increasing Q in Figure 1) the coupling constant α_s becomes smaller. As anticipated, this is a unique feature among the forces and comes from the non-abelian nature of the QCD gauge symmetry. Such a phenomenon is also depicted by the weakening of the anti-screening effect of the surround- ing virtual gluons with decreasing distance. In this way two quarks

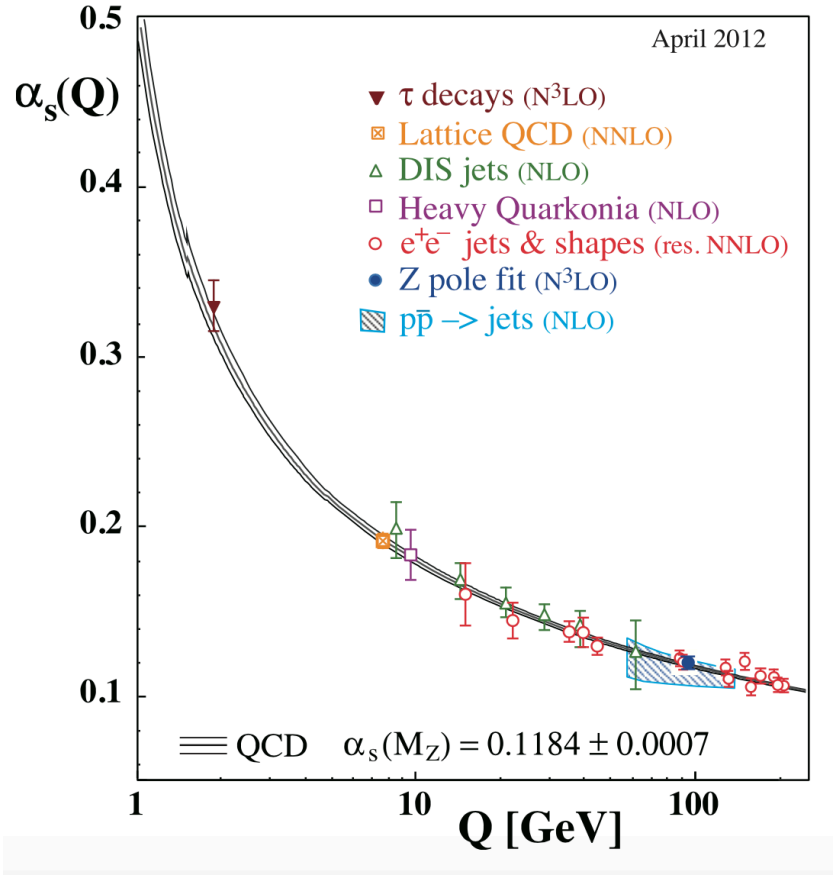

Figure 1: QCD coupling constant as a function of momentum transfer. Experimental data and also theoretical prediction are presented. [1]

closer and closer in space show each other a smaller and smaller color charge.

Chiral symmetry One further property of interest is connected to the chirality of the quark. It can be verified that the QCD lagrangian for massless quarks is invariant under a chiral rotation ($\mathrm{SU}_L(\mathrm{N}_f) \times \mathrm{SU}_R(\mathrm{N}_f)$), while the operator $\bar{q}\mathrm{q} = \bar{q}_L \mathrm{q}_R + \bar{q}_R \mathrm{q}_L$ is not invariant (in the axial part), meaning that the mesons (state $\bar{q}\mathrm{q}$) should have the same mass. Experimentally this is clearly not true, and it could be shown that the axial current is conserved (PCAC and the Goldberger-Treiman relation). The solution to this puzzle is that the chiral (axial-vector) symmetry is spontaneously broken; this means that the symmetry of the Hamiltonian is not a symmetry of the corresponding ground state. It has also been shown, by G. t?Hooft, that the confinement implies a dynamical breaking of the chiral symmetry [7]; this means that the breaking comes from the interaction between the objects in the system. From this follows that the masses of the quarks are strongly increased because of the interaction with the constituents of the system. This mechanism, known as dynamical chiral symmetry breaking justifies the mass of the hadrons, reducing the role of the Higgs mechanism in the mass explanation at least for the light hadrons.

The asymptotic freedom property suggests the existence of a state of matter, called Quark-Gluon Plasma (QGP), in which the constituents of the hadrons are de-confined.

1.3 Heavy Ion Collisions

In the case a QGP is formed, it will eventually expand because of its internal pressure. As the system expands it also cools. The space-time evolution of the expansion can be seen in Figure 2 (right side). A and B represent the two incoming ion beams. After a pre-equilibrium phase a QGP is formed. As it expands, the system will eventually reach what is known as the critical temperature (T_c). At this point partons begin to hadronize and this will continue until the chemical freeze-out (T_{ch}) takes place, when inelastic collisions cease. At this stage the distribution of hadrons is frozen. As cooling and expansion continue the hadrons reach what is called thermal freeze out (T_{fo}). Here the elastic collisions stop and the hadrons carry fixed momenta. The QGP state can not be directly observed, because of its short lifetime. Instead, through experiment we measure the final state hadrons, which have a fixed momentum after T_{fo}. The observables of interest should tell us about the de-confinement and the thermodynamic properties of the matter. Moreover, experimental measurements include yields and p_{T}spectra of various particle species, azimuthal studies of high p_{T}particles, phase space distributions, and particle correlations.

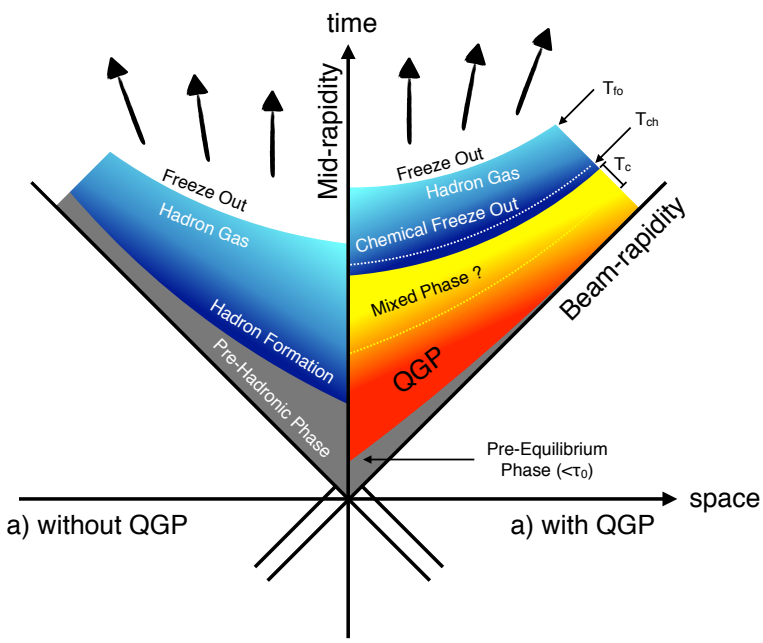

Figure 2: Hydrodynamic evolution of a heavy ion collision with and without the formation of a QGP.

A practical way to reach a critical condition in which a nuclear system should undergo

a phase transition to the QGP, at high temperature and/or matter density, is to collide two nuclei at sufficiently high energy. Therefore, relativistic and ultra-relativistic heavy-ion collisions are a unique tool to study nuclear matter under extreme conditions.

2 Theoretical models

2.1 Thermal statistical model

The statistical-thermal model has proved extremely successful in applications to relativistic collisions of both heavy ions and elementary particles as shown in Figure 3. In light of this success, THERMUS, a thermal model analysis package, has been developed for incorporation into the object-oriented ROOT framework [13].

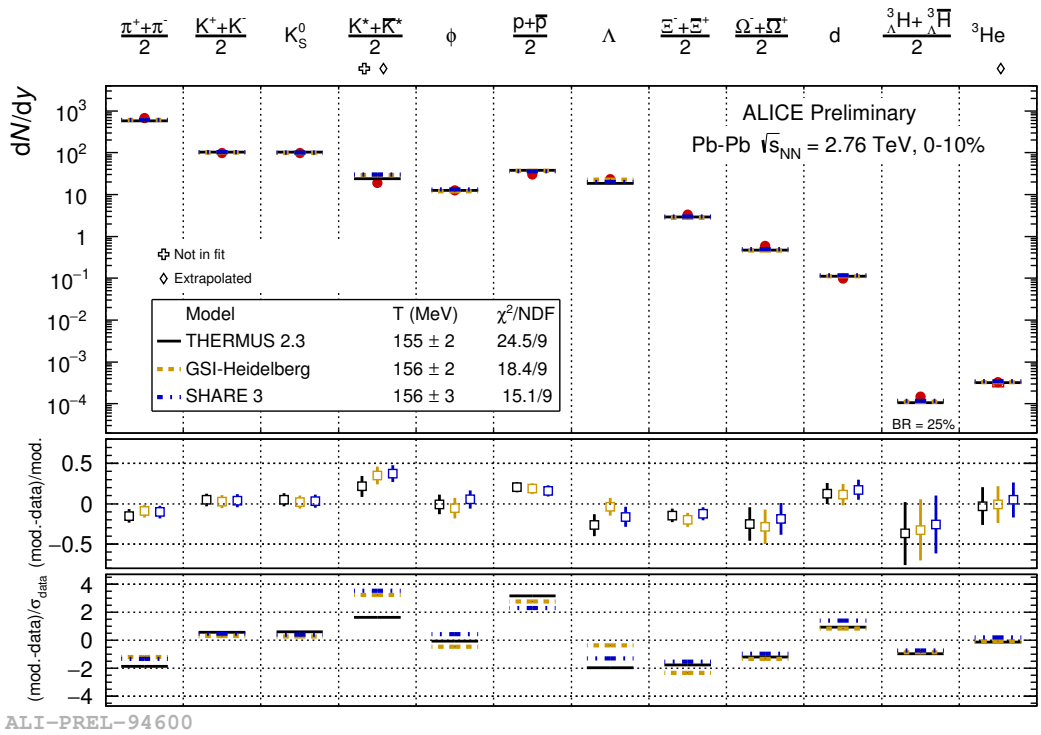

Figure 3: Grand canonical thermal fit of 0-10% central Pb-Pb collisions, with 3 models (THERMUS, GSI, SHARE). Excluded volume correction implemented in THERMUS and GSI with rh = 0.3 fm μ_B fixed to 0, γ_s fixed to 1, γ_c fixed to 20 (THERMUS and GSI)

There are three types of statistical-thermal models in explaining data in high energy nuclear physics and THERMUS treats the system quantum numbers B (baryon number), S (strangeness) and Q (charge) within three distinct formalisms:

1. **Grand-Canonical Ensemble:** Because the hot dense matter produced in nucleus-nucleus collisions is large enough, this ensemble is the most widely used in applications

to heavy-ion collisions, in which the quantum numbers are conserved on average.

2. **Fully-Canonical Ensemble:** In which B, S and Q are each exactly conserved and this ensemble used in high-energy elementary collisions such as pp, $p\overline{p}$ and e^-e^+ collisions.

3. **Strangeness-Canonical Ensemble:** In small systems or at low temperatures, a canonical treatment leads to a suppression of hadrons carrying non-zero quantum numbers, since these particles have to be created in pairs and the resulting low production of strange particles requires a canonical treatment of strangeness.

In order to calculate the thermal properties of a system, one starts with an evaluation of its partition function. The form of the partition function obviously depends on the choice of ensemble. In the present analysis the strangeness-canonical ensemble used and the statistical-thermal model requires six parameters as input: the chemical freeze-out temperature T, baryon and charge chemical potentials μ_B and μ_Q respectively, canonical or correlation radius, R_C; the radius inside which strangeness is exactly conserved and the fireball radius R. An additional strangeness saturation factor γ_S has been used as indicator of a possible departure from equilibrium and $\gamma_S = 1.0$ corresponds to complete strangeness equilibration.

The volume dependence cancels out when studying the particle ratios as well as strangeness canonical equivalent to grand canonical formalism if $\Delta S = 0$ in the ratios and γ_S also cancels out. Parameters used in the analysis listed in Table 3. The μ_B parameter taken from the Ref. [14].

Table 3: Parameters used in the thermal-model calculations.

Parameter	Value
T (MeV)	varied (see text)
μ_B (MeV)	9.2×10^{-2}????
μ_Q (MeV)	0.0
γ_S	1.0

2.1.1 Calculations

Concept:
In order to calculate the particle ratios within strangeness canonical formalism of THERMUS, temperature varied between 60 MeV to 180 MeV and particle yields extracted for each temperature value and then primary particle ratios calculated for each case.

Feed-Down Correction:
Since the particle yields measured by the detectors in collision experiments include feed-down from heavier hadrons and hadronic resonances, the primordial hadrons are allowed to decay to particles considered stable by the experiment before model predictions are compared with experimental data. In the analysis only Λ particles counted as stable (do not allowed to decay) so there is no feed-down contribution from these particles to the other ratios.

Properties of studied particles and their particle ratios listed in Table 4 and Table 5, respectively.

Table 4: Properties of particles used in the ratio calculations.

Particle	Δ^{++}	p	K^{*0}	K^0	K^+	Λ^*	Λ	Σ^{*+}	Σ^+	Σ^0
Mass (MeV/c^2)	1232	938.27	895.92	497.61	493.67	1519.5	1115.68	1382.8	1189.37	1192.6
Width (MeV/c^2)	120	–	50.7	–	–	15.6	–	37.6	–	–
$c\tau$ (fm)	1.6	–	3.9	–	–	12.6	–	5.51	–	–
Ang. Momentum (J)	3/2	1/2	1	1	0	3/2	1/2	3/2	1/2	1/2
Isospin (I)	3/2	1/2	1/2	1/2	1/2	0	0	1	1	1
Parity (P)	+1	+1	-1	-1	0	-1	+1	+1	+1	+1
Strangeness (S)	0	0	1	1	1	-1	-1	-1	-1	-1
Baryon Number (B)	1	1	0	0	0	1	1	1	1	1
Decay Channel	$p\pi^+$	–	π^-	–	$\mu^+\nu_\mu$	pK^-	$p\pi^-$	$\Lambda\pi^+$	$p\pi^0$	$\Lambda\gamma$
Branching Ratio (%)	~ 100	–	~ 66.7	–	~ 63.54	~ 45	~ 63.9	~ 87	~ 51.6	~ 100
Q-Value(MeV/c^2)	154.16	–	262.68	–	–	87.55	37.84	127.55	111.53	76.96

2.1.2 Results and comparison with data

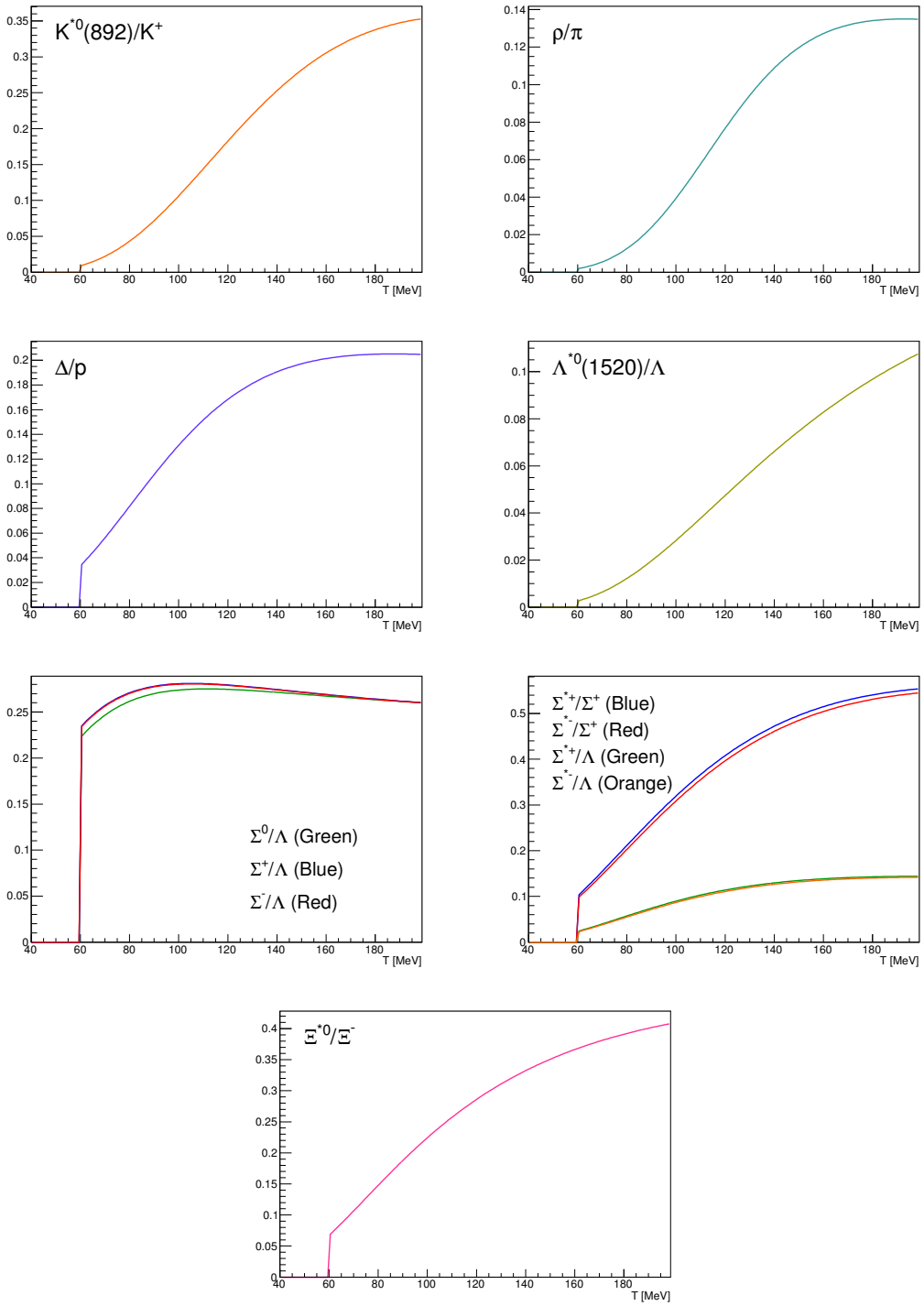

Figure 4: Ratio of baryonic and mesonic resonances over their stable partner as a function of temperature.

Table 5: Difference of mass (ΔM), baryon number (ΔB), strangeness (ΔS) and charge (ΔQ) of the ratios. The values of the slopes needs to be checked!!!!

Particle	Δ^{++}/p	K*/K$^+$	Λ^*/Λ	Σ^{*+}/Λ	Σ^{*+}/Σ^0	Σ^0/Λ	Σ^{*+}/Σ^+	Ξ^{*0}/Ξ^-
ΔM (MeV/c^2)	293.8	402.25	403.82	267.12	190.16	76.96	193.43	210.49
ΔB	0	0	0	0	0	0	0	0
ΔS	0	0	0	0	0	0	0	0
ΔQ	+1	-1	0	+1	0	+1	0	-1
Slope (%) per MeV ??????	0.19	0.76	0.98	0.25	-	-0.08	0.37	0.42

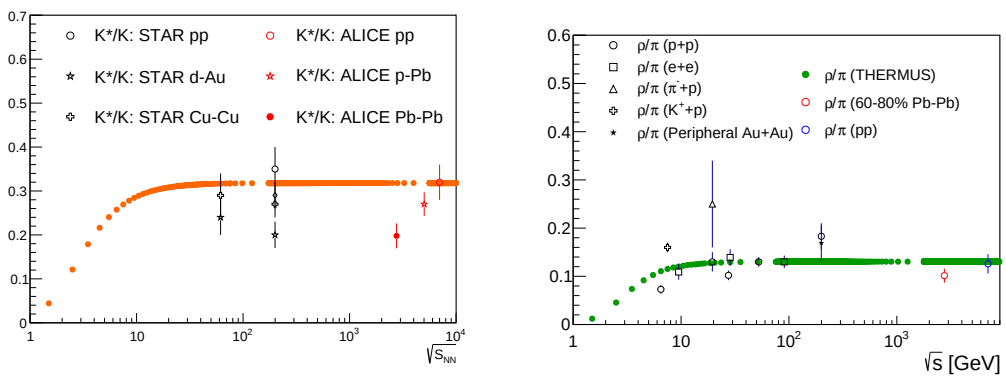

Figure 5: Ratio of resonances over their stable partner as a function of $\sqrt{(s)}$.

2.2 EPOS, UrQMD

The EPOS3 model [15, 16, 17] describes the full evolution of a heavy-ion collision. The initial stage is treated via a multiple-scattering approach based on Pomerons and strings. The reaction volume is divided into a core and a corona part [18]. The core is taken as the initial condition for the QGP evolution, for which one employ viscous hydrodynamics. The corona part is simply composed of hadrons from string decays. After hadronisation of the fluid (core part), these hadrons and as well the corona hadrons are fed into UrQMD [19, 20], which describes hadronic interactions in a microscopic approach. The chemical and kinetic freeze-outs occur within this phase. The chemical freeze-out is expected to occur shortly after the phase transition from partonic to hadronic matter and is followed by the kinetic freeze-out.

As explained in [15, 16, 17, 18], EPOS3 is an event generator based on 3+1D viscous hydrodynamical evolution starting from flux tube initial conditions, which are generated in the Gribov-Regge multiple scattering framework. An individual scattering is referred

to as a Pomeron, identified with a parton ladder, eventually showing up as flux tubes (or strings). Each parton ladder is composed of a pQCD hard process, plus initial and final state linear parton emission. Nonlinear effects are considered by using saturation scales Q_s, depending on the energy and the number of participants connected to the Pomeron in question.

The final state partonic system (corresponding to a Pomeron) amounts to (usually two) color flux tubes, being mainly longitudinal, with transversely moving pieces carrying the $p_{\mathrm{T}}$of the partons from hard scatterings. One has two flux tubes based on the cylindrical topology of the Pomerons. Each quark- antiquark pair in the parton ladder will cut a string into two; in this sense one may have more than two flux tubes. In any case, these flux tubes eventually constitute both bulk matter, also referred to as ?core? (which thermalizes, flows, and finally hadronizes) and jets (also referred to as ?corona?), according to some criteria based on the energy of the string segments and the local string density. For the core, we use a 3+1D viscous hydrodynamic approach, employing a realistic equation of state, compatible with lQCD results. We employ for all calculations in this paper a value of ?/s = 0.08. Whenever a hadronisation temperature of TH is reached, we apply the usual Cooper-Frye freeze-out procedure, to convert the fluid into particles. We use TH = 166MeV. From this point on, we apply the hadronic cascade UrQMD [19, 20], about which more details are given later. All hadrons participate in the cascade, including those from the core (after freeze- out) and the corona. The corona particles, from string decay, are only ?visible? after a certain formation time (some constant of order one fm/c), multiplied by the corresponding gamma factor), so very high p_{T}particles have a good chance to escape.

The UrQMD model is a non-equilibrium transport approach. The interactions of hadrons in the current version include binary elastic and $2 \rightarrow$ n inelastic scatterings, resonance creations and decays, string excitations, particle + antiparticle annihilations as well as strangeness exchange reactions. The cross sections and branching ratios for the corresponding interactions are taken from experimental measurements (where available), detailed balance relations and the additive quark model. The model describes the full phase-space evolution of all hadrons, including resonances, in a heavy- ion collision based on their hadronic interactions and their decay products. Due to the short lifetime of resonances, their decay products may interact in the hadronic phase. This is not the case for weak decays, where the system has already decoupled at the time of the decay. As discussed previously, the experimental reconstruction of resonances will be influenced by the final state interactions of the decay products. Resonance signals have been previously studied using the UrQMD model.

3 Production of resonance with strangeness

The Quark Model, proposed independently by Murray Gell-Mann and Yuval Ne?eman in 1964 [21], enables the classification of hadrons in terms of their constituent quarks. In this model, the lighter mesons and baryons are representations of an $SU_f(3)$ group, whose fundamental representation is the three dimensional vector (u, d, s). These are the three lighter quarks whose characteristics are reported in Table reftable:quark.

Light flavor	d	u	s
Baryon number (B)	+1/3	+1/3	+1/3
Electric charge (Q)	-1/3	+2/3	-1/3
Isospin (I)	-1/2	+1/2	0
Strangeness (S)	0	0	-1
mass (MeV/c^2)	$2.3^{+0.7}_{-0.5}$	$4.8^{+0.5}_{-0.3}$	95±5

Table 6: Quantum numbers and masses associated to the three lighter quarks: u, d and s

The hadronic state are obtained from the decomposition of the following scalar products of the fundamental representations of the group:

Meson (q$\bar{q}$) $3 \bigotimes \bar{3} = 1 \bigoplus 8$

Baryon (qqq) $3 \bigotimes 3 \bigotimes 3 = 10_S \bigoplus 8_M \bigoplus 8_M \bigoplus 1_A$

For the baryons without c or b qaurk, flavor and spin may be combined in an approximate flavor-spin SU(6), in which the six basic states are d $\uparrow$, d $\downarrow$, $\cdots$, s $\downarrow$ ($\uparrow$, $\downarrow$ = spin up, down). Then the baryons belong to the multiplets on the right side of

$6 \bigotimes 6 \bigotimes 6 = 56_S \bigoplus 70_M \bigoplus 70_M \bigoplus 20_A$

Here, the 56 representation can be decompose in an octet ($J^P = 1/2^+$) and a decuplet ($J^P = 3/2^+$), as can be seen in Figure 6 and Figure 7.

Among the hadrons, the special family of particles that contain at least one strange quark but not heavier quarks (like charm or bottom), are called hyperons. These are: the Λ(uds), the triplet Σ^+(uus), Σ^0(uds), Σ^-(dds), the doublet Ξ^-(dss), Ξ^0(uss) and the Ω(sss) and the corresponding antiparticles. Ξ and Ω are the only hyperons containing more than one strange quark, hence they are called multi-strange baryons. Resonances shown in Figure reffig:decuplet having * with its name (e.g. $X^{*\pm}$) are particles with higher mass than the corresponding ground state particle with the same quark content. Different resonances with different lifetimes can probe different stages of the fireball expansion. The lifetime of some short-lived resonances is reported in Table 7. The ratios between resonances and

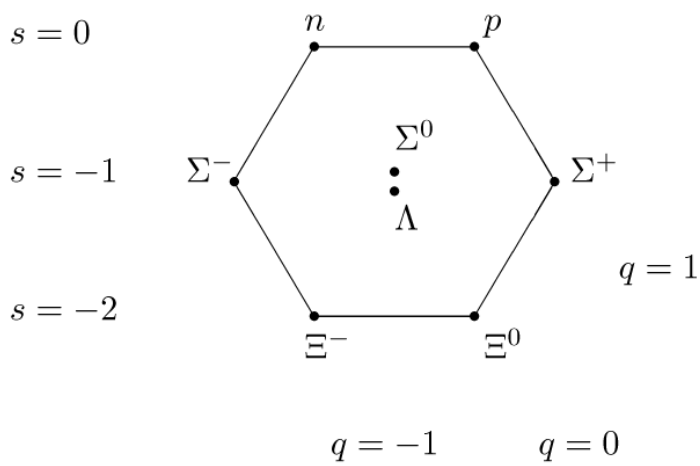

Figure 6: The $J^P = 1/2^+$ ground state baryon octet

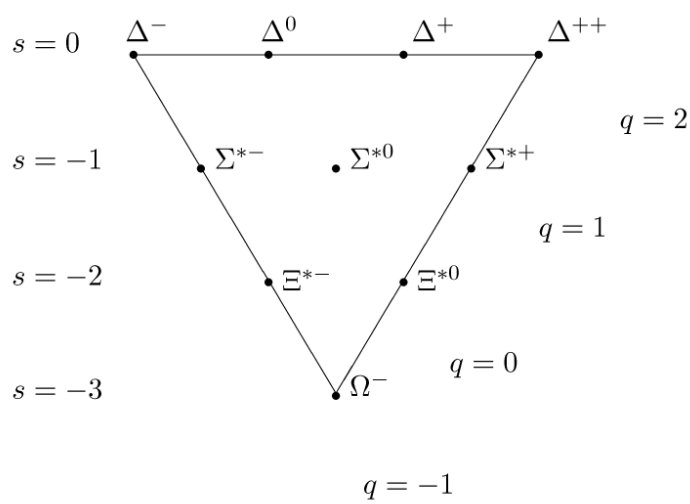

Figure 7: The $J^P = 3/2^+$ baryon decuplet

stable hadrons can be compared for resonances with different lifetimes and provide insights on the role of the re-scattering effect between the two freeze-out phases.

Particle	$\rho(770)$	$\Delta(1232)$	K*(892)	$\Sigma(1385)$	$\Lambda(1520)$	$\Xi(1530)$	$\Phi(1020)$
Lifetime[cτ]	1.3 fm	1.7 fm	4.0 fm	5.5 fm	10.3 fm	22 fm	46 fm

Table 7: Lifetime of hadronic resonances

In the following, a general overview of the role of the strange quark within the QGP studies with heavy-ion collisions is given. And importance of the measurement of resonance is explained as probe of properties in hadronic phase between the chemical(T_{ch}) and the kinetic freeze-out(T_{kin}).

3.1 Strange quark and hyperons

The original interest in the strangeness in the context of the QGP comes from an idea by Johann Rafelski and Berndt M*ü*ller. In 1982, they suggested a possible signature for the formation of a QGP in a heavy-ion collision [22]. The key argument, at a fixed collision energy, rests on the different production mechanism of the s quark within two different systems:

1. **Hadron Gas (HG)** , where the degrees of freedom are the hadronic ones, as quark and gluons are confined

2. **QGP** , where the degrees of freedom are partonic ones, with quarks and gluons free with respect to each other

The mass of the hadrons is only partly due to the mass of the constituent valence quarks.

Naively speaking, the quarks ?dress up? due to the strong interaction that keeps them confined. Once they are free, as in a QGP, the quarks recover their bare masses. It was predicted that, if the QGP is formed, an enhancement of the strange quarks should occur, because the production of $s\bar{s}$ pairs becomes easier due to the lower energy needed. When the QGP cools down, these strange quarks eventually recombine into hadrons favoring also an enhancement of the number of strange hadrons. This effect is larger for hadrons with higher strangeness, with the following scaling for the number type:

$N_\Omega > N_\Xi > N_\Lambda$

where N_Ω, N_Ξ, N_Λ are the number of produced Ω, Ξ and Λ. A certain enhancement of strange hadrons can occur also in a hadron gas system, but the processes of hadronisation in this case are relatively easy for K and Λ. and progressively harder for hadrons with higher strangeness, hence the relation would be:

$N_\Omega < N_\Xi < N_\Lambda$.

The production of multi-strange hadrons with respect to pp - like collisions is considered to be a signature of the formation of the QGP and it was observed at SPS, RHIC and LHC. [23]

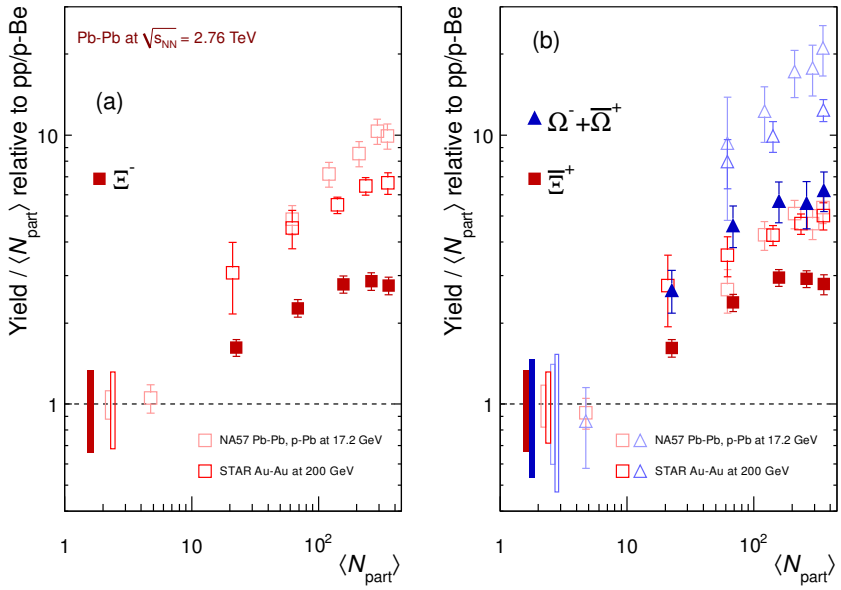

Figure 8: Enhancements in the rapidity range $|y|$ <0.5 as a function of the mean number of participants $\langle N_{part} \rangle$, showing LHC (ALICE, full symbols), RHIC and SPS (open symbols) data. Boxes on the dashed line at unity indicate statistical and systematic uncertainties on the pp or p-Be reference. Error bars on the data points represent the corresponding uncertainties for all the heavy-ion measurements and those for p–Pb at the SPS.

The measured enhancement factors of baryons with increasing strangeness content are reported in Figure 8 as a function of the number of participant nucleons, $\langle N_{part} \rangle$, in comparison with similar measurements at SPS and RHIC. For p–Pb collisions there is no evidence of enhancement. For Pb–Pb collisions the enhancement increases with centrality and the effect is larger for particles with higher strangeness content, up to a factor ?20 for ?s. No hadronic model has reproduced these observations and they can be interpreted as clear signal of QGP state formation. The comparison with results from the previous experiments shows that the relative enhancements decrease with increasing collision energy. An explanation of this behavior is given in terms of a statistical model, with canonical strangeness conservation. In a small system, with small particles multiplicities, quantum numbers conservation laws (such as strangeness) must be applied locally, event-by-event,

whereas in a large system, with many degrees of freedom, they can be applied in average, by means of the corresponding chemical potential. The conservation of quantum numbers is known to reduce the phase space available for particle production. This canonical suppression factor decreases with lower energy in the centre of mass of the collisions and could explain the larger enhancement for lower energy systems.

3.2 Resonance production

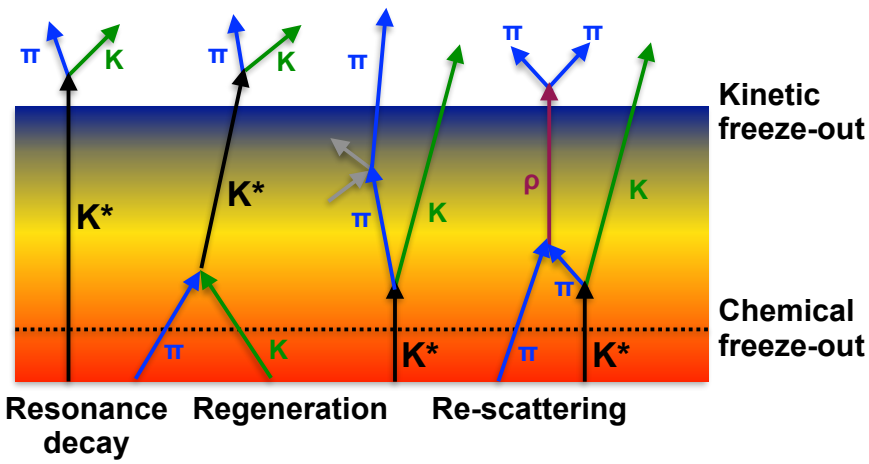

Figure 9: Hadronic phase

Resonances are particles with higher mass than the corresponding ground state particle with the same quark content. Hadronic resonances decay strongly, thus with a short lifetime, $\tau \sim$ few tenths of fm/c. The resonance natural width is given by $\Gamma = \bar{h}/\tau$, that is inversely proportional to the lifetime. Broad states with finite Γ decay very shortly after being produced and can be measured only by reconstruction of their decay products (or "daughters") in a detector. In heavy-ion collisions, hadronic resonances are produced within the bulk of the expanding medium, where they can decay while still traversing its volume. Decay products may interact with the other particles of the medium (mostly pions at the LHC), resulting in the impossibility of reconstructing the resonance, because the invariant mass of the daughters does not match that of the parent particle. Conversely, resonances may be regenerated as a consequence of pseudo-elastic collisions in the time lapse between the chemical (T_{ch}) and the kinetic freeze-out (T_{kin}). Re-scattering and regeneration depend on the individual cross section, hence lifetime, of the resonances and affect the measurement of their yield and momentum spectrum. The yield is decreased if the re-scattering dominates, vice versa the regeneration feeds the system with more particles.

The two effects may even compensate. Different resonances with different lifetimes can probe different stages of the fireball expansion. The ratios between resonances and stable hadrons can be compared for resonances with different lifetimes and provide insights on the role of the re-scattering effect between the two freeze-out phases.

4 A Large Ion Collider Experiment at the LHC

ALICE (A Large Ion Collider Experiment) has been collecting data during the whole first phase of the Large Hadron Collider operations, from its startup on the 23 November 2009 to the beginning of the first long technical shutdown in February 2013. During the first three years of operations LHC provided pp collisions at 0.9, 2.76, 7 and 8 TeV, Pb–Pb collisions at 2.76A TeV and finally p–Pb collisions at 5.02 TeV. The first section of this chapter focuses on the LHC performance during this phase and includes details on the accelerator parameters that allow the LHC to perform as a lead ion collider. A detailed description of the ALICE detector follows in the section 4.2.1. ALICE has been designed and optimized to study the high particle-multiplicity environment of ultra-relativistic heavy-ion collisions and its tracking and particle identification performance in Pb–Pb collisions are discussed. The attention is drawn in particular on the central barrel detectors. Section 4.2.2 describes the ALICE Data Acquisition (DAQ) system, that also embeds tools for the online Data Quality Monitoring (DQM). The final part of the chapter is dedicated to the offline computing and reconstruction system based on the GRID framework.

4.1 The Large Hadron Collider

The Large Hadron Collider (LHC) [24] at CERN is the biggest particle accelerator worldwide. The LHC project was approved in 1994 and construction works in the existing underground tunnel started in 2001 after the dismantling of the LEP collider, which had previously been built in the tunnel which is located under the Swiss-French border area close to Geneva at a depth of 50 to 175 m. The LHC has a circumference of 26.7 km. By design, its maximum achievable energies are 7 TeV for beam of protons and 2.76 TeV per nucleon for beam of lead ions, thus providing collisions at $\sqrt{s}$= 14 TeV and $\sqrt{s_{\mathrm{NN}}}$= 5.5 TeV, respectively. These would be the largest energies ever achieved in particle collision experiments. The LHC is a synchrotron that accelerates two counter-rotating beams in separate parallel beam pipes. In each of them bunches of particles travel many times around the accelerator ring before the collision energy is reached. The accelerator has to bend the beams around the ring, keep the bunches focused and accelerate them to their collision energy. Finally, the spatial dimension of the bunches has to be minimized in order to attain high luminosity, which ensure a high number of collisions per time interval at the collision points, i.e. a high luminosity. A combination of magnetic and electric field components performs the mentioned tasks. Despite the high luminosity reached, only a very small fraction of the particles of two bunches collides in a single bunch crossing. The others leave the interaction region essentially uninfluenced, are defocused, and continue to circulate in the accelerator.

Injection of bunches into the LHC (Figure 10) is preceded by acceleration in the LINAC2, PS booster, PS, and SPS accelerators. The acceleration sequence is slightly different for heavy-ions, in which case bunches pass the LINAC3, LEIR, PS, and SPS

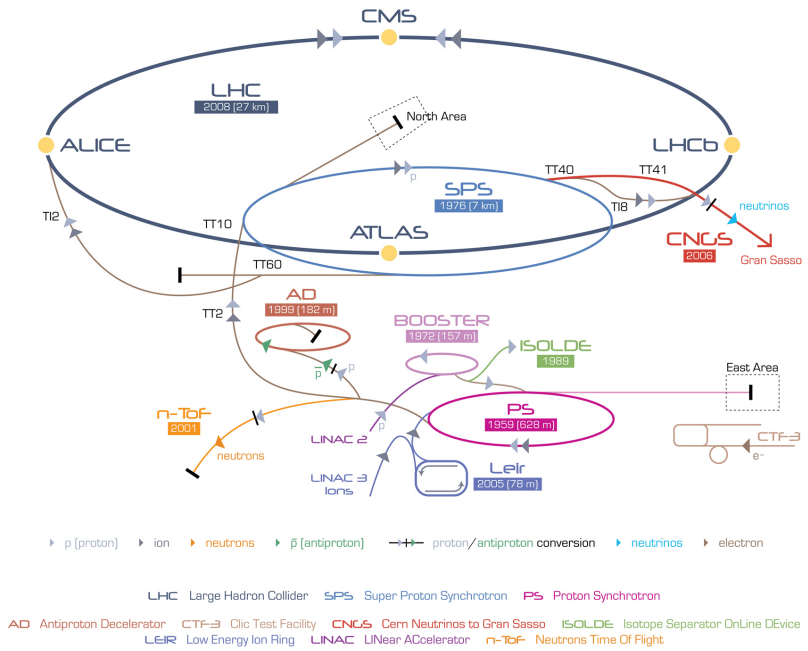

Figure 10: The CERN accelerator complex [2]

accelerators (more information can be found in [90]). Several injections to the LHC are needed until all bunches of both beams are filled. The first pp collisions at 900 GeV centre-of-mass energy were delivered by the LHC on September 10th 2008. Nine days later, the operations were interrupted due to a failure in an electrical connection between two magnets. The machine operators spent over a year repairing and consolidating the accelerator. On November 20th 2009 low energy proton beams circulated again, and a few days later, by achieving the energy of 1.18 TeV per proton beam, LHC became the most powerful accelerator in the world. The first pp collisions at centre-of-mass energy of 7 TeV were delivered in March 2010, and the first Pb?Pb collisions at centre-of-mass energy of 2.76 TeV per nucleon pair in November 2010. In 2010 the integrated luminosity delivered by the LHC was $\sim$ 48 pb^{-1} for pp collisions at $\sqrt{s}$= 7 TeV ($\sim$ 0.5 pb^{-1} in ALICE) and $\sim$ 10 μb^{-1} for Pb?Pb at $\sqrt{s_{\rm NN}}$= 2.76 TeV ($\sim$ 10 μb^{-1} in ALICE). In 2011 the beam energy was the same as in 2010 both for pp and Pb–Pb. The performance of the LHC improved in terms of luminosity with $\sim$ 5.61 fb^{-1} for pp ($\sim$ 2 pb^{-1} in ALICE) and $\sim$ 166 μb^{-1} for Pb–Pb collisions ($\sim$ 143.62 μb^{-1} in ALICE). In 2012, the centre-of-mass energy for pp collisions was brought to 8 TeV and the integrated luminosity (up to December 2012, end of the pp program) was $\sim$ 23.3 fb^{-1} ($\sim$ 10 pb^{-1} in ALICE). A pilot p–Pb run operated at $\sqrt{s_{\rm NN}}$= 5.02 TeV on September 2012, followed by a long p–Pb run on February 2013 with a delivered luminosity of 31.2 nb^{-1}. A very short pp run at $\sqrt{s}$= 2.76 TeV ended the Run1 of the LHC program, marking the start of the first long shutdown (LS1) until the end of 2014. Despite its excellent performance, the LHC has not yet achieved the nominal parameters ($\sqrt{s}$, L), that is the main goal for the next ignition of the machine in 2015. The LHC produces collisions in four so called Interaction Points (IPs) in correspondence of which are located six detectors of different dimensions and with different goals, all able to study the products of the interactions. These are:

ALICE (A Large Ion Collider Experiment-IP$_2$) [25] is a dedicated heavy-ion experiment designed to study strongly-interacting matter at very high energy density. It explores the phase transition to the QGP, its phase diagram, and its properties. Furthermore, ALICE will also study collisions of protons, on one hand as a baseline for heavy-ion measurements and on the other hand it contributes to measurements of identified particles by making use of its excellent particle identification capability and its acceptance at very low transverse momenta.

ATLAS (A Toroidal LHC ApparatuS-IP$_1$) and **CMS (Compact Muon Solenoid - IP$_5$)** [26][27] are general-purpose detectors for pp collisions that are built to cover the widest possible range of physics at the LHC. Specific topics are the search for the Higgs boson and physics beyond the Standard Model, e.g. new heavy particles postulated by supersymmetric extensions (SUSY) of the Standard Model and evidence of extra dimensions.

LHCb (The Large Hadron Collider beauty experiment-IP$_8$) [28] is a dedicated

experiment for the study of heavy flavor physics at the LHC. In particular, the experiment focuses on the study of CP violation and rare decays of beauty and charm particles, to test the Standard Model and to search for evidence of New Physics. The LHCb physics program is complementary to the flavor physics studies conducted at the B-factories and to the direct searches for new particles performed at ATLAS and CMS.

LHCf (Large Hadron Collider forward experiment-IP$_1$) [29] measures forward particles created during LHC collisions to provide further understanding of high energy cosmic rays. The detector is placed close to the ATLAS experiment.

TOTEM (TOTal Elastic and diffractive cross-section Measurement-IP$_5$) [30] measures the total cross-section, elastic scattering, and diffractive processes. The detector is located close to the CMS experiment.

4.2 The ALICE project

The ALICE experiment at the LHC [31] has as main goal the study of nuclear matter under extreme conditions of temperature and energy density such as those reached in ultra-relativistic heavy-ion collisions. The aim is to verify the QCD prediction of the existence of a phase transition from the common hadronic matter to the Quark-Gluon Plasma. Since ALICE is the only LHC experiment specifically designed for Pb–Pb collisions, it has to be able to cope with the large multiplicities associated with these collision systems and at the same time has to cover as many QGP-related observables as possible. ALICE is also interested in the study of pp interactions, as these are crucial for a comparison with Pb–Pb collisions, to tune Monte Carlo models and per se, like the other LHC experiments. With respect to these experiments, ALICE is endowed with an excellent Particle IDentification (PID) performance, obtained combining different PID techniques from different detectors that are optimized in different momentum (p) regions.

4.2.1 ALICE detector

ALICE is a complex of 14 detector subsystems (Figure 11) that can be classified in three groups:

Central detectors are housed in a solenoid magnet which provides the experiment with a 0.5 T magnetic field and covers the pseudo-rapidity interval -0.9 $< \eta <$0.9 (corresponding to a polar acceptance $\pi/4 < \theta < 3\pi/4$). The azimuthal acceptance is 2π. They are mainly dedicated to vertex reconstruction, tracking, particle identification and momentum measurement. Starting from the interaction region and going outward, we find the following detectors:

- Inner Tracking System (ITS)
- Time Projection Chamber (TPC)
- Transition Radiation Detector (TRD)
- Time Of Flight (TOF)

In the mid-rapidity region there are also three detectors with limited azimuthal acceptance:

- High Momentum Particle Identification Detector (HMPID)
- PHOton Spectrometer (POHS)
- ElectroMagnetic CALorimeter (EMCAL)

Muon spectrometer is placed in the forward pseudo-rapidity region (-4.0 $< \eta <$ -2.5) and consists of a dipole magnet and tracking and trigger chambers. It is optimized to reconstruct heavy quark resonances (such as J/Ψ through their $\mu^+\mu^-$ decay channel) and single muons.

Forward detectors are placed in the high pseudo-rapidity region (small angles with respect to the beam pipe). They are small and specialized detector systems used for triggering or to measure global event characteristics. They are:

- Time Zero (T0) to measure the event time with precision of the order of tens of picoseconds, as needed by TOF
- VZERO (V0) to reject the beam-gas background and to trigger minimum bias events
- Forward Multiplicity Detector (FMD) to provide multiplicity information over a large fraction of the solid angle (-3.4 $< \eta <$ -1.7 and 1.7 $< \eta <$ 5)
- Photon Multiplicity Detector (PMD) to measure the multiplicity and the spatial distribution of photons on an event-by-event basis in the 2.3 $< \eta <$ 3.7 region
- Zero Degree Calorimeter (ZDC) to measure and trigger on the impact parameter. The ZDC consists of two calorimeters, one for neutrons (ZDC:ZN) and one for protons (ZDC:ZP), and includes also an electromagnetic calorimeter (ZEM)

The ALICE global coordinate system [32] is a right-handed orthogonal Cartesian system with the origin X, Y, Z = 0 at the centre of the detector. The three Cartesian axes are defined as follows: the X axis pointing towards the centre of the LHC, the Y axis pointing upward and the Z axis parallel to the local mean beam line pointing in the direction opposite

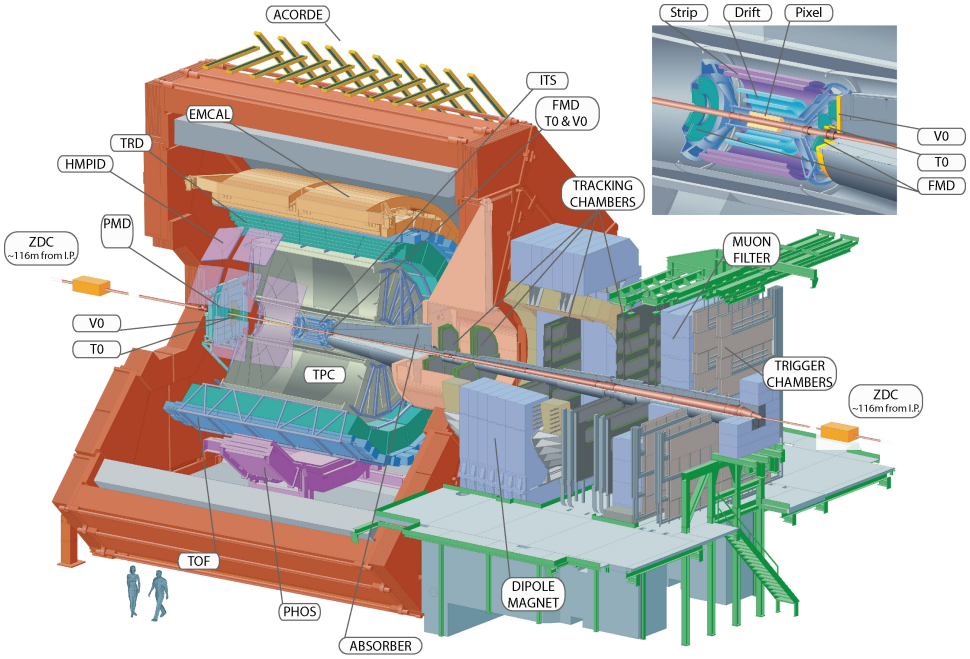

Figure 11: The ALICE detector

to the muon spectrometer. The azi- muthal angle increases counter-clockwise from the positive X axis (Φ= 0) to the positive Y axis ($\Phi = \pi/2$) with the observer standing at positive Z and looking at negative Z; the polar angle increases from the positive Z axis (θ = 0) to the X-Y plane ($\theta = \pi/2$) and to the negative Z axis ($\theta = \pi$).

In the following Sections more specific descriptions of the detectors used in the identification of the $\Xi(1530)^0$ baryons and in the determination of the characteristics of typical collisions will be given.

ITS

The ITS [31] (Figure 12) is the barrel detector closest to the beam pipe. Its main goals are:

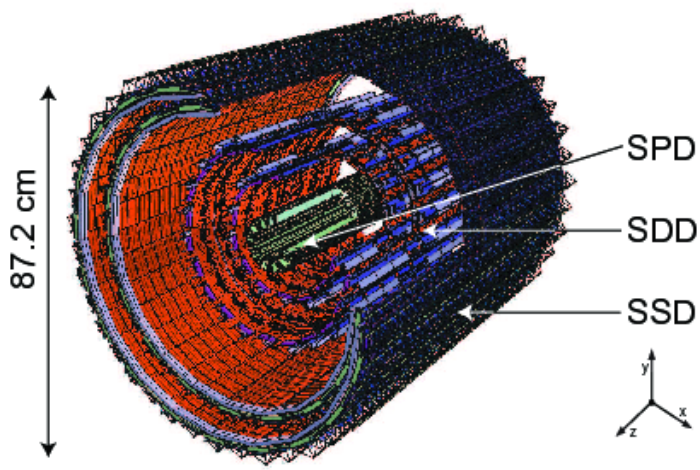

Figure 12: Schematic view of the ITS [3]

- to contribute with the TPC to the global tracking of ALICE by improving the angle and momentum resolution
- to reconstruct the position of the primary interaction vertex
- to reconstruct secondary vertices from decays of heavy-flavor and strange particle decays;
- to track and identify particles with momentum below 100 MeV/c^2
- to improve the momentum, impact parameter and angle resolution for the measurement of high p_{T}particles performed with the TPC

- to reconstruct particles traversing dead regions of the TPC

The ITS surrounds the beam pipe (which is a 800 μm thick cylinder with an outer diameter of 2.9 cm) and consists of six cylindrical layers of silicon detectors located at radii between 4 cm and 43 cm. Due to the high track density, the two innermost layers are Silicon Pixel Detectors (SPD) which guarantee a high granularity. They are followed by two layers of Silicon Drift Detectors (SDD), while the two outmost layers are double-sided Silicon micro-Strip Detectors (SSD).

Since the momentum and impact parameter resolutions for low momentum particles are dominated by multiple scattering effects, the amount of material in the active volume has been minimized as much as possible. The granularity of the detector was optimized to keep the occupancy low in all the layers. With the technology chosen, the ITS detectors reach a spatial resolution of the order of a few tens of ?m4 resulting in a resolution on the impact-parameter5 better than 70 ?m in the r plane for pT ¿ 1 GeV/c and thus well suited for the reconstruction of heavy-flavor decays (see Figure 13).

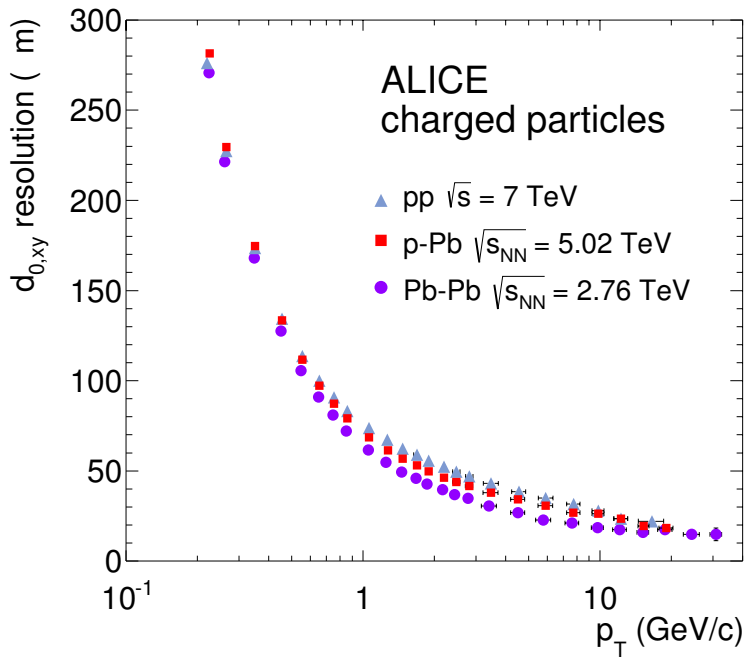

Figure 13: Track impact parameter resolution in the transverse plane (rϕ) vs $p_{\mathrm{T}}$for charged particle

TPC

The TPC [33] (Figure 14) is the main tracking detector of the central barrel, optimized

to provide, together with the other central barrel detectors, charged- particle momentum measurements with good two-track separation, particle identification and vertex determination. The TPC was designed for an excellent tracking performance in the high multiplicity environment of Pb–Pb collisions. For this reason, it was chosen to be a drift chamber, cylindrical in shape, 5 m long, with the inner radius ($r_{in} \sim 85$ cm) determined by the maximum acceptable track density, and the external one ($r_{ext} \sim 250$ cm) by the minimum track length for which dE/dx resolution is $< 10\%$. The TPC volume is filled with 90 m^3 of $Ne/CO_2/N_2$ (90/10/5). The readout planes are divided in 18 sectors in which multi-wire proportional chambers (with cathode pad readout) are housed. Because of its good dE/dx resolution, the TPC can identify particles with $p_T < 1$ GeV/c on a track-by-track basis.

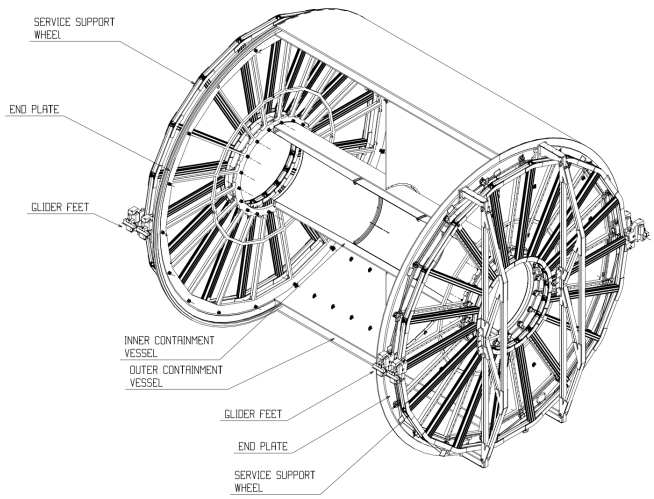

Figure 14: Schematic view of the TPC

Charged particles traveling through the TPC ionize the detector?s gas; the measurement of this loss of energy is what we need to identify a particle. The physics observable in this case is the energy loss per unit length, within the matter crossed by the charged particle, which we call specific energy loss, also denoted by dE/dx. This is described by the Beth–Bloch equation, 5, that highlights the key of the identification technique: this observable depends only on the charge and on velocity (β) of the particle, which, in turn, depends only on the momentum and the mass of the ionizing particle. Since momentum is already known due to track curvature and charge is unitary for most measured tracks, measuring the dE/dx allows us to indirectly determine mass and thus determine the particle species. The Bethe-Bloch equation gives the mean specific energy loss:

$$-\langle\frac{dE}{dx}\rangle = k_1 \cdot z^2 \frac{Z}{A} \cdot \frac{1}{\beta^2}[\frac{1}{2} ln(k_2 \cdot m_e c^2 \cdot \beta^2\gamma^2) - \beta^2 + k_3] \quad (5)$$

where $\beta\gamma = p/\mathrm{Mc}$ and: Z: atomic number of the ionized gas (in this case $Ne/CO_2/N_2$)
A: mass number of the ionized gas (g/mol)
m_e: electron mass
z: electric charge of the ionizing particle in unit of electron charge e
M: ionizing particle mass
p: ionizing particle momentum
β: ionizing particle velocity normalized to the light velocity c
$\gamma = 1/\sqrt{1-\beta^2}$, Lorent factor
k_1, k_2, k_3: constants depending on the ionized medium

For a given ionizing particle mass hypothesis, a given momentum and a given length of the trajectory in the ionizing medium, the total charge deposited along the trajectory is subject to statistical fluctuations. This random variable follows a Landau distribution, that give us the opportunity to measure the mean value hdE/dxi. The long tail of the Landau distribution is usually truncated at 50%-70% of the collected signal.

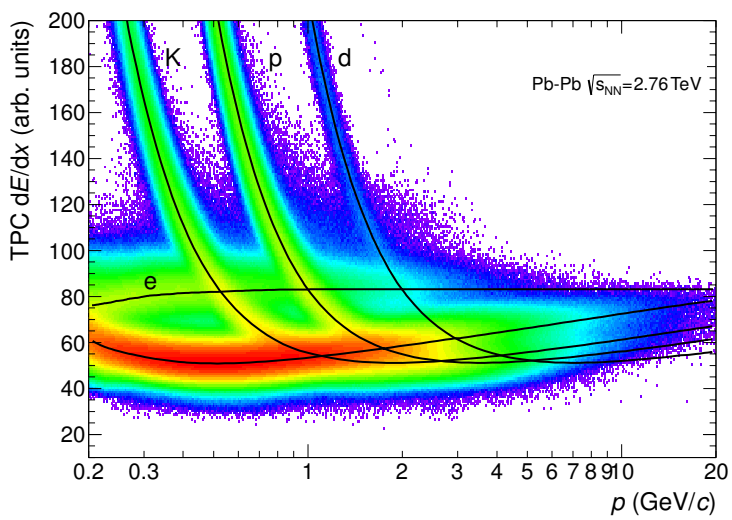

Figure 15: Specific energy loss (dE/dx) in the TPC vs. particle momentum in Pb–Pb collisions at $\sqrt{s_{\mathrm{NN}}}$= 2.76 TeV. The lines show the parametrisations of the expected mean energy loss.

The specific energy loss in the TPC as a function of momentum is shown in Figure 15. The different bands characteristic for $e^{\pm}$, $\pi^{\pm}$, $K^{\pm}$, $p^{\pm}$ are clearly visible. These are the evidence of the statistical distribution of the measured energy loss around the expected mean value. The expected value correspond to the prediction by a Bethe–Bloch experimental parametrization (superimposed as black lines in the Figure). For a track

within the TPC the relevant quantity to be considered for PID is the difference between the measured specific energy loss and the corresponding predicted value, by the Bethe-Bloch parametrization for a given measured momentum. If normalized to the resolution of the dE/dx measurement in the TPC, this difference could be expressed in number of σ(see Equation 6). In this way it is possible to estimate more quantitatively the goodness of a mass hypothesis. This also gives us the possibility to choose the strictness we want to adopt in the identification of a particle (n_σ , n = 2, 3, 4):

$$n_\sigma = \frac{(dE/dx)_{measured} - (dE/dx)_{Bethe-Bloch}}{\sigma_{TPC}} \tag{6}$$

V0

The VZERO detector [34] consists of two segmented arrays of plastic scintillator counters, called VZERO-A and VZERO-C, placed around the beam-pipe on either side of the IP: one at Z = 340 cm, covering the pseudo-rapidity range [2.8; 5.1], and the other at Z = -90 cm (in front of the absorber), covering the pseudo-rapidity range [-3.7; -1.7]. They consist of 32 counters distributed in four rings, each divided in eight 45 sectors. Each counter is made of scintillator material embedded with WaveLength Shifting fibers. Clear fibers collect and transport the signal to photomultipliers 3 - 5 m far from the detector, inside the L3 magnet. The counters have a time resolution better than 1 ns. Their response is recorded in a time window of 25 ns around the nominal beam crossing time. The VZERO has an important role in rejecting background from beam-gas collisions (see, Figure 16) exploiting the relative time-of-flight measurement between the two arrays: when the beam-gas collision takes place outside the region between the two arrays, particles arrive 6 ns before or after the time of a beam-beam collision.

The VZERO is a trigger detector that will provide a minimum-bias trigger for all colliding systems to the central barrel detectors and three centrality triggers in p–Pb and Pb–Pb collisions (multiplicity, central and semi-central).

The first parameter to be determined in A–A(p–A) collisions is the centrality(multipliciy). This is defined according to the value of the impact parameter, b, and provides a geometrical scale of the overlapping region between the colliding nuclei: a collision will be defined from central to peripheral, as the impact parameter increases. The centrality of a collision is not directly available and must be deduced from a combination of experimentally measured quantities and Monte Carlo simulations. There are a number of observables that can be measured and used as centrality estimators. The charged-particle multiplicity N_{ch} and the transverse energy E_T measured around mid-rapidity are measurable quantities related to the energy deposited in the interaction region (these are therefore related to N_{part}). These variables increase significantly increasing the centrality of the collisions. Another measurable quantity to estimate the centrality is the zero-degree energy EZDC, namely the energy carried by spectator nucleons N_{spec} = 2A - N_{part} = E_{ZDC}/E_A, where E_A is the beam energy per nucleon. Typically a measured distribution of one of the previous observables is mapped to the corresponding distribution obtained from phenomenological

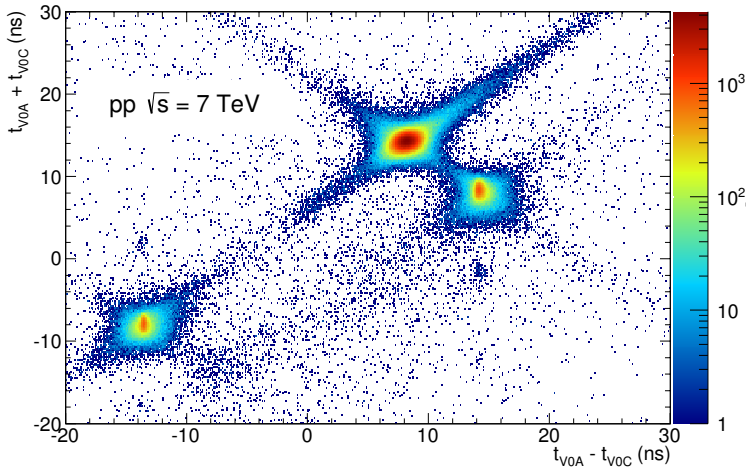

Figure 16: Correlation between the sum and difference of signal times in V0A and V0C. Three classes of events collisions at (8.3 ns, 14.3 ns), background from Beam 1 at (-14.3 ns, -8.3 ns), and background from Beam 2 at (14.3 ns, 8.3 ns) can be clearly distinguished.

Glauber calculations. The Glauber model [35, 36] uses a semi-classical approach: the A?A collision is assumed to be an incoherent superposition of N elementary nucleon- nucleon collisions. The main parameters of the model are the inelastic nucleon- nucleon collision cross-section σ_n and the nuclear density distribution ρ(r). In practice, the simulated distribution well reproduce the measured distribution or the latter is fitted with an analytical function. The experimental distribution can then be divided in classes with sharp cuts on the measured observable (E_{ZDC}, E_T or N_{ch}). These "centrality" classes will correspond to well defined percentage of the integral of the distribution. A given centrality class in the measured distribution, corresponds to the same class in the simulated distribution, where the main geometrical variables (N_{part}, N_{coll} and T_{AA}) can be determined. The number of classes that can be defined depends on the resolution achievable on the selection variable. In the analysis described in this thesis the centrality(multiplicity) estimation is based on the measurement of the multiplicities from the VZERO scintillators [37][38]. This is the method that achieve the best centrality resolution: it ranges from 0.5% in central to 2% in peripheral collisions. Other methods, as the ones based on the E_{ZDC} measurement or based on the estimate of the number of tracks in the SPD or TPC, are used to asses a systematic uncertainty on the centrality determination. The distribution of the VZERO amplitudes is shown in Figure 17 where the centrality(multiplicity) percentiles are also indicated.

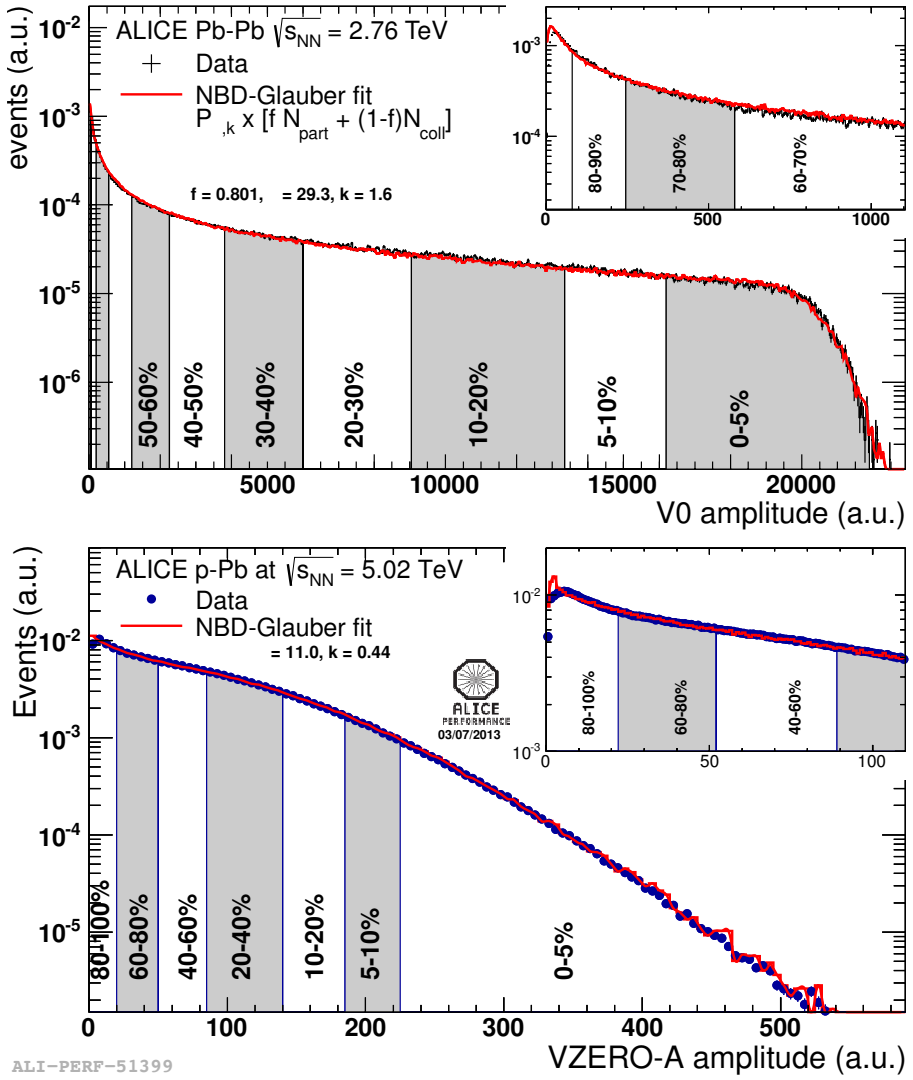

Figure 17: Distribution of the V0 amplitude (sum of V0A and V0C in top, V0A in bottom). The inset shows a magnified version of the most peripheral region.

4.2.2 Data Acquisition (DAQ) and trigger system

The architecture of data acquisition is shown in Figure 18. The tasks of the ALICE DAQ system are the assembly of event informations from individual detectors into complete events (event building) as well as buffer- ing and export of assembled events to permanent storage. The DAQ is designed to process a data rate up to 1.25 GB/s in heavy-ion runs. Event building is done in two steps. Data from the detectors is received by Detector Data Links (DDLs) on Local Data Concentrators (LDCs). The LDCs assemble the data into sub-events that are then shipped to Global Data Collectors (GDCs). A GDC re- ceives all sub-events from a given event and assembles them into a complete event. These events are subsequently stored on a system called Transient Data Storage (TDS).

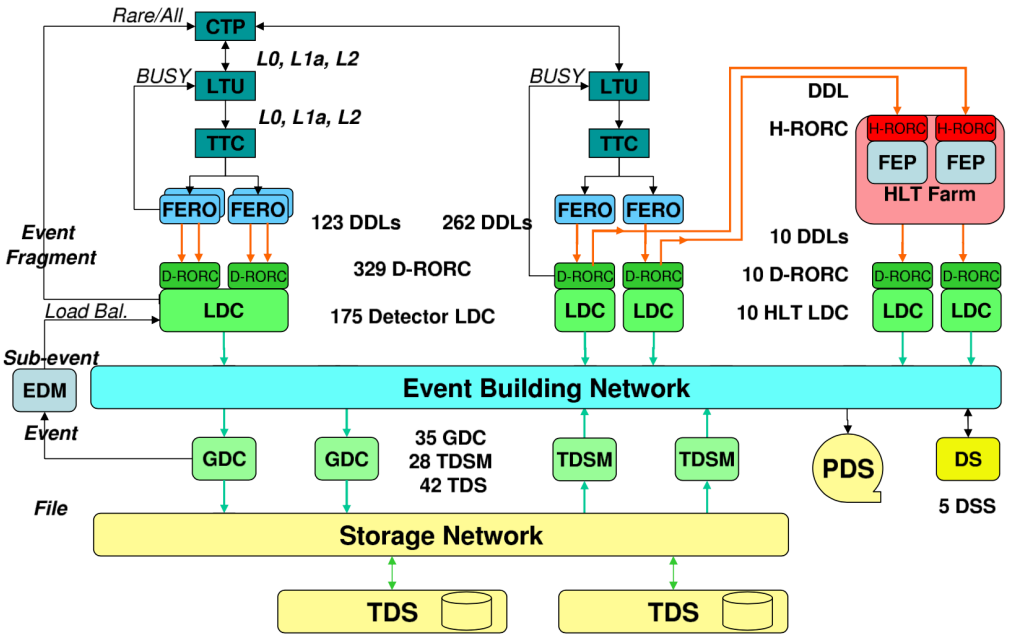

Figure 18: The overall architecture of the ALICE DAQ and the interface to the HLT system.

ALICE can simultaneously take data in several partitions, where a set of detec- tors can store their outputs. Since a partition is a group of commonly controlled detectors, a given detector can only be active in one partition at a time. The ac- tive detectors in a given partition may be assigned to data taking groups called clusters, for which triggers

can be defined. Therefore, upon a trigger only a sub- set of the whole partition may be read out. Furthermore, a triggering detector does not have to be necessarily part of the partition. ALICE has a two-layer trigger architecture [39]. The low-level trigger is a hardware trigger called Central Trigger Processor (CTP). The High-Level Trigger (HLT) is implemented as a pure software trigger. The CTP combines inputs from different trigger sources, namely the various detectors. These inputs are single signals, like a hit in the detector, or, can be the result of fast calculation performed directly in the detectors. The HLT allows the implementation of sophisticated logic for the triggering. In contrast to the CTP which governs the readout of the detectors, the HLT receives a copy of the data read out from the detectors and processes them. The hardware trigger combines the trigger signals of the various detectors to decide if an event is accepted, that means it is read out and written to disk. Several trigger levels reduce the event rate depending on the input signals. The first level, called L0, is delivered after 1.2 ?s, while the second, called L1, after 6.5 ?s. The final trigger, L2, is delivered after 100 ?s, upon completion of the drift time in the TPC. Only after an L2 trigger the event is finally stored. The rates of different trigger classes are very different. By definition minimum-bias triggers have the highest rate; other triggers that look for rare signals are characterized by much lower rates. In order to cope with different scenarios, downscaling factors can be applied to the trigger classes individually, i.e. only every nth event fulfilling the trigger condition is read out. The total recording rate is limited by the maximum bandwidth of data that can be recorded to disk and tape. The ALICE software trigger, called HLT, is a farm of multiprocessor computers. The aim is to have about 1000 PCs processing the data in parallel allowing an online analysis of the events. A trigger decision comes from the analysis of a more comprehensive set of information than what happens for the hardware trigger, giving the possibility to apply more sophisticated triggers. Examples include triggers on high energy jets or on muon pairs. Furthermore, the HLT can significantly reduce the event size by selecting regions of interest (partial readout of detectors) and by further compression of the data. The HLT receives a copy of the raw data and performs per detector reconstruction, partly aided by hardware coprocessors. Subsequently, the trigger decision is based on the global reconstructed event. In the same step a region of interest can be selected. In the last optional step, if the trigger decision is positive, the data are compressed. The trigger decision, partial readout information, compressed data, and the re- construction output is sent to LDCs and subsequently processed by the DAQ. In terms of the overall DAQ architecture, data sent by HLT is treated like stemming from a detector.

4.2.3 ALICE offline software frame work

The required computing resources for the reconstruction and analysis of the raw data as well as the production of simulated events needed for the understanding of the data exceed the computing power of single institutes and even centers like CERN. Therefore, institutes that are part of the Collaboration also provide storage and computing resources. Distribution of the data for reconstruction and analysis cannot be performed manually and this led to the need for an automated system. The concept of a decentralized computing model called Grid [40] was identified as a solution.

The AliEn Framework

The Grid paradigm implies the unification of resources of distributed computing center, in particular computing power and storage, to provide them to users all over the World. It allows computing center to offer their resources to a wider community and the local resources to be shared by an entire collaboration. Software that implements the Grid concept is called Grid middleware. ALICE has developed a Grid middleware called AliEn [41] since 2001. An ALICE user employs AliEn to connect to the ALICE Grid which is composed of a combination of general services that are provided by many Grid middleware solutions and ALICE-specific services provided by AliEn. Parts of the ALICE Grid are: i) a global file catalog that is a directory of files in storage elements distributed over the Globe, ii) the automatic matching of jobs for execution to a suitable location in one of the connected sites, iii) a shell-like user interface and iv) API9 services for the ROOT framework [42].

AliRoot Framework

AliRoot [31] is the offline framework for simulation, alignment, calibration, reconstruction, visualization, quality assurance, and analysis of experimental and simulated data. It is based on the ROOT framework. Most of the code is written in C++ with some parts in Fortran that are wrapped inside C++ code. Re-usability and modularity are the basic features of the AliRoot framework. Modularity allows parts of the code to be replaced, with minimum or no impact on the rest (for example changing the event generator, the transport Monte Carlo or the reconstruction algorithms). This is achieved implementing abstract interfaces. In addition codes for each detector subsystem are independent modules with their specific code for simulation and reconstruction and the code can be developed concurrently with minimum interference. Re-usability is meant to maintain a maximum amount of backward compatibility as the system evolves.

The central module of the AliRoot framework is STEER (Figure 19) which provides several common functions such as: steering of program execution for simulation, reconstruction and analysis; general run management, creation and destruction of data structures, initialization and termination of program phases; base classes for simulation, event generation, reconstruction, detectors elements. For event simulation the framework provides the following functionality:

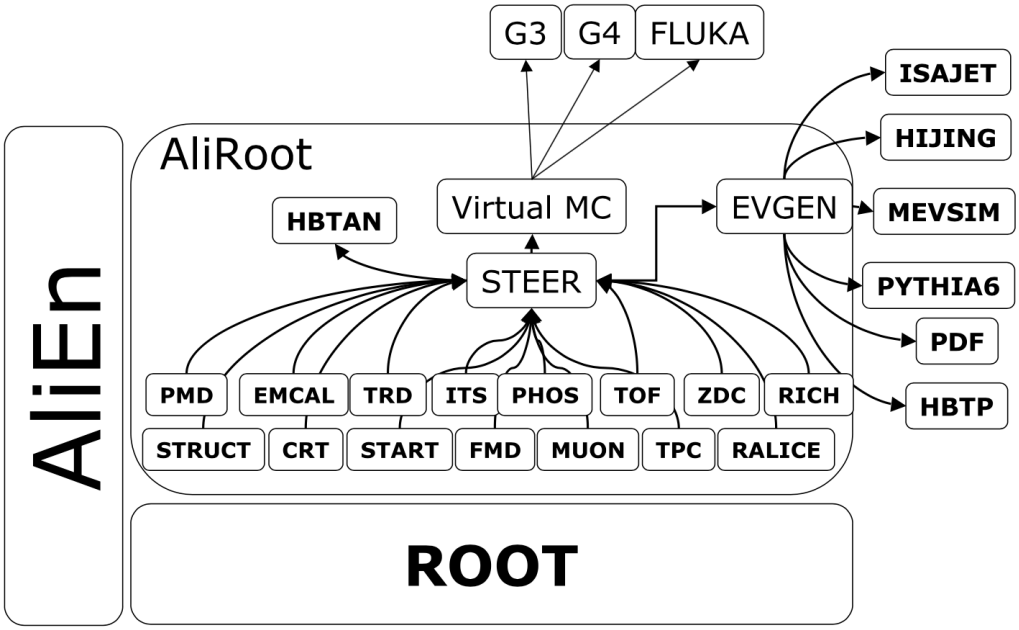

Figure 19: Schematic view of the AliRoot framework

5 Measurement of $\Xi(1530)^0$ production in p–Pb and Pb-Pb

The measurement of resonance production in p–Pb collisions helps to disentangle cold nuclear matter effects from genuine hot medium effects and contribute to the study of the system size dependence of re-scattering in the hadronic phase. And the measurement in ultra-relativistic heavy-ion collisions such as Pb–Pb collisions, provide information on the properties of hadronic medium and different stage of its evolution. In order to study the particle production mechanism in the hadronic phase between the chemical and kinetic freeze-out, the $\Xi(1530)^0$ resonance production at mid-rapidity($-0.5 < y_{\mathrm{CMS}} < 0$) is measured in p–Pb collisions $\sqrt{s_{\mathrm{NN}}}$= 5.02 TeV and in Pb–Pb collisions with $|y|$ <0.5 at $\sqrt{s_{\mathrm{NN}}}$2.76 TeVwith the ALICE experiment, via the reconstruction of its hadronic decay into $\Xi\pi$.

5.1 $\Xi(1530)^0$ -reconstruction

The Ξ^{*0} production in p–Pb and Pb–Pb collisions at mid-rapidity has been studied in different multiplicity classes, from very central to peripheral collisions. The analysis strategy is based on the invariant mass study of the reconstructed pairs (referred to as the candidates) whose provenance could be the decay of a Ξ^{*0} baryon into charged particles. The decay products (also called daughters in the text) are identified as oppositely charged Ξ and π among the tracks reconstructed in the central barrel. The event selection, track selection and the particle identification strategy is described. The raw signal yield is extracted by fitting the background-subtracted invariant mass distribution in several transverse momentum intervals. In order to extract the p_{T}-dependent cross section, these yields are corrected for efficiency. The p_{T}-dependent correction due to the detector acceptance and reconstruction efficiency, (Acc $\times$ ϵ_{rec})(pt), is computed from a Monte Carlo simulation. The absolute normalisation is then performed, by dividing for the number of the events in each multiplicity and centrality classes.

5.1.1 Data sample and event selection

A description of the ALICE detector and of its performance during the LHC Run 1 (2010–2013) can be found in [31, 43]. The data sample in the analysis from Pb–Pb collisions with energy of $\sqrt{s_{\mathrm{NN}}}$=2.76 obtained during 2011 and the sample of p–Pb run at $\sqrt{s_{\mathrm{NN}}}$= 5.02 TeV was recorded in 2013.

Due to the asymmetric energies of the proton (4 TeV) and lead ion (1.57 A TeV) beams, the centre-of-mass system in the nucleon-nucleon frame is shifted in rapidity by Δy_{NN} = 0.465 towards the direction of the proton beam with respect to the laboratory frame of the ALICE detector [5]. For the analysed p–Pb data set, the direction of the proton beam was towards the ALICE muon spectrometer, the so-called "C" side, standing for negative rapidities; conversely, the Pb beam circulated towards positive rapidities, labelled as "A"

side in the following. The analysis in this paper was carried out at midrapidity, in the rapidity window $-0.5 < y_{\mathrm{CMS}} < 0$.

The minimum-bias trigger during the p–Pb run was configured to select events by requiring a logical OR of signals in V0A and V0C [43], two arrays of 32 scintillator detectors covering the full azimuthal angle in the pseudo-rapidity regions $2.8 < \eta_{\mathrm{lab}} < 5.1$ and $-3.7 < \eta_{\mathrm{lab}} < -1.7$, respectively [44]. In the data analysis it was required to have a coincidence of signals in both V0A and V0C in order to reduce the contamination from single-diffractive and electromagnetic interactions. Out of this sample in p–Pb collision events about 109.3 million events, 93.9 million events satisfy the following selection criteria and have been actually used for the analysis.

The Pb–Pb collisions data sample was selected by online centrality trigger requiring a signal in the forward V0 detectors[38] to record enhanced data in central collision. The data consists of 24.8 million events in most central collisions (0-10%), 21.8 million events in semi-central collisions (10-50%) and 3.5 million events with minimum-bas trigger (0-90%). Among 49.6 million events in total, 43.0 million events have been analyzed as passed the criteria below.

- Events with z-coordinate of primary vertex (Vz) falling within ± 10 cm from the interaction point
- Rejection of pile-up event
- Requiring primary tracks to have at least one hit in one of the two innermost layers of the ITS (silicon pixel detector, SPD)
- p–Pb: multiplicity ranges in percentile (V0A): 0-20%, 20-40%, 40-60%, 60-100% and MB(0-100%)
- Pb–Pb: centrallity classes (V0A and V0C): 0-10%, 10-40%, 40-80% and MB (0-80%)

The distribution of the vertex z position of the accepted events in p–Pb collision is reported on left panel in Figure 20 and corresponding figure but obtained from Pb–Pb collisions is shown on right panel in Figure. 20. Events with $|\mathrm{V}_z|$ <10 cm have been used to ensure a uniform acceptance in the central pseudo-rapidity region, $|\eta|$ <0.8, where the analysis is performed. This cut reduces the total number of events to 97.5 million events, that is the ∼89.2% of the initial sample in p–Pb collisions and 43.04 million events which is ∼86.8% of the initial sample in Pb–Pb collisions are survived.

Fig. 21 shows the multiplicity distribution of the accepted events in p–Pb collision divided in bins of percentile. The each color on the histogram indicate the multiplicity ranges used in this analysis. Corresponding events for each multiplicity range are in Table 8.

The distribution of centrality in each trigger used to select the events in Pb–Pb collision is shown in Fig. 22 and the reason why the centrality has step structure is that there are

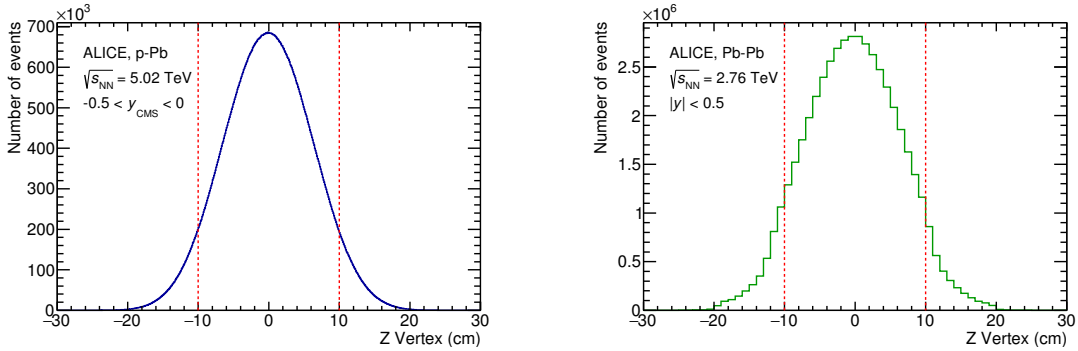

Figure 20: Vertex-z coordinate distribution of the accepted events in p–Pb collision(Left) and in Pb–Pb collisions(Right). The red dashed line indicates vertex cut

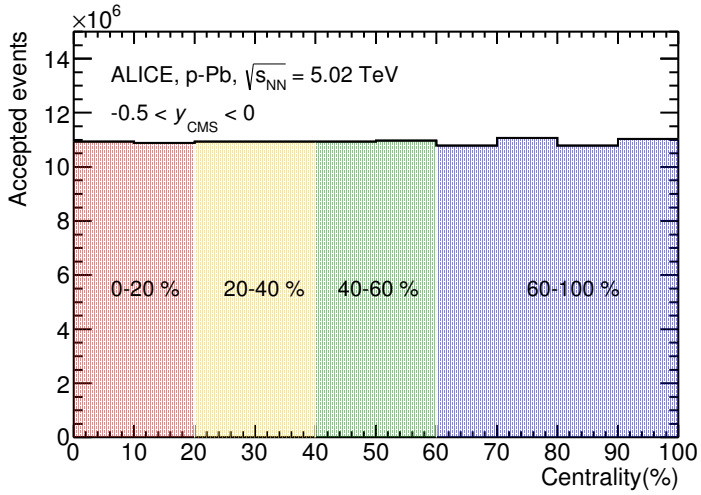

Figure 21: Multiplicity distribution of accepted events in p–Pb collision in percentile. The each color and labels define the four intervals in which the analysis in performed.

three different trigger classes classified by the amplitude threshold on VZERO detector. Because the distribution of events as function of centrality is not a flat, this may lead to additional bias, in particular when one needs to combine the results from different triggers. For example, events from 40-80% centrality bin have bias with high statistics in 40-60%. In order to avoid this effect, we have applied a flattening procedure to have flat distribution of events as function of centrality. A brief explanation of the method is below :

1. Histograms are obtained for the effective mass distribution in 1% centrality bins and for the centrality distribution
2. The effective mass distributions are scaled in each 1% centrality bin by a factor: Factor = $N_{\text{event in 20-40\%}}$ / 20 / $N_{\text{event in current 1\% bin}}$
3. Each bin in the centrality distribution is scaled using the factor described above
4. Histograms are added for centrality bins of interest: 0-10%, 10-40%, 40-80%, 0-80%

The resulting number of events in each centrality classes is summarized in Table 8.

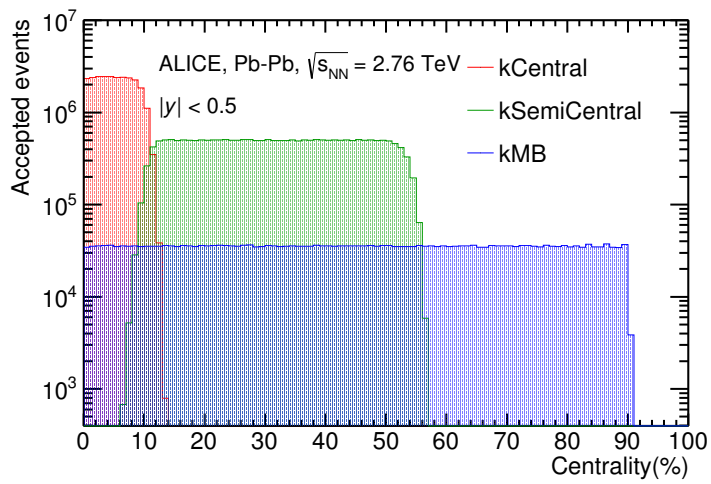

Figure 22: Centrality distribution of three different trigger classes.

p–Pb	0-20%	21.82×10^{6}
	20-40%	21.86×10^{6}
	40-60%	21.91×10^{6}
	60-100%	43.68×10^{6}
Pb–Pb	0-10%	5.58×10^{6}
	10-40%	16.73×10^{6}
	40-80%	22.31×10^{6}

Table 8: Number of accepted and analyzed events per multiplicity/centrality interval

5.1.2 Track and topological selection

In comparison with the Ξ^{*0} analysis carried out in pp collisions at $\sqrt{s} = 7$ TeV [7], track and topological selections were revised and adapted to the p–Pb dataset. Pions from strong decays of Ξ^{*0} were selected according to the criteria for primary tracks. As summarized in Table 9, all charged tracks were selected with $p_{\mathrm{T}} > 0.15$ GeV/c and $|\eta_{\mathrm{lab}}| < 0.8$, as described in Ref. [43]. The primary tracks were chosen with the Distance of Closest Approach (DCA) to PV of less than 2 cm along the longitudinal direction (DCA_z) and lower than $7\sigma_r$ in the transverse plane (DCA_r), where σ_r is the resolution of DCA_r. The σ_r is strongly p_{T}-dependent and lower than 100 μm for $p_{\mathrm{T}} > 0.5$ GeV/c [43]. To ensure a good track reconstruction quality, candidate tracks were required to have at least one hit in one of the two innermost layers (SPD) of the ITS and to have at least 70 reconstructed points in the Time Projection Chamber (TPC), out of a maximum of 159. The Particle IDentification (PID) criteria for all decay daughters are based on the requirement that the specific energy loss ($\mathrm{d}E/\mathrm{d}x$) is measured in the TPC within three standard deviations (σ_{TPC}) from the expected value ($\mathrm{d}E/\mathrm{d}x_{\mathrm{exp}}$), computed using a Bethe-Bloch parametrization [43].

Common track selections	$\lvert\eta_{\mathrm{lab}}\rvert$	< 0.8
	p_{T}	> 0.15 GeV/c
	PID $\lvert(\mathrm{d}E/\mathrm{d}x)-(\mathrm{d}E/\mathrm{d}x)_{\mathrm{exp}}\rvert$	$< 3\ \sigma_{\mathrm{TPC}}$
Primary track selections	DCA_z to PV	< 2 cm
	DCA_r to PV	$< 7\sigma_r$-$10\sigma_r$ (p_{T})
	number of SPD points	≥ 1
	number of TPC points	> 70
	χ^2 per cluster	< 4

Table 9: Track selections common to all decay daughters and primary track selections applied to the charged pions from decays of Ξ^{*0}.

Since pions and protons from weak decay of Λ ($c\tau = 7.89$ cm [1]) and pions from weak decay of Ξ^{-} ($c\tau = 4.91$ cm [1]) are produced away from the PV, specific topological and

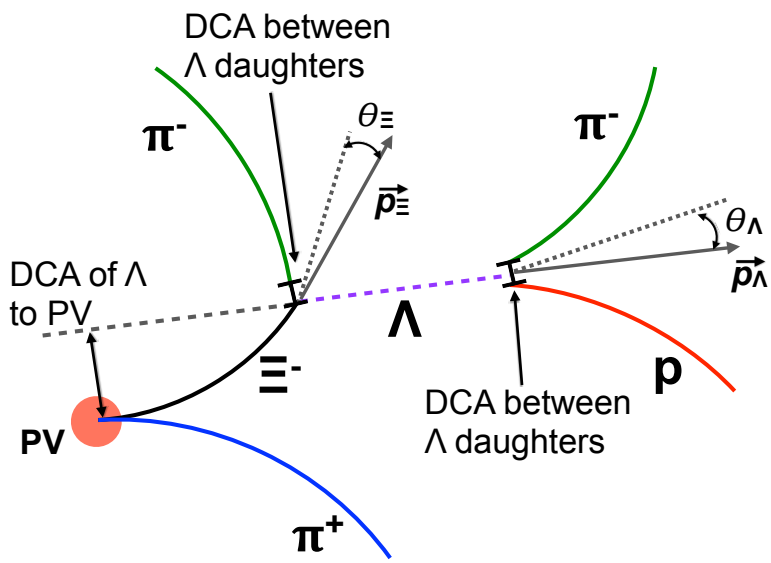

Figure 23: Sketch of the decay modes for Ξ^{*0} and depiction of the track and topological selection criteria.

track selection criteria, as summarized in Table 10, were applied [6, 7, 45].

Topological cuts	p–Pb	Pb–Pb
DCA$_r$ of Λ decay products to PV	> 0.06 cm	> 0.11 cm
DCA between Λ decay products	< 1.4cm	< 0.95 cm
DCA of Λ to PV	> 0.015 cm	> 0.06
$\cos\theta_\Lambda$	> 0.875	> 0.998
$r(\Lambda)$	$0.2 < r(\Lambda) < 100$ cm	$0.2 < r(\Lambda) < 100$ cm
$\lvert M_{p\pi} - m_\Lambda \rvert$	< 7 MeV/c^2	< 7 MeV/c^2
DCA$_r$ of pion (from Ξ^-) to PV	> 0.015 cm	> 0.035 cm
DCA between Ξ^- decay products	< 1.9 cm	< 0.275
$\cos\theta_\Xi$	> 0.981	> 0.9992
$r(\Xi^-)$	$0.2 < r(\Xi^-) < 100$ cm	$0.2 < r(\Xi^-) < 100$ cm
$\lvert M_{\Lambda\pi} - m_\Xi \rvert$	< 7 MeV/c^2	< 7 MeV/c^2

Table 10: Topological and track selection criteria.

.

In the analysis of Ξ^{*0}, Λ and π from Ξ^- were selected with a DCA of less than 1.9 cm and with a DCA$_r$ to the PV greater than 0.015 cm. The Λ daughter particles (π and p)

were required to have a DCA_r to the PV greater than 0.06 cm, while the DCA between the two particles was required to be less than 1.4 cm. Cuts on the invariant mass, the cosine of the pointing angle (θ_Λ, θ_Ξ) and the radius of the fiducial volume ($r(\Lambda)$, $r(\Xi)$) in Table 10 were applied to optimize the balance of purity and efficiency of each particle sample.

5.1.3 Particle identification

PID selection criteria are applied for

1. $\pi^{\pm}$ (last emitted π) and proton from Λ
2. $\pi^{\pm}$ (second emitted π) from $\Xi^{\pm}$
3. $\pi^{\pm}$ (first emitted π) from $\Xi(1530)^0$

by using TPC. On TPC dE/dx versus momentum distribution, 3σ cuts are applied to TPC for selecting each of the particles. The TPC dE/dx selection allows to have better signal with $\sim$20% increase of significance.

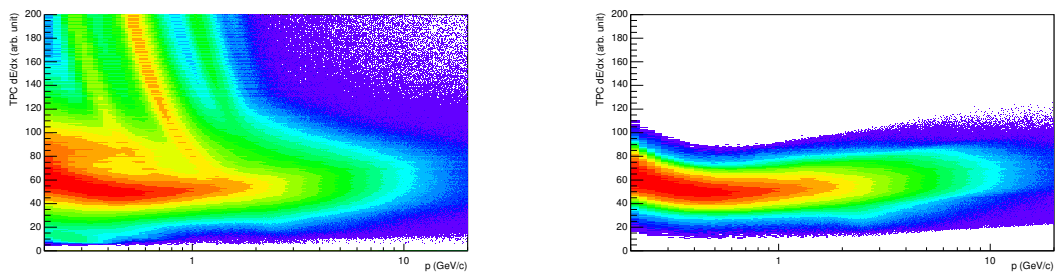

Figure 24: TPC dE/dx as function of transverse momentum for total (top) and selected first emitted π in 3σ (bottom)

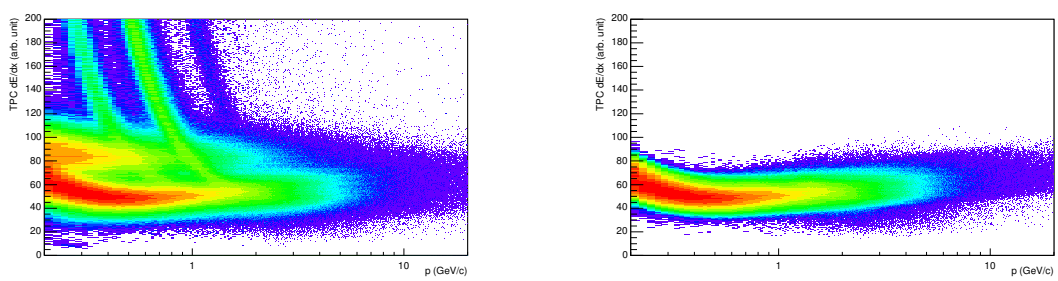

Figure 25: TPC dE/dx as function of transverse momentum for total (top) and selected second emitted π in 3σ(bottom)

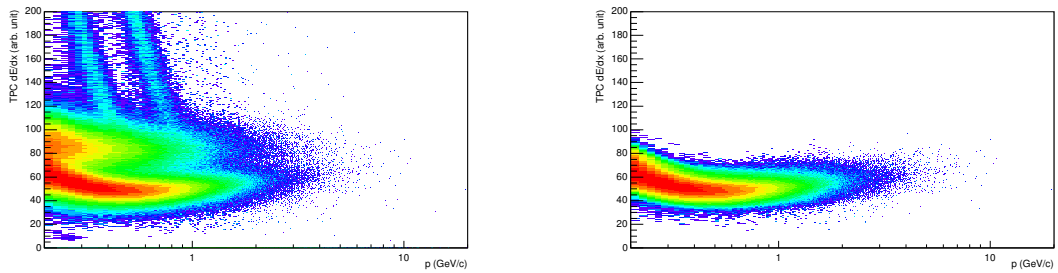

Figure 26: TPC dE/dx as function of transverse momentum for total (top) and selected last emitted π in 3σ(bottom)

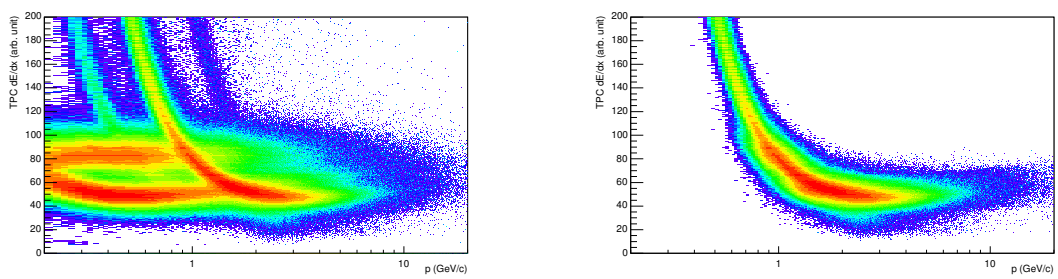

Figure 27: TPC dE/dx as function of transverse momentum for total (top) and selected proton in 3σ(bottom)

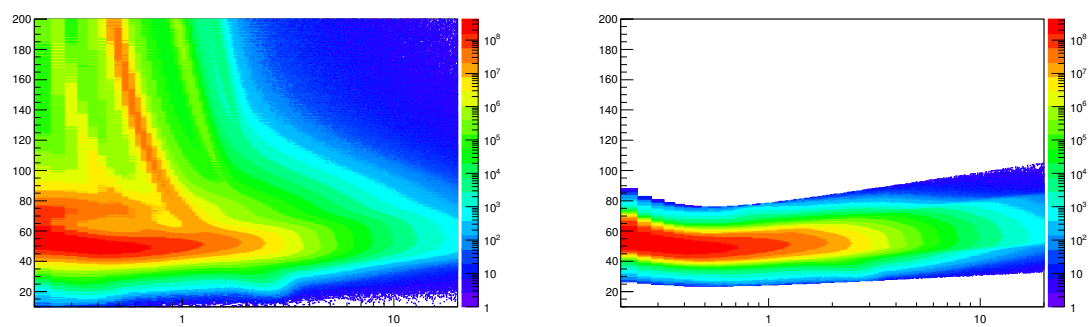

Figure 28: TPC dE/dx as function of transverse momentum for total (top) and selected first emitted π in 3σ (bottom)

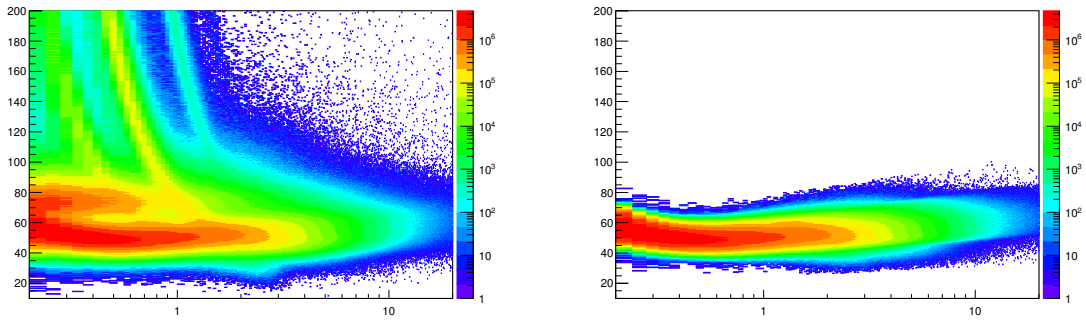

Figure 29: TPC dE/dx as function of transverse momentum for total (top) and selected second emitted π in 3σ(bottom)

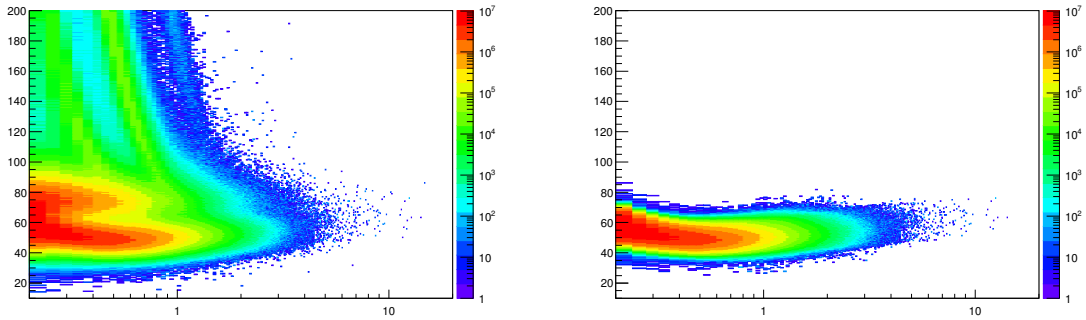

Figure 30: TPC dE/dx as function of transverse momentum for total (top) and selected last emitted π in 3σ(bottom)

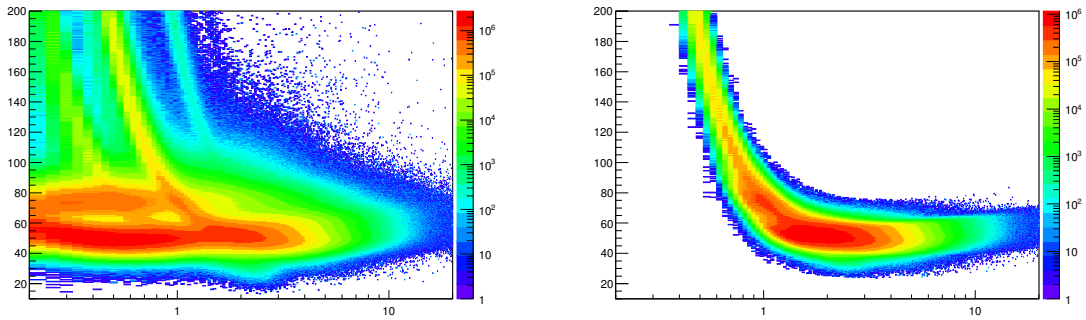

Figure 31: TPC dE/dx as function of transverse momentum for total (top) and selected proton in 3σ(bottom)

5.1.4 Signal extraction

The Ξ^{*0} signals were reconstructed by invariant-mass analysis of candidates for the decay products in each transverse momentum interval of the resonance particle, and for each multiplicity class. The $\Xi^-\pi^+(\Xi^+\pi^-)$ invariant mass distribution is reported in Figure 5.1.4 for semi-central events (20-40%) in p–Pb collisions and Figure 5.1.4 for central events(0-10%) in Pb–Pb collisions.

Since the resonance decay products originate from a position which is indistinguishable from the PV, a significant combinatorial background is present. In order to extract $\Xi(1530)^0$ signal it is necessary to remove or, at least reduce, the combinatorial background. For this analysis, this has been done with the event mixing (EM) technique, by combining uncorrelated decay products 20 different events in p–Pb (5 different events in Pb–Pb). The events for the mixing have been selected by applying the similarity criteria to minimise distortions due to different acceptances and to ensure a similar event structure, only tracks from events with similar vertex positions z ($|\Delta z| < 1$ cm) and track multiplicities n ($|\Delta n| < 10$) were taken.

The mixed-event background distributions were normalised to two fixed regions, $1.49 < M_{\Xi\pi} < 1.51$ GeV/c^2 and $1.56 < M_{\Xi\pi} < 1.58$ GeV/c^2 , around the Ξ^{*0} mass peak (Figure 5.1.4 and 5.1.4). These regions were used for all p_{T}intervals and multiplicity classes, because the background shape is reasonably well reproduced in these regions and the invariant-mass resolution of the reconstructed peaks appears stable, independently of p_{T}. The uncertainty on the normalisation was estimated by varying the normalisation regions and is included in the quoted systematic uncertainty for the signal extraction (Section5.4).

After the background subtraction, the resulting distribution is shown in Figure 5.1.4 and 5.1.4. In order to obtain raw yields, a combined fit of a first-order polynomial for

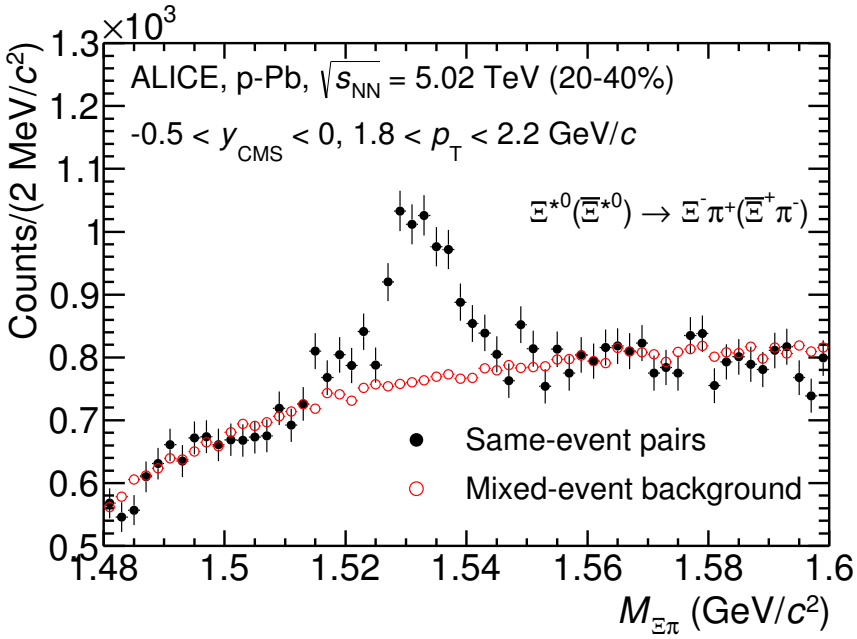

Figure 32: The $\Xi^{\mp}\pi^{\pm}$ invariant mass distribution (Same-event pairs) in 1.8< p_{T}<2.2 GeV/c and for the multiplicity class 20-40%. The background shape, using pairs from different events (Mixed-event background), is normalised to the counts in $1.49 < M_{\Xi\pi} < 1.51$ GeV/c^2 and $1.56 < M_{\Xi\pi} < 1.58$ GeV/c^2 .

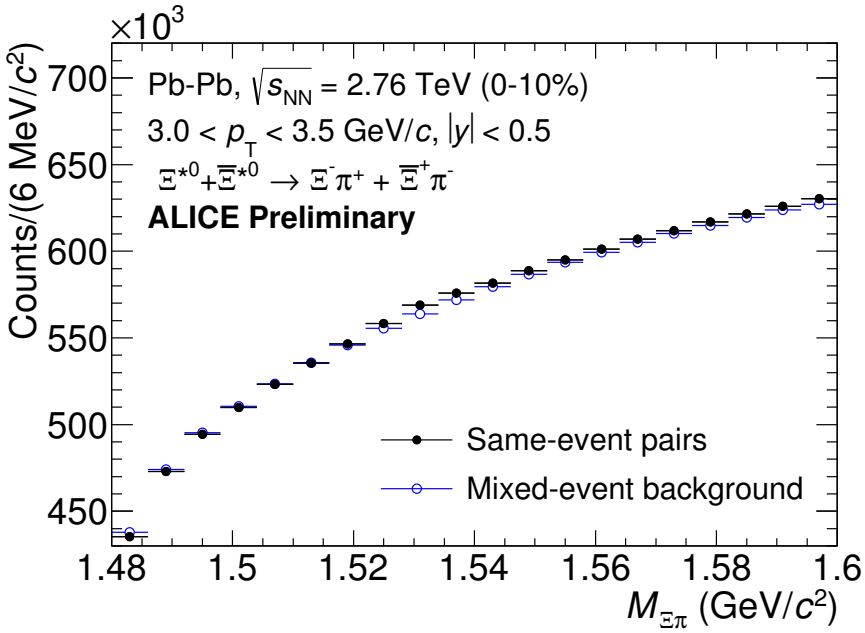

Figure 33: The $\Xi^{\mp}\pi^{\pm}$ invariant mass distribution (Same-event pairs) in 3.0< p_{T}<3.5 GeV/c and for the centrality class 0-10%. The background shape, using pairs from different events (Mixed-event background), is normalised to the counts in $1.49 < M_{\Xi\pi} < 1.51$ GeV/c^2 and $1.56 < M_{\Xi\pi} < 1.58$ GeV/c^2 .

the residual background and a Voigtian function (a convolution of a Breit-Wigner and a Gaussian function accounting for the detector resolution) for the signal was used. The mathematical form of fit function used in anaysis is:

$$f(M_{\Xi\pi}) = \frac{Y}{2\pi}\frac{\Gamma_0}{(M_{\Xi\pi}-M_0)^2+\frac{\Gamma_0^2}{4}}\frac{e^{-(M_{\Xi\pi}-M_0)/2\sigma^2}}{\sigma\sqrt{2\pi}} + bg(M_{\Xi\pi}) \tag{7}$$

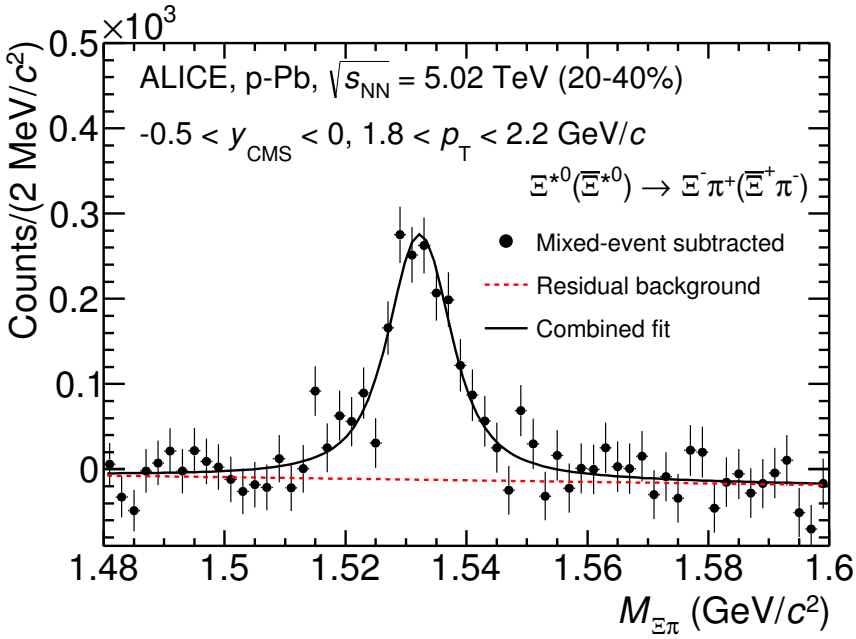

Figure 34: The invariant mass distribution after subtraction of the mixed-event background in p–Pb collisions. The solid curve represents the combined fit, while the dashed line describes the residual background.

The mass parameter of the Voigtian fit (M_0) is left free within the fit range (1.48 GeV/c^2 and 1.59 GeV/c^2). The overall invariant mass width of the Voigtian function is governed by 2 parameters: σ and Γ_0. The σ describes the broadening of the peak due to finite detector resolution while Γ describes the intrinsic width of the resonance itself. The Γ_0 is fixed to the PDG value of 9.1 MeV/c for the$\Xi(1530)^0$. Because of lack of statistics, the σ can be over estimated. Therefore the σ parameter is fixed to value derived from σ in MB events which has largest statistics. The σ as function of p_{T}distribution in MB events is shown in Figure. 36 and we also report invariant mass of $\Xi(1530)^0$ as function of p_{T}in Figure. 37. The $\Xi(1530)^0$ raw yields have been extracted from the fit for the 4 multiplicity

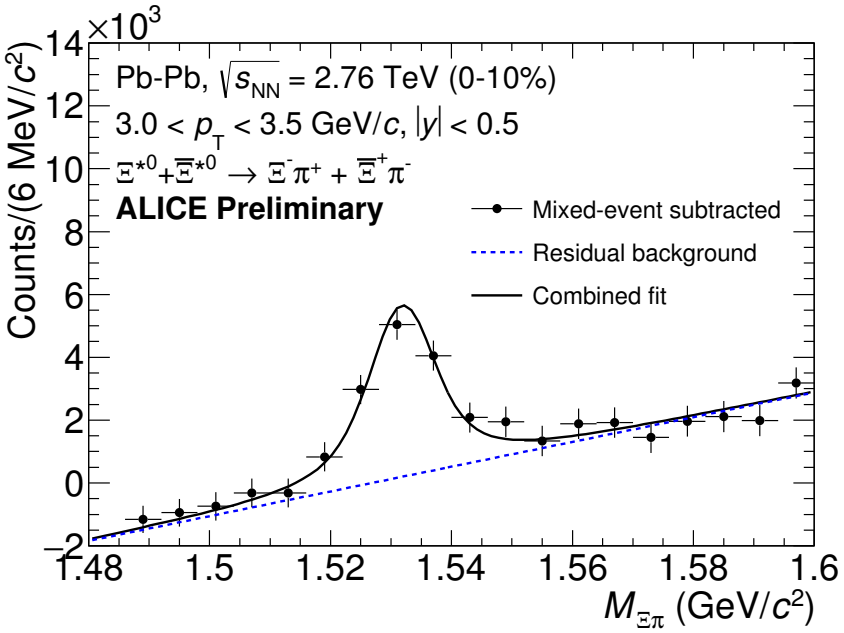

Figure 35: The invariant mass distribution after subtraction of the mixed-event background in Pb–Pb collisions. The solid curve represents the combined fit, while the dashed line describes the residual background.

bins (+ NSD events) in p–Pb and 4 centrality bins in Pb–Pb collisions and the yields as function of $p_{\mathrm{T}}$are shown in Figure 38.

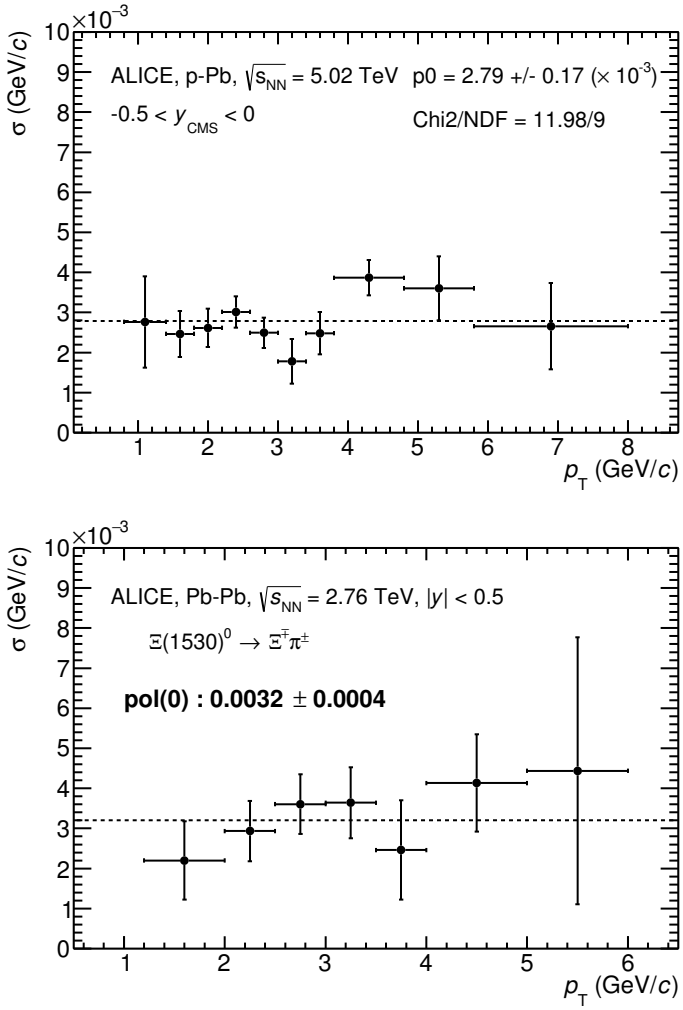

Figure 36: σ fit parameters as a function of p_{T}in MB in p–Pb collisions (top) and in Pb–Pb collisions (bottom).

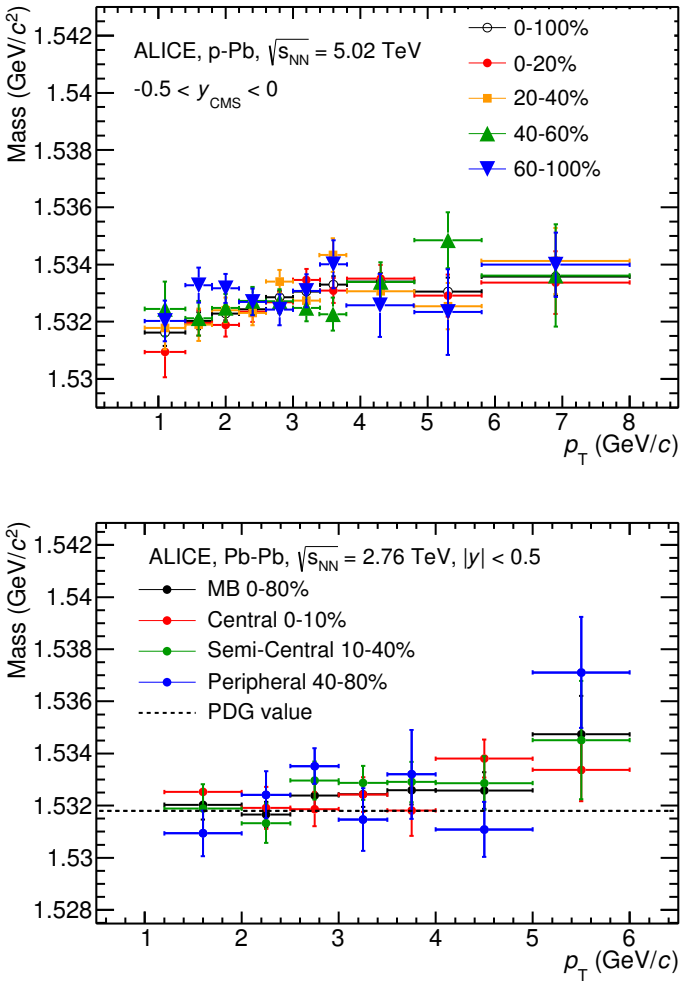

Figure 37: $\Xi(1530)^0$ -mass obtained from fit of the Voigtian peak as a function of p_{T}in each multiplicity classes in p–Pb collisions (top) and the different centrality classes in Pb–Pb (bottom).

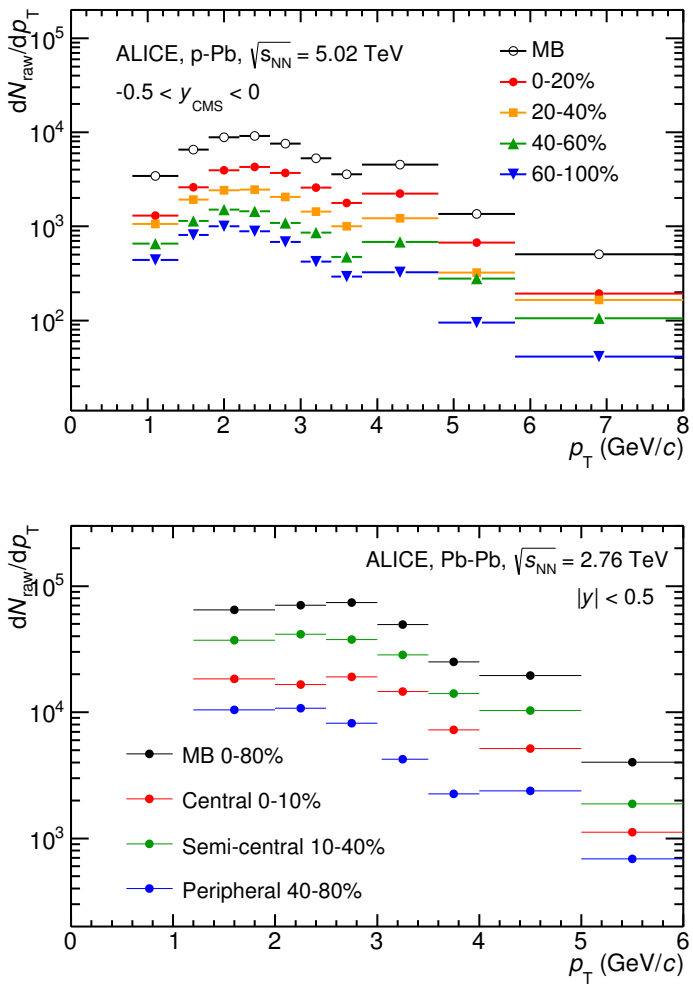

Figure 38: $\Xi(1530)^0$ -raw spectra obtained from fit of the Voigtian peak and a polynomial residual background for different multiplicities in p–Pb collisions (top) and Pb–Pb collisions (bottom). Only the statistical error is reported.

5.2 Efficiency correction

The raw yields were corrected for the geometrical acceptance and the reconstruction efficiency (A $\times$ ϵ) of the detector (Figure. 39). By using the DPMJET 3.05 event generator [46] and the GEANT 3.21 package [47], a sample of about 100 million p–Pb events was simulated and reconstructed in order to compute the corrections. The distributions of $A \times \epsilon$ were obtained from the ratio between the number of reconstructed Ξ^{*0} and the number of generated particle in the same p_{T} and rapidity interval. Since the correction factors for different multiplicity classes are in agreement with those from MB events within statistical uncertainty, the latter were used for all multiplicity classes.

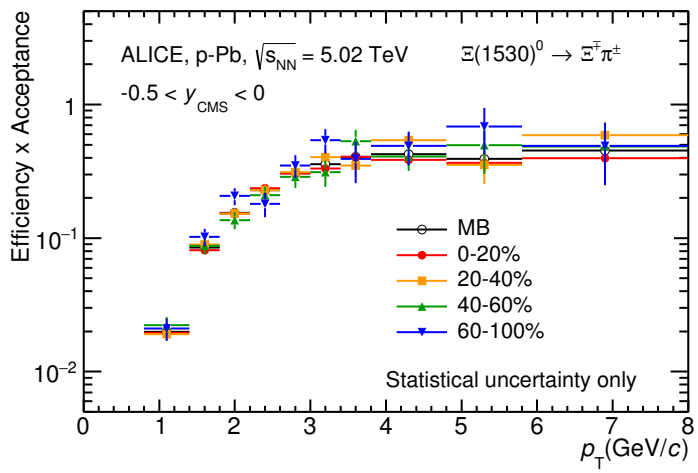

Figure 39: $\Xi(1530)^0$ -raw spectra obtained from fit of the Voigtian peak and a polynomial residual background for different multiplicities. Only the statistical error is reported.

Because the generated $\Xi(1530)^0$ spectra have different shapes than the measured $\Xi(1530)^0$ spectra, it is necessary to weight the generated and reconstructed $\Xi(1530)^0$ spectra in these simulations. Fig. 40 shows the generated and reconstructed $\Xi(1530)^0$ spectra plotted with the (corrected) measured $\Xi(1530)^0$ spectrum for MB events and the Levy fit of that measured spectrum. The generated and measured $\Xi(1530)^0$ spectra have different behaviours for the range $0.5 < p_{\mathrm{T}} < 1$ GeV/c. The generated $\Xi(1530)^0$ spectrum decreases with increasing p_{T}over this range, while the fit of the measured $\Xi(1530)^0$ spectrum reaches a local maximum in this range. The correction ϵ is observed to change rapidly over this p_{T}range. It is therefore necessary to weight the generated spectrum so that it has the shape of the measured $\Xi(1530)^0$ spectrum (and to apply corresponding weights to the reconstructed $\Xi(1530)^0$ spectrum). An iterative procedure is performed to determine the correct weighting (and therefore the correct ϵ).

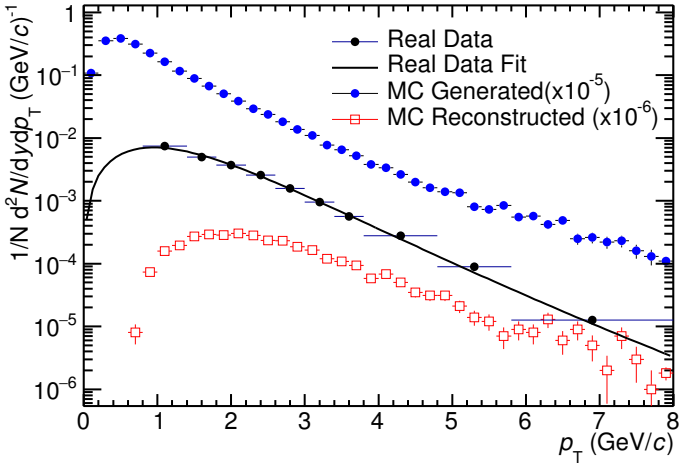

Figure 40: Real corrected $\Xi(1530)^0$ spectrum (black) for the minimum bias with Levy fit (black curve). Also shown are the unweighted generated (blue) and reconstructed (red) $\Xi(1530)^0$ spectra.

1. The unweighted ϵ is calculated.
2. This ϵ is used to correct the measured xis spectrum.
3. The corrected $\Xi(1530)^0$ spectrum is fit.
4. This fit is used to weight the simulated xis spectra. A p_{T}dependent weight is applied to the generated xis spectrum so that it follows the fit. The same weight is applied to the reconstructedxis spectrum.
5. The (weighted) ϵ is calculated.
6. Steps 2-5 are repeated (with the weighted ϵ from step 5 used as the input for step 2) until the ϵ values are observed to change by $< 0.1\%$ (relative) between iterations. It is observed that four iterations are sufficient for this procedure to converge.

Finally, the re-weighted efficiency is obtained and the distribution as function of $p_{\mathrm{T}}$is shown in Figure 41.

In order to obtain the correction factor dedicated in Pb–Pb collisions, MC events are generated using Heavy Ion Jet Interaction Generator (HIJING). The generated events are passed through a GEANT3 model of the ALICE experiment with a realistic description of the detector response. Because we have observed centrality dependent efficiency, the centrality dependent efficiencies have been applied to get corrected raw yield. The reweighing

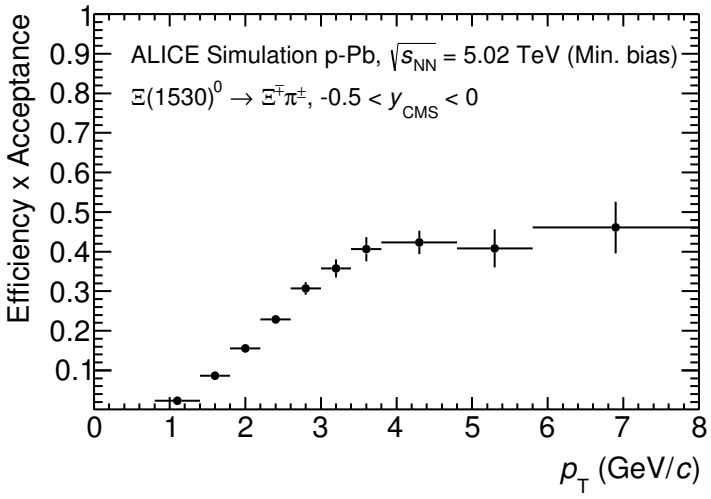

Figure 41: Efficiency as a function of p_{T}in minimum bias events in p–Pb collisions.

approach which was used to correct the efficiency in p–Pb is also applied to the efficiency obtained in Pb-Pb.

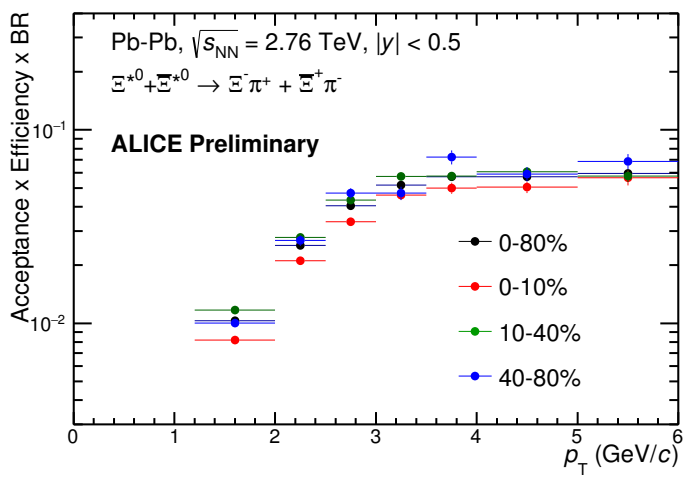

Figure 42: Efficiency as a function of p_{T}in different centrality classes in Pb–Pb collisions

5.3 Corrected p_{T}-spectra

The p_{T} spectrum is by the number of produced particles of a given type in the desired interval of phase-space divided by the number of inelastic collisions. The spectrum is calculated as:

$$\frac{1}{N} \times \frac{d^2N}{dydp_T} = \frac{1}{N_{E,PhysSel}} \times \frac{N_{raw}}{dp_T dy} \frac{1}{\epsilon} \frac{N^{MC}_{total}}{N^{MC}_{post-PV cut}}, \tag{8}$$

where N_E represent the number inelastic collisions, the $\frac{dN}{dydp_T}$ is the yield per range of rapidity y, per range in p_{T}. On the right hand side $\mathrm{N}_{E,PhysSel}$ is the number of events counted by the physics selection trigger. N_{raw} is the raw extracted number of particle in the rapidity and p_{T}bin of width $\Delta y = 0.5$ in p–Pb ($\Delta y = 1.0$ in Pb–Pb) and $\Delta \mathrm{p}_T$, respectively. ϵ is the reconstruction efficiency estimated from Monte Carlo simulations. $\frac{N^{MC}_{total}}{N^{MC}_{post-PV cut}}$ is the ratio of the total number of particle from MC divided by the number of particle from MC after the Primary-Vertex cut is imposed. It takes into account the fraction of particle lost after imposing the PV cut. We notice that for minimum-bias results in p–Pb, we adopted a normalisation such that to provide result from non-single diffractive(NSD) cross-section. The normalisation factor is 0.964 [5]. The obtained spectrum at MB and the spectrums from different multiplicity classes in p–Pb are shown in Figure 43 and different centrality classes in Pb–Pb are shown in Figure 44.

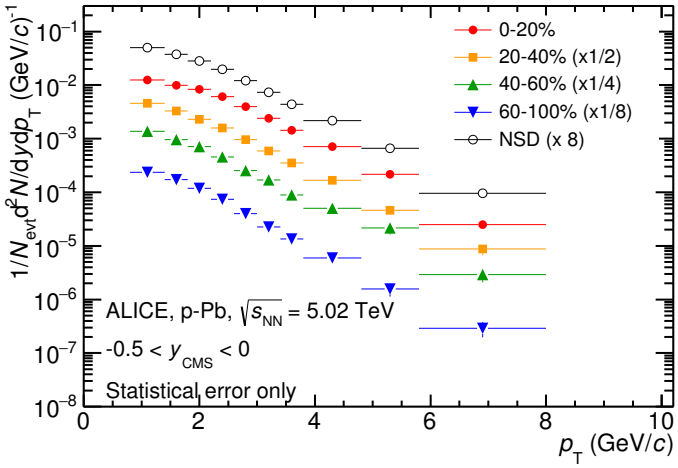

Figure 43: Corrected p_{T}-spectra of $\Xi(1530)^0$ in NSD and different multiplicity classes in p–Pb collisions.

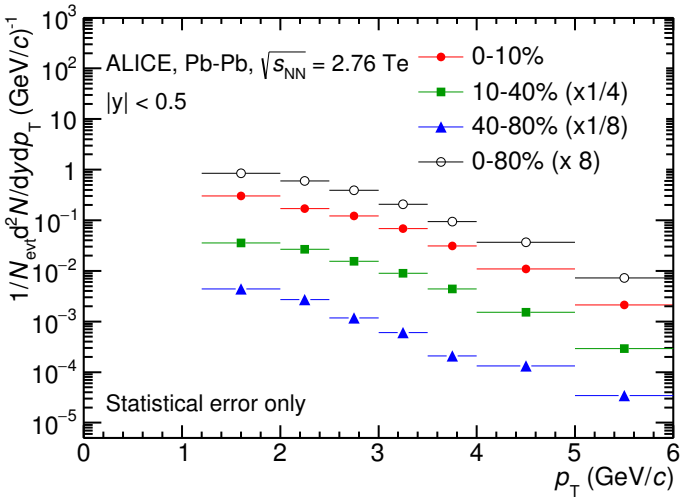

Figure 44: Corrected p_{T}-spectra of $\Xi(1530)^0$ in different centrality classes in Pb-Pb collisions.

5.4 Systematic uncertainties

The systematic uncertainties are calculated in seven principle groups. The procedure to obtain the systematic uncertainties is performed many times by varying the possible permutation of the analysis parameter.The general strategy for evaluating systematic uncertainties is described as following:

1. Choose one set of parameters for the analysis as default
2. Observe the deviation of yield when one parameter is changed
3. The systematic uncertainty is calculated for a given source as the RMS deviation of the available sources.
4. The total systematic uncertainty, taking into account all the different sources, is the sum in quadrature of each source.

To study the systematic effect we repeat the measurement by varying one parameter at a time. A Barlow [48] check has been performed for each measurement to verify whether it is due to a systematic effect or a statistical fluctuation. Let each measurement be indicated by ($y_i \pm \sigma_i$) and the central value (default measurement) by ($y_c \pm \sigma_c$), one can define $\Delta\sigma_i$ (Eq. 9).

$$\Delta\sigma_i = \sqrt{(}|\sigma_i^2 - \sigma_c^2|) \tag{9}$$

Then we calculate $n_i = \Delta y_i / \Delta\sigma_i$, where $\Delta y_i = |y_c$ - $y_i|$. If $n_i \leq 1.0$ then the effects are due to the statistical fluctuation and if $n_i > 1.0$ we apply consistency check. Since the alternate and default measurements are not statistically independent, an alternate measurement which is statistically consistent with the default measurement should not be used in calculating a systematic uncertainty. The difference between the two measurements is $\Delta = y_c$ - y_i. The difference in quadrature of the uncertainties is calculated by Eq. 9. It could be possible to check if $\Delta < \sigma$ and exclude such cases from the systematic uncertainties. However, there can be statistical fluctuations for which $\Delta > \sigma$. If the variations between the default and alternate measurements are purely statistical, the distribution of Δ/σ should be a Gaussian with a mean value that is consistent with zero and a deviation σ consistent with unity. In this analysis, if the mean value is less than 0.1 and σ is less than 1, the variation passes the consistency check.

Only the measurements which passed the Barlow check ($n_i > 1$) are used to determine the systematic uncertainty. For measurements N > 2, the systematic uncertainty has been determined as the RMS (eqn. 10) of the available measurements. If N=2, the absolute difference is assigned as systematic uncertainty.

$$\delta y_{syst.} = \sqrt{\frac{1}{N}\sum_i (y_i - \overline{y})^2} \tag{10}$$

Here N is the total number of available measurements including y_c and $\overline{y}$ is the average of value of the measurements. The measurement did not pass Barlow check, zero systematic uncertainty has been assigned to the value.

By suing the way as explained above, all the main contributions to the systematic uncertainty of particle spectra have been studied. In particular those that comes from signal extraction, topological and kinematical selection cuts, track quality selection and nσ TPC PID variation. the meaning of each source of systematic uncertainty studied is described in the following:

Signal extraction

We have extracted the signal with varying the yield calculating method which contains the method of signal extraction by integrating the Voigtian fit function and bin counting. We also have varied the normalisation range which is related to the invariant mass region where the mixed events distribution is scaled to subtract the combinatorial background and different background estimator such as Like-Sign distribution and polynomial fit was taken account into the systematic source of signal extraction. The systematic uncertainty from signal extraction is sum in quadrature of three sources.

Topological selection

To evaluate the stability of the chosen set of values for the topological cuts, loose and tight cuts have beed defined in order to vary by $\pm 10\%$ respectively. The parameters are changed once at a time. Total systematic uncertainty from topological selection is calculated by summation in quadrature of nine sources.

TPC $\mathrm{N}_{cluster}$ selection

The selection performed for the daughter tracks of the cascade is that $\mathrm{N}_{cluster}$ is larger than 70 and the value has been varied to 60 and 80 in order to estimate the systematic uncertainty due to this selection.

TPC $\mathrm{d}E/\mathrm{d}x$ selection

In order to evaluate any potential effect due to the TPC $\mathrm{d}E/\mathrm{d}x$ selection (U_{PID}), the N_σ selection was varied with N = 2.5 and 3.5.

p_T shape correction

As described in Section 5.2, due to the different shape of the measured and generated $\Xi(1530)^0$ spectra, we have applied reweighing procedure to the generated spectra to have same shape and this correction is added into contributor of systematic uncertainty as p_T shape correction.

Mass window range selection

In order to select $\Xi^\pm$ which is daughter particle of $\Xi(1530)^0$, we apply the mass window

± 7 MeV/c^2 around $\Xi(1530)^0$ mass on $\Lambda\pi$ invariant mass distribution. The boundaries has been varied to ± 6 MeV/c^2 and ± 8 MeV/c^2 to estimate systematic uncertainty.

Vertex range selection

The distribution of vertex-z is shown in Fig.20. The cut on |Vz| was varied from the nominal $\pm$10cm to $\pm$9cm, $\pm$11cm.

Material Budget and hadronic cross section

A possible source of uncertainty comes from the description of the material, active (detecting area) or dead (structure and cable), that the particles cross during their travel in the MC with respect to the real material present in the detector. Such description could affect the reconstruction efficiency in different aspects (e.g. multiple scattering, energy loss). The value estimated by Ξ analysis [23] has been used in this study which gives 4% systematic uncertainty. In case of systematic uncertainty from hadronic cross section, we have inherited the value studied in previous measurement[49] which amount is 1%.

Tracking efficiency

Systematic uncertainties from tracking efficiency from ITS + TPC combined track were assigned as 3% in p–Pb and 4% in Pb–Pb collision system.[49]
(https://twiki.cern.ch/twiki/bin/view/ALICE/TrackingEfficiencyCharged)

Finally, total systematic uncertainty is sum in quadrature of sources listed above. Figure 45 and Figure 46 show the total systematic uncertainty in minimum bias event and different multiplicity classes in p–Pb collisions, respectively. Again, Figure 47 and Figure 48 present the total systematic uncertainty in minimum bias event and different centrality classes in Pb–Pb collisions.

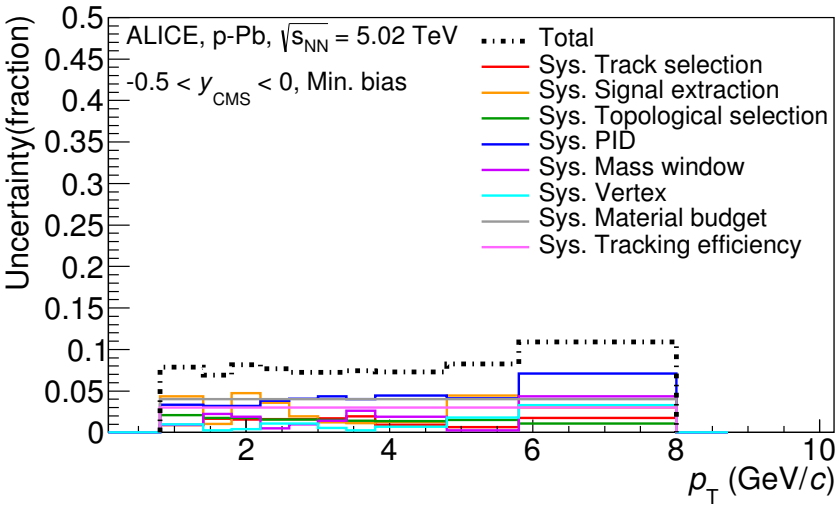

Figure 45: Summary of the contributions to the systematic uncertainty in minimum bias events in p–Pb collisions. The dashed black line is the sum in quadrature of all the contributions.

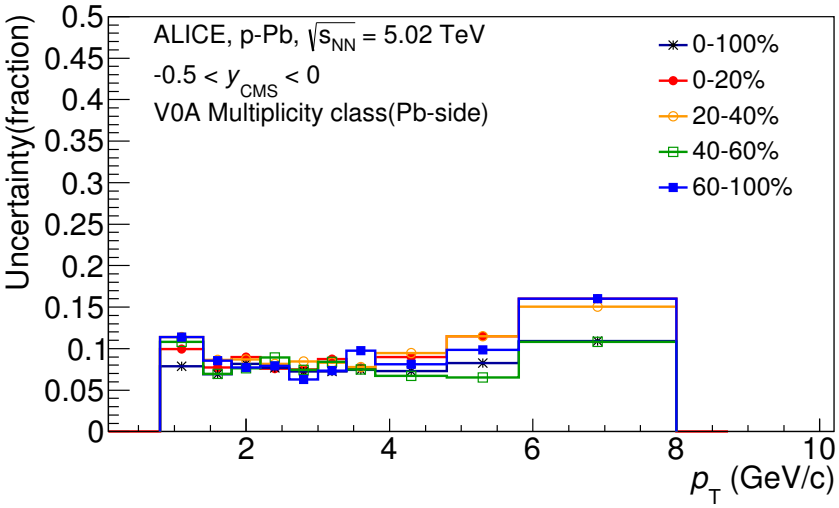

Figure 46: Systematic uncertainties for each multiplicity classes in p–Pb collisions.

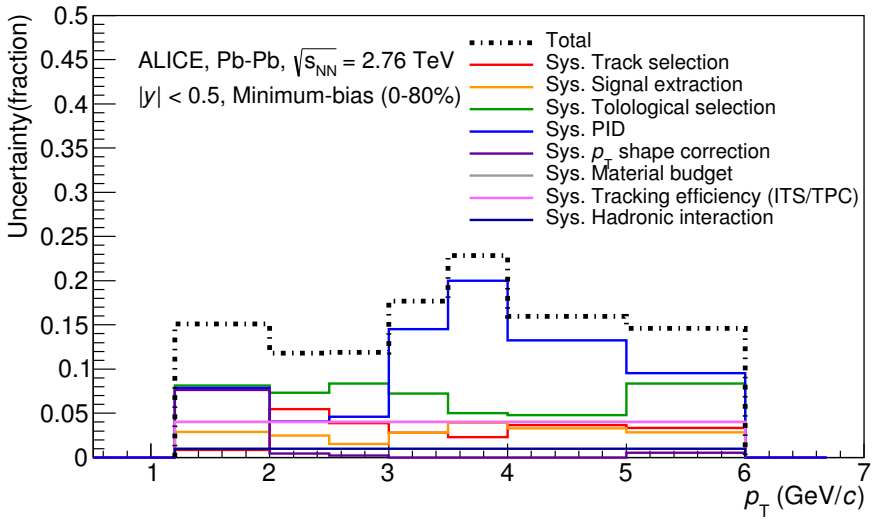

Figure 47: Summary of the contributions to the systematic uncertainty in minimum bias events in Pb–Pb collisions. The dashed black line is the sum in quadrature of all the contributions.

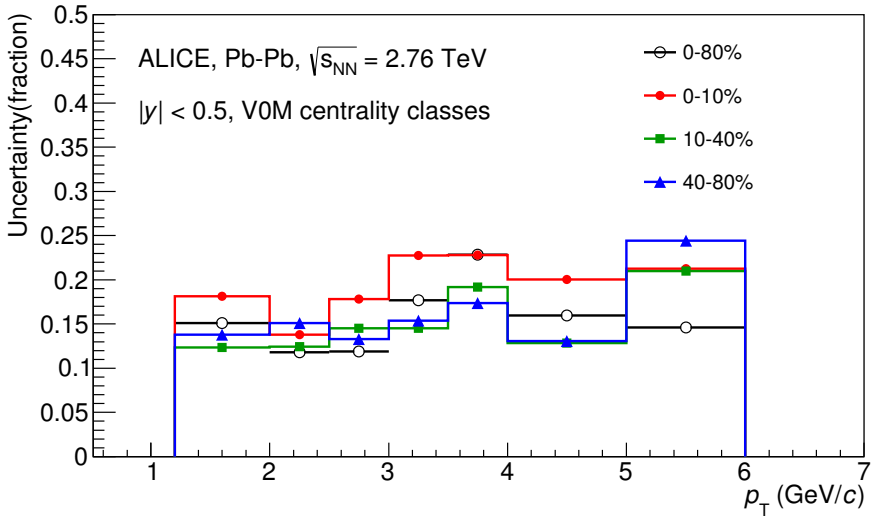

Figure 48: Systematic uncertainties for each multiplicity classes.

Source of uncertainty	p-Pb	Pb-Pb
p_{T}-dependent		
Tracking efficiency	3%	4%
Tracks selection	1-2%	1-5%
Topological selection	1-2%	5-8%
PID	3-7%	4-20%
Signal extraction	1-5%	1-4%
p_{T} shape correction	-	0-8%
Mass window ($\Xi^{\pm}$)	4%	-
Vertex selection	3%	-
p_{T}-independent		
Hadronic interaction	-	1%
Material budget	4%	4%
Branching ratio	0.3%	0.3%
Total	8-12%	9-25 %

Table 11: Summary of the systematic uncertainties on the differential yield, $\mathrm{d}^2N/(\mathrm{d}p_{\mathrm{T}}\mathrm{d}y)$. Minimum and maximum values in all p_{T} intervals and multiplicity classes in p–Pb, centrality classes in Pb–Pb are shown for each source.

5.5 $\Xi(1530)^0$ transverse momentum spectra

The raw yield shown in Figure 43 and 44 have been corrected for efficiency as described in section 5.2. The measured spectra for $(\Xi(1530)^0 + \overline{\Xi(1530)^0})/2$ are reported in Figure 49 for p–Pb collisions and Figure 50 for Pb–Pb collisions. The statistical and systematic uncertainties are reported respectively as the error bars and the boxes on the plot. The corrected yields for p–Pb collisions are measured with $0.8 < p_{\mathrm{T}} < 8.0$ GeV/c while the yields for Pb–Pb collisions are obtained with $1.2 < p_{\mathrm{T}} < 6.0$ GeV/c due to difficulty of signal extraction in low and high p_{T} region.

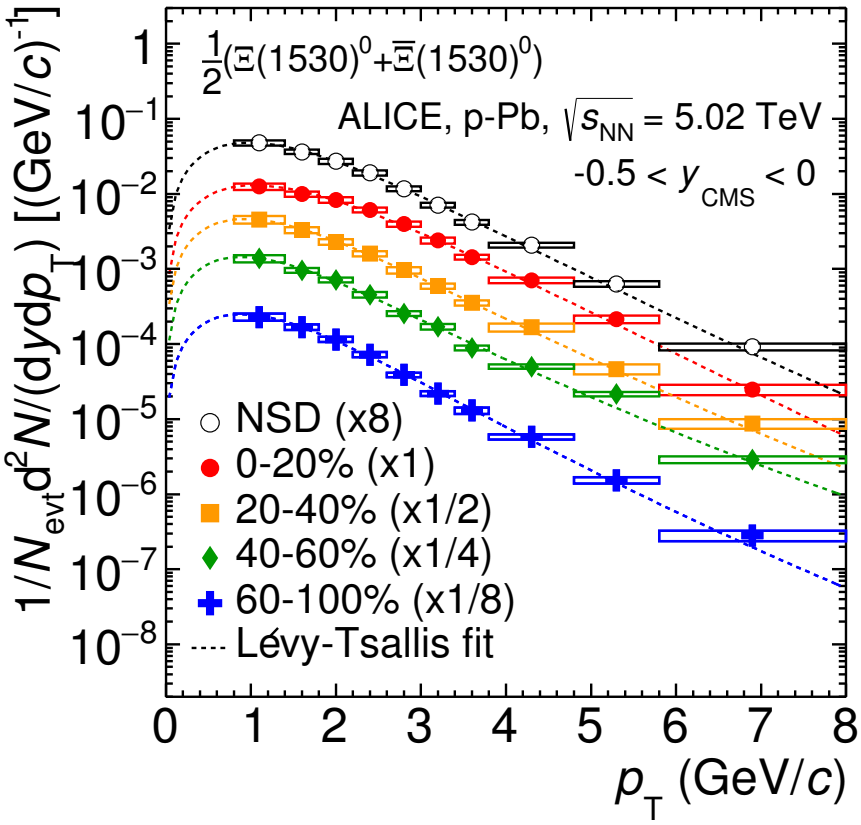

Figure 49: Corrected yields as function of p_T in NSD events and multiplicity dependent event classes in p–Pb collision system. Statistical uncertainties are presented as bar and systematical uncertainties are plotted as boxes.

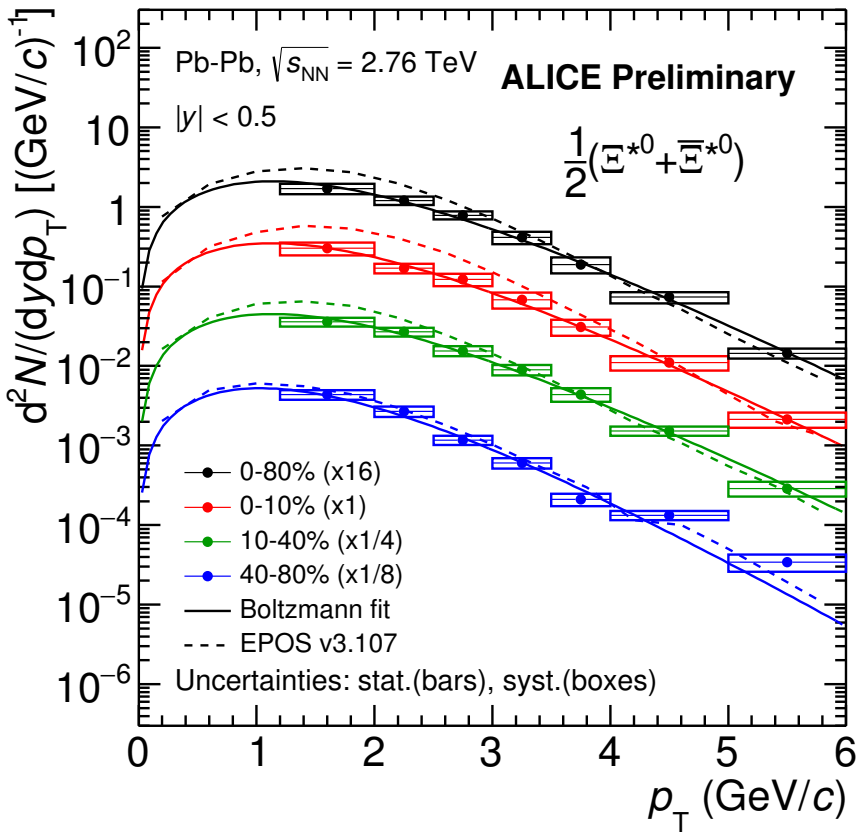

Figure 50: Corrected yields as function of p_T in different centrality classes in Pb–Pb collision system. Statistical uncertainties are presented as bar and systematical uncertainties are plotted as boxes.

6 Further results and discussion

The transverse momentum distributions of double-strange hyperon resonances, $\Xi(1530)^0$, produced in p–Pb collisions at $\sqrt{s_{\rm NN}}$= 5.02 TeV and Pb–Pb collisions at $\sqrt{s_{\rm NN}}$= 2.76 TeV were measured in the mid-rapidity range and they have been already presented in Chapter 5. From the measurement, the $\langle p_{\rm T}\rangle$ and integrated particle yield ratios with system size have been obtained. In the present Chapter these results are compared with model predictions and discussed in connection with the following topics:

- Mean transverse momentum studies
- Study of particle production mechanism in hadronic phase
- Study of strangeness enhancement

Most of the theoretical aspects related to these topics and, in particular, the description of the models already have been adrressed in Chapter 2.

6.1 Mean transverse momentum

Figure 51 shows the mean transverse momentum $\langle p_{\rm T}\rangle$ as a function of mean charged-particle multiplicity density $\langle {\rm d}N_{\rm ch}/{\rm d}\eta_{\rm lab}\rangle$ at midrapidity. The results for $\Xi(1530)^0$ are compared with those for other hyperons observed in p–Pb collisions at $\sqrt{s_{\rm NN}}$= 5.02 TeV [4, 6].

Increasing trends from low to high multiplicities are observed for all hyperons. The mean transverse momenta increase by 20% as the mean charged-particle multiplicity increases from 7.1 to 35.6. This result is similar to the one obtained for the other hyperons. Furthermore, a similar increase has been observed also for $\rm K^{\pm}$, $\rm K^0_S$, $\rm K^*(892)^0$ and ϕ [5], whereas protons are subject to a larger ($\sim$ 33%) increase in the given multiplicity range, as discussed also in Ref. [4].

In all multiplicity classes, the $\langle p_{\rm T}\rangle$ follows an approximate mass ordering:

- $\langle p_{\rm T}\rangle_{\Lambda} < \langle p_{\rm T}\rangle_{\Xi^-} \simeq \langle p_{\rm T}\rangle_{\Sigma^{*\pm}} < \langle p_{\rm T}\rangle_{\Xi^{*0}} < \langle p_{\rm T}\rangle_{\Omega^-}$

The $\langle p_{\rm T}\rangle$ of $\Sigma^{*\pm}$ looks systematically lower than the $\langle p_{\rm T}\rangle$ of Ξ^-, despite the larger mass of $\Sigma^{*\pm}$. The uncertainties, however, are too large to draw any conclusion on possible hints of violation of the mass hierarchy. This hierarchy of mass-ordering, also including D^0 and J/ψ in the comparison, is displayed in Figure 52. Note, however, that the D^0 and J/ψ were measured in different rapidity ranges: $|y_{\rm CMS}| < 0.5$ [8] ($|y_{\rm CMS}| < 0.9$ [9]) for D^0 (J/ψ) in pp and $-0.96 < y_{\rm CMS} < 0.04$ [8] ($-1.37 < y_{\rm CMS} < 0.43$ [10]) for D^0 (J/ψ) in p–Pb, and the results for D^0 and J/ψ in p-Pb collisions are for the 0-100% multiplicity class. This mass dependence is observed in both p–Pb and pp collisions. It was observed also by the STAR collaboration [50] in MB pp, MB d–Au and central Au–Au collisions.

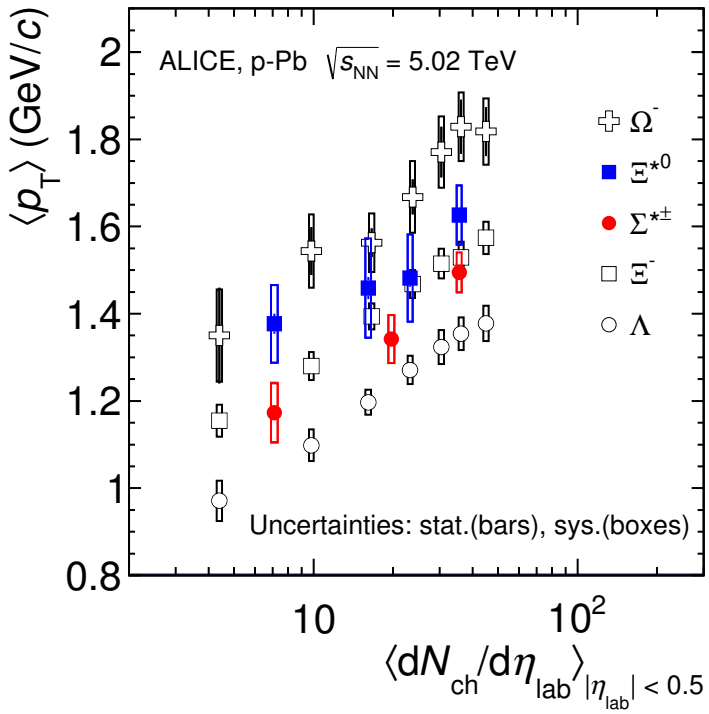

Figure 51: Mean transverse momenta $\langle p_{\mathrm{T}} \rangle$ of Λ, Ξ^-, $\Sigma^{*\pm}$, Ξ^{*0} and Ω^- in p–Pb collisions at $\sqrt{s_{\mathrm{NN}}}$= 5.02 TeV as a function of mean charged-particle multiplicity density $\langle \mathrm{d}N_{\mathrm{ch}}/\mathrm{d}\eta_{\mathrm{lab}} \rangle$, measured in the pseudorapidity range $\mid \eta_{\mathrm{lab}} \mid < 0.5$. The results for Λ, Ξ^- and Ω^- are taken from [4, 5, 6]. Statistical and systematic uncertainties are represented as bars and boxes, respectively. The Ω^- and Ξ^- points in the 3rd and 4th lowest multiplicity bins are slightly displaced along the abscissa to avoid superposition with the $\Xi(1530)^0$ points.

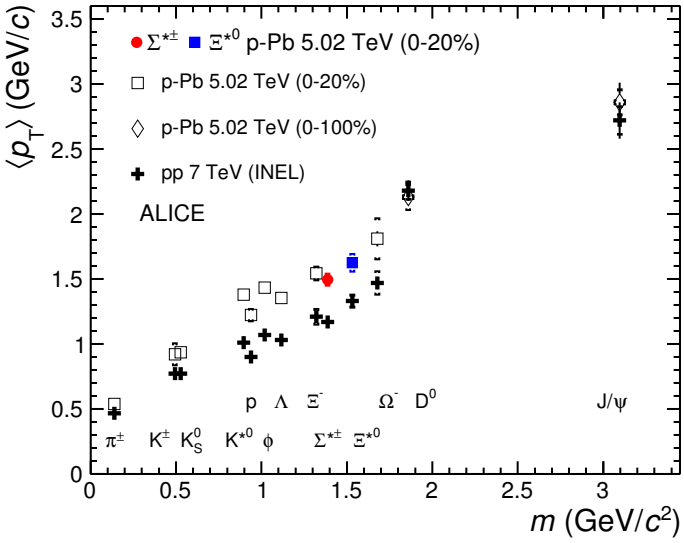

Figure 52: Mass dependence of the mean transverse momenta of identified particles for the $0-20\%$ V0A multiplicity class and with $-0.5 < y_{\rm CMS} < 0$ in p–Pb collisions at $\sqrt{s_{\rm NN}}$= 5.02 TeV [4, 6], and in minimum-bias pp collisions at $\sqrt{s} = 7$ TeV [7] with $|y_{\rm CMS}| < 0.5$. Additionally, D^0 and J/ψ results are plotted. The D^0 and J/ψ were measured in different rapidity ranges: $|y_{\rm CMS}| < 0.5$ [8] ($|y_{\rm CMS}| < 0.9$ [9]) for D^0 (J/ψ) in pp and $-0.96 < y_{\rm CMS} < 0.04$ [8] ($-1.37 < y_{\rm CMS} < 0.43$ [10]) for D^0 (J/ψ) in p–Pb. Note also that the results for D^0 and J/ψ in p-Pb collisions are for the 0-100% multiplicity class.

Furthermore, for the light-flavour hadrons, the mean transverse momenta in p–Pb collisions are observed to be consistently higher than those in pp collisions at 7 TeV. The situation for the charm hadrons is different, where $\langle p_{\mathrm{T}} \rangle$ appears compatible between both colliding systems. The discrepancy is likely due to different production mechanisms for heavy and light flavours and to a harder fragmentation of charm quarks. Specifically, the fact that $\langle p_{\mathrm{T}} \rangle$ remains similar in pp and in p–Pb is consistent with an R_{pPb} ratio compatible with unity at all p_{T}[8] for D^0, and/or with the effects of shadowing in p–Pb which reduces the production at low $p_{\mathrm{T}}$and thus increasing the overall $\langle p_{\mathrm{T}} \rangle$ for J/ψ [10]; the small p_{T}hardening expected in pp when going from 5.02 to 7TeV is apparently not enough to counter-balance the situation.

Because of small decrease of the $\langle p_{\mathrm{T}} \rangle$ for proton and Λ relative to those for K^{*0} and ϕ, two different trends for mesons and baryons have been suggested [51]. Even including D^0 and J/ψ, as shown in Figure 52, a different trend for mesons and baryons cannot be convincingly established.

6.2 Particle yield ratios

6.2.1 Integrated yield ratios of excited to ground-state hadrons

The integrated yield ratios of excited to ground-state hyperons [52, 4, 7, 6] with the same strangeness content, for different collision systems and energies, are shown in Figure 53 as a function of system size. The ratio of $\Xi(1530)^0$ to Ξ is flat across the system and it complements the information derived from other resonance measurement for different lifetime which are shown in Figure 54.

The short-lived resonances(ρ, K* and Λ*) which exhibit suppression from peripheral to central lead-lead collisions and with respect to thermal model in central lead-lead collisions. Currently favored explanation of is dominance of elastic re-scattering of decay daughters over regeneration in the hadronic phase.

The constant behavior of the yield ratios of excited to ground-state hyperons with same strangeness content ($\Xi(1530)^0$ and Φ) indicates that neither regeneration nor re-scattering dominates with increasing collision system size because of its longer-lifetime.

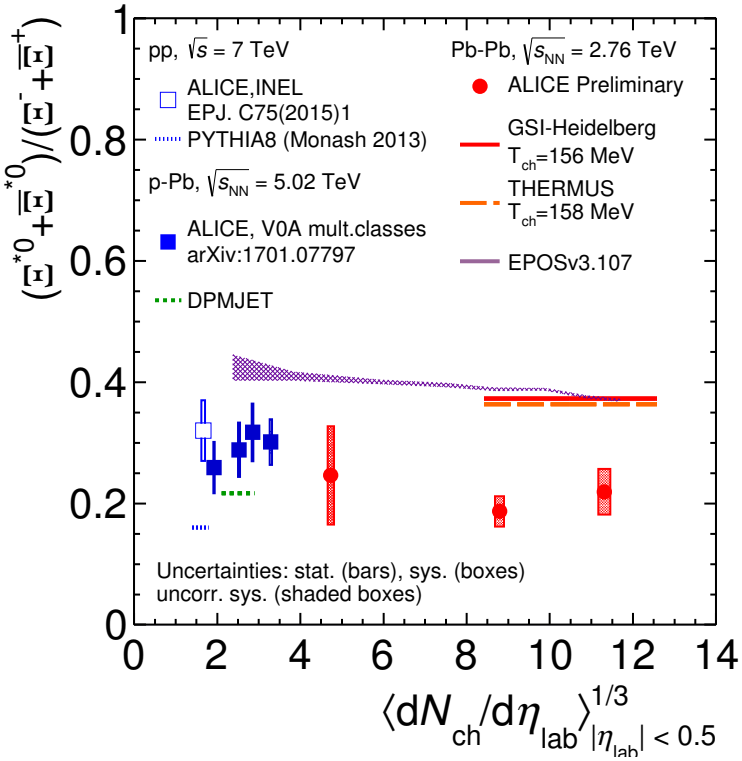

Figure 53: Ratio of $\Xi(1530)^0$ to Ξ^- measured in pp [7], p–Pb [4, 6] and Pb–Pb collisions as a function of $\langle \mathrm{d}N_{\mathrm{ch}}/\mathrm{d}\eta_{\mathrm{lab}} \rangle$ measured at midrapidity. Statistical uncertainties (bars) are shown as well as total systematic uncertainties (hollow boxes) and systematic uncertainties uncorrelated across multiplicity (shaded boxes). A few model predictions are also shown as lines at their appropriate abscissa.

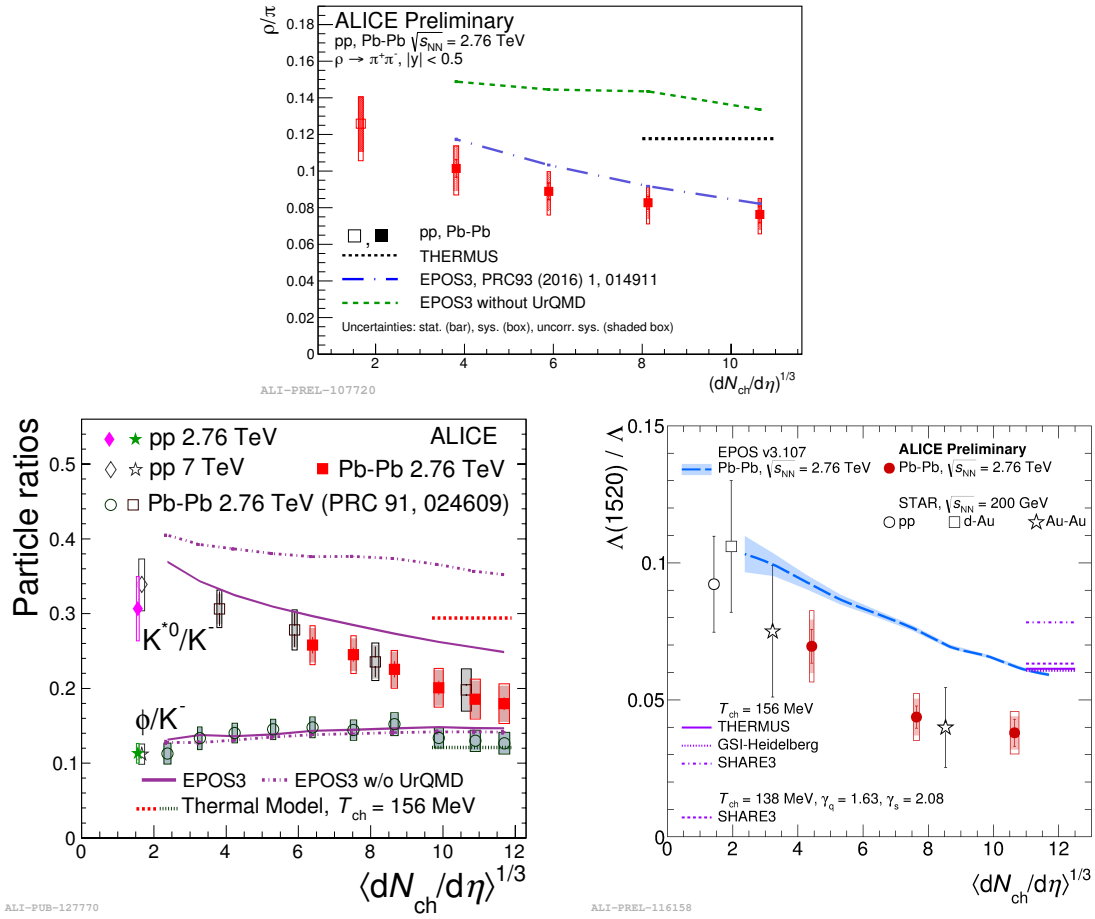

Figure 54: Ratio of ρ/π(Up), K*/K, ϕ/K(Left bottom) and $\Lambda*/\Lambda$ with system size measured at mid-rapidity. Statistical uncertainties (bars) are shown as well as total systematic uncertainties (hollow boxes) and systematic uncertainties uncorrelated across multiplicity (shaded boxes). A few model predictions are also shown as lines at their appropriate abscissa.

6.3 Integrated yield ratios to pion

The integrated yield ratios of excited hyperons to pions are shown in Figure 55 to study the evolution of relative strangeness production yields with increasing collision system size. The ratio of $\Xi(1530)^0$ to Ξ is observed to be increase from pp to p–Pb collisions system and then, decrease from peripheral to central Pb–Pb collision. The QCD-inspired predictions like PYTHIA for pp [53] and DPMJET for p–Pb [46] clearly underestimate the observed yield ratios, while the statistical one seems to be comparable with results from high multiplicity in p–Pb but the ratio in Pb–Pb is below with respect to the model. The results in pp and p–Pb collisions are consistent with previous observation of ground-state hyperons to pion ratios. The Figure 56 presents particle yield ratios to pions of strange and multi-strange hadrons normalized to the values measured in pp collisions. As shown in the Figure 56, the $\Xi(1530)^0$ to pion ratios follow the trend of Ξ pi as function of $\langle \mathrm{d}N_{\mathrm{ch}}/\mathrm{d}\eta_{\mathrm{lab}} \rangle$ and indicate that the strangeness enhancement observed in p–Pb collisions depends predominantly on the strangeness content, rather than on the hyperon mass.

The Figure 57 also shows the hyperon-to-pion ratios and compared with model predictions. The

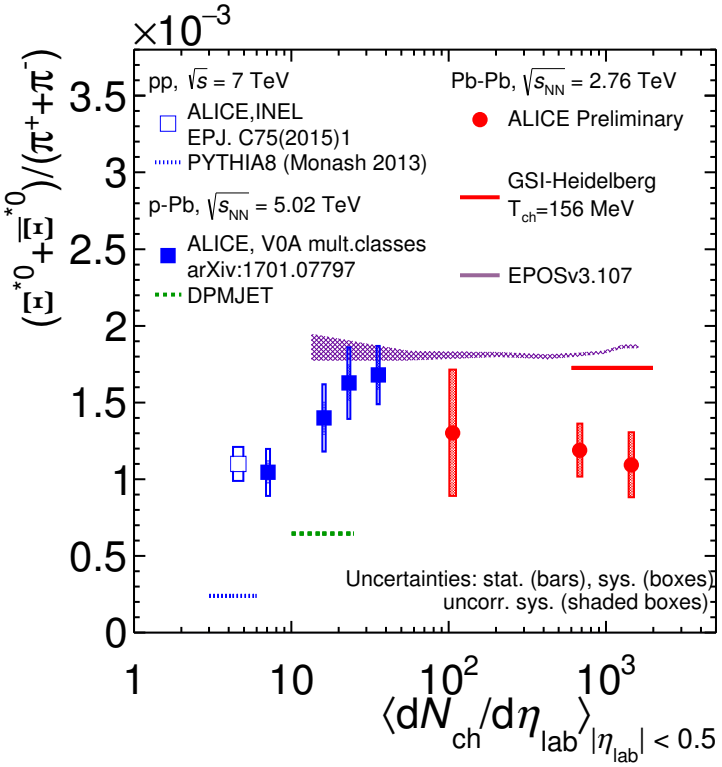

Figure 55: Ratio of $\Xi(1530)^0$ to $\pi^{\pm}$, measured in pp [11] and p–Pb [7] collisions, as a function of the average charged particle density ($\langle \mathrm{d}N_{\mathrm{ch}}/\mathrm{d}\eta_{\mathrm{lab}} \rangle$) measured at mid-rapidity. Statistical uncertainties (bars) are shown as well as total systematic uncertainties (hollow boxes) and systematic uncertainties uncorrelated across multiplicity (shaded boxes). A few model predictions are also shown as lines at their appropriate abscissa.

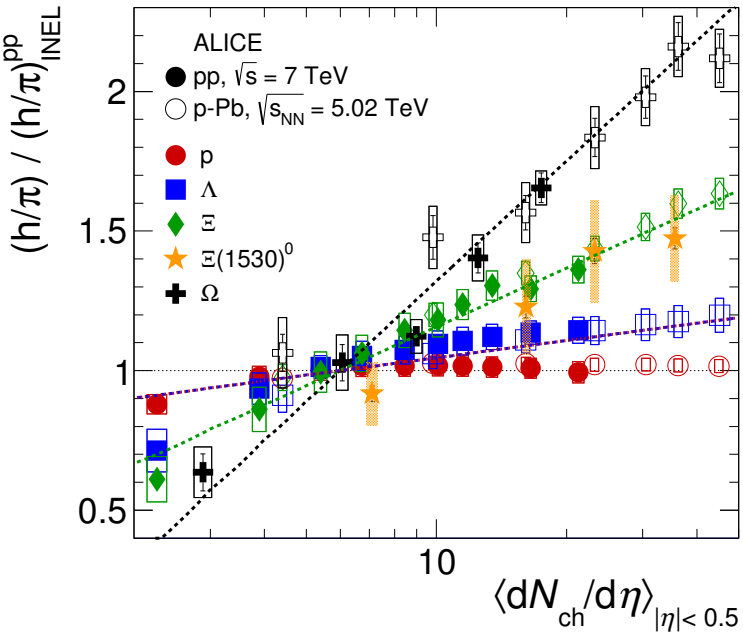

Figure 56: Particle yield ratios to pions of strange and multi-strange hadrons normalized to the values measured in pp collisions, both in pp and in p–Pb collisions. The common systematic uncertainties cancel in the double-ratio. The empty boxes represent the remaining uncorrelated uncertainties. The lines represent a simultaneous fit of the results with the empirical scaling formula in Equation **??**.

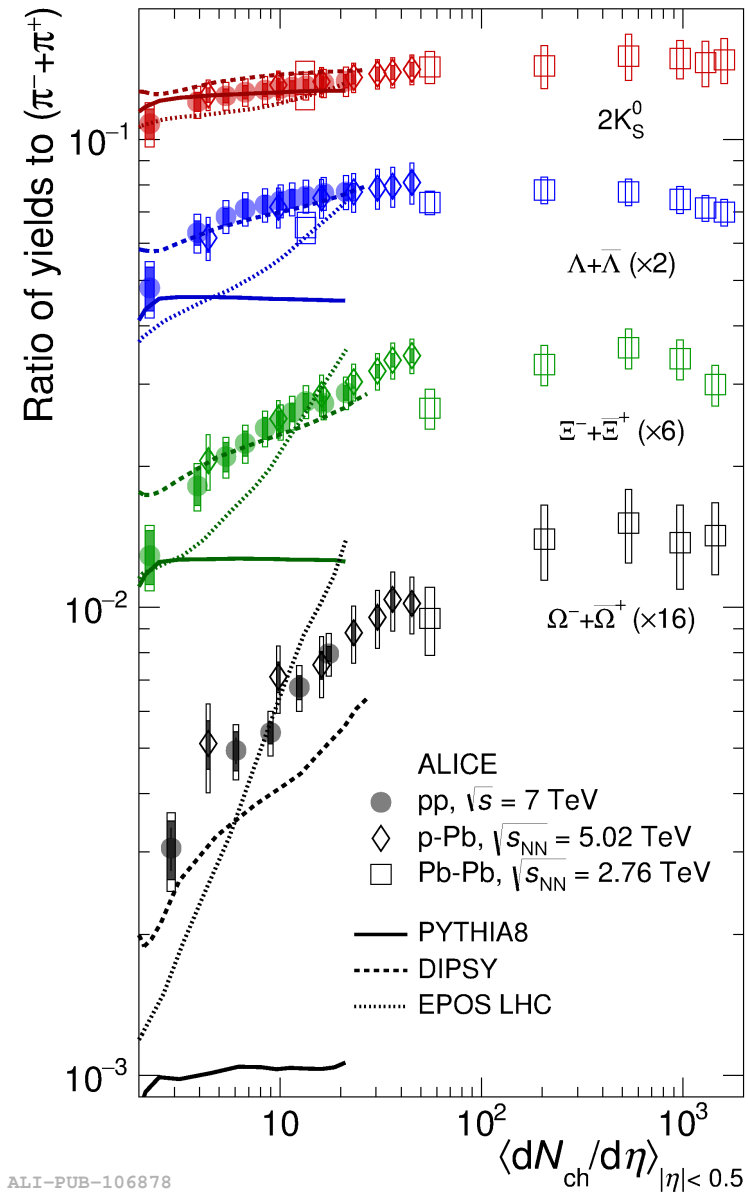

Figure 57: p_T-integrated yield ratios of strange and multi-strange hadrons to $(\pi^+ + \pi^-)$ as a function of $\langle dN_{ch}/d\eta_{lab} \rangle$ measured in the rapidity interval $|\eta| < 0.5$. The empty and dark-shaded boxes show the total systematic uncertainty and the contribution uncorrelated across multiplicity bins, respectively. The values are compared to calculations from MC models and to results obtained in Pb–Pb and p–Pb collisions at the LHC.

References

[1] **Particle Data Group** Collaboration, K. Olive *et al.*, "Review of Particle Physics," *Chin. Phys.* **C38** (2014) 090001.

[2] "TE-EPC-LPC LHC units,". `http://te-epc-lpc.web.cern.ch/te-epc-lpc/machines/lhc/general.stm`.

[3] **ALICE** Collaboration, K. e. a. Aamodt, "Alignment of the ALICE Inner Tracking System with cosmic-ray tracks," *JINST* **5** (2010) P03003.

[4] **ALICE** Collaboration, J. Adam *et al.*, "Multiplicity dependence of pion, kaon, proton and lambda production in p–Pb collisions at $\sqrt{s_{\rm NN}}$= 5.02 TeV," *Phys. Lett.* **B728** (2014) 25–38, `arXiv:1307.6796 [nucl-ex]`.

[5] **ALICE** Collaboration, J. Adam *et al.*, "Production of $\mathrm{K}^*(892)^0$ and $\phi(1020)$ in p–Pb collisions at $\sqrt{s_{\rm NN}}$= 5.02 TeV," *Eur. Phys. J.* **C76** (2016) 245, `arXiv:1601.7868 [nucl-ex]`.

[6] **ALICE** Collaboration, J. Adam *et al.*, "Multi-strange baryon production in p–Pb collisions at $\sqrt{s_{\rm NN}}$=5.02 TeV," *Phys. Lett.* **B758** (2016) 389–401, `arXiv:1512.07227 [nucl-ex]`.

[7] **ALICE** Collaboration, B. Abelev *et al.*, "Production of $\Sigma(1385)^{\pm}$ and $\Xi(1530)^0$ in proton-proton collisions at $\sqrt{s}$= 7 TeV," *Eur. Phys. J.* **C75** (2015) 1, `arXiv:1406.3206 [nucl-ex]`.

[8] **ALICE** Collaboration, J. Adam *et al.*, "D-meson production in p–Pb collisions at $\sqrt{s_{\rm NN}}$= 5.02 TeV and in pp collisions at $\sqrt{s}$= 7 TeV," *Phys. Rev. C* **94** (2016) 054908, `arXiv:1605.07569 [nucl-ex]`.

[9] **ALICE** Collaboration, B. Abelev *et al.*, "Inclusive J/ψ production in pp collisions at $\sqrt{s}$= 2.76 TeV," *Phys. Lett.* **B718** (2012) 295–306, `arXiv:1203.3641 [hep-ex]`.

[10] **ALICE** Collaboration, J. Adam *et al.*, "Rapidity and transverse-momentum dependence of the inclusive J/ψ nuclear modification factor in p–Pb collisions at $\sqrt{s_{\rm NN}}$= 5.02 TeV," *JHEP* **06** (2015) 55, `arXiv:1503.07179 [nucl-ex]`.

[11] **ALICE** Collaboration, J. Adam *et al.*, "Measurement of pion, kaon and proton production in proton-proton collisions at $\sqrt{s}$ = 7 TeV," *Eur. Phys. J.* **C75** (2015) 226, `arXiv:1504.00024 [nucl-ex]`.

[12] F. Halzen and A. Martin, "Quarks and Leptons: an introductory course in modern particle physics," *By John Wiley and Sons* (1984) .

[13] S. Wheaton, J. Cleymans, and M. Hauer, "THERMUS: A Thermal model package for ROOT," *Comput. Phys. Commun.* **180** (2009) 84–106, `arXiv:hep-ph/0407174 [hep-ph]`.

[14] J. Cleymans, S. Kabana, I. Kraus, H. Oeschler, K. Redlich, and N. Sharma, "Antimatter production in proton-proton and heavy-ion collisions at ultrarelativistic energies," *Phys. Rev.* **C84** (2011) 054916, `arXiv:1105.3719 [hep-ph]`.

[15] S. O. T. P. K. W. H.J. Drescher, M. Hladik, "Parton-Based Gribov-Regge Theory," *Phys. Rept.* **350** (2001) 93–289, `hep-ph/0007198`.

[16] T. P. M. B. K. M. K. Werner, Iu. Karpenko, "Event-by-event simulation of the three-dimensional hydrodynamic evolution from flux tube initial conditions in ultrarelativistic heavy ion collisions," *Phys. Rev.* **C82** (2010) 044904.

[17] I. K. T. P. K. Werner, B. Guiot, "Analyzing radial flow features in p-Pb and p-p collisions at several TeV by studying identified-particle production with the event generator EPOS3," *Phys. Rev.* **C89** (2014) 064903.

[18] K. Werner., "Analyzing radial flow features in p-Pb and p-p collisions at several TeV by studying identified-particle production with the event generator EPOS3," *Phys. Rev. Lett.* **98** (2007) 152301.

[19] S. B. et al., "Microscopic Models for Ultrarelativistic Heavy Ion Collisions," *Prog. Part. Nucl. Phys.* **41** (1998) 255.

[20] M. B. et al., "Relativistic Hadron-Hadron Collisions in the Ultra-Relativistic Quantum Molecular Dynamics Model," *J. Phys.* **G25** (1999) 1859–1896.

[21] M. Gell-Mann and Y. Ne'eman, "The Eightfold Way," *By W.A. Benjamin* (1964) .

[22] J. Rafelski and B. Mller, "Strangeness Production in the Quark-Gluon Plasma," *Phys. Rev. Lett* **48** (1982) 1066–1069.

[23] **ALICE** Collaboration, B. Abelev *et al.*, "Multi-strange baryon production at mid-rapidity in Pb–Pb collisions at $\sqrt{s_{\rm NN}}$= 2.76 TeV," *Phys. Lett.* **B728** (2014) 216–227, `arXiv:1307.5543 [nucl-ex]`.

[24] L. Evans and P. Bryant, "LHC Machine," *JINST* **3** (2008) S08001.

[25] "ALICE Technical Proposal," *In CERN-LHCC-95-71* (1995) .

[26] "ATLAS Technical Proposal," *In CERN-LHCC-94-43* (1994) .

[27] "CMS Technical Proposal," *In CERN-LHCC-94-38* (1994) .

[28] "LHCb Technical Proposal," *In CERN-LHCC-98-004* (1998) .

[29] "Technical Proposal for CERN LHCf Experiment," *In CERN-LHCC-05-032* (2005) .

[30] "Total Cross Section, Elastic Scattering and Diffraction Dissociation at the LHC," *In CERN-LHCC-99-007* (1999) .

[31] **ALICE** Collaboration, K. Aamodt *et al.*, "The ALICE experiment at the CERN LHC," *JINST* **3** (2008) S08002.

[32] **ALICE** Collaboration, L. B. et al, "Definition of the ALICE coordinate system and basic rules for sub-detector components numbering," *In Internal Note ALICE-INT-2003-038* (2003) .

[33] **ALICE** Collaboration, J. e. a. Alme, "The ALICE TPC, a large 3-dimensional tracking device with fast readout for ultra-high multiplicity events," *In Nuclear Instruments and Method in Physics Research* **A622** (2010) 316–367.

[34] "Technical Design Report on Forward Detectors: FMD, T0 and VZERO," *In CERN-LHCC-2004-025* (2004) .

[35] R. Glauber, "Lectures in Theoretical Physics," *By Interscience Publishers.* **1** (1959) 315.

[36] A. S. K.C. Chung, C.S. Whang and G. Pech, "Transverse and forward energy distributions in untra-relativistic heavy-ion collisions by an absorption model," *Physics Review* **C57** (1998) 847–856.

[37] **ALICE** Collaboration, J. Adam *et al.*, "Centrality dependence of particle production in p–Pb collisions at $\sqrt{s_{\rm NN}}$= 5.02 TeV," *Phys. Rev.* **C91** (2015) 064905, `arXiv:1412.6828 [nucl-ex]`.

[38] **ALICE** Collaboration, B. Abelev *et al.*, "Centrality determination of Pb–Pb collisions at $\sqrt{s_{\rm NN}}$= 2.76 TeV with ALICE," *Phys. Rev.* **C88** (2013) , `arXiv:1303.0737 [nucl-ex]`.

[39] "ALICE Technical Design Report of the Trigger, Data Acquisition, High-Level Trigger, Control system," *In CERN-LHCC-2003-062.* (2003) .

[40] "The Grid - Blueprint for a New Computing Infrastructure," *By Morgan Kaufmann Publishers.* (1999) .

[41] e. a. Bagnasco. S, "AliEn: ALICE Environment on the GRID," *In Jounal of Physics: Conference Series* **119** (2008) n.062012.

[42] R. Brun and F. Rademakers, "ROOT - An object oriented data analysis framework," *In Nuclear Instrument and Methods in Physics Research Section* **A 389** (1997) 81–86.

[43] **ALICE** Collaboration, B. Abelev *et al.*, "Performance of the ALICE Experiment at the CERN LHC," *Int. J. Mod. Phys.* **A29** (2014) 1430044, `arXiv:1402.4476 [nucl-ex]`.

[44] **ALICE** Collaboration, B. Abelev *et al.*, "Pseudorapidity Density of Charged Particles in p–Pb Collisions at $\sqrt{s_{\rm NN}}$= 5.02 TeV," *Phys. Rev. Lett.* **110** (2013) 032301, `arXiv:1210.3615 [nucl-ex]`.

[45] **ALICE** Collaboration, K. Aamodt *et al.*, "Strange particle production in proton-proton collisions at $\sqrt{s}$= 0.9 TeV with ALICE at the LHC," *Eur. Phys. J.* **C71** (2011) 1594, `arXiv:1012.3257 [nucl-ex]`.

[46] S. Roesler, R. Engel, , and J. Ranft, "The Monte Carlo Event Generator DPMJET-III, Advanced Monte Carlo for Radiation Physics, Particle Transport Simulation and Applications," *Conference Proceedings, MC2000, Lisbon, Portugal, October 23-26* (2000) 1033–1038, `hep-ph/0012252`.

[47] R. Brun, F. Carminati, and S. Giani, "GEANT detector description and simulation tool," *CERN-W5013* (1994) .

[48] R. Barlow, "Systematic Errors: Facts and Fictions," *Presented at Advanced Statistical Techniques in HEP, Durham, March 2002* (2002) 333p, `hep-ex/0207026v1`.

[49] **ALICE** Collaboration, B. Abelev *et al.*, "Centrality dependence of π, K and p production in Pb–Pb collisions at $\sqrt{s_{\rm NN}}$= 2.76 TeV," *Phys. Rev.* **C88** (2013) , `arXiv:1301.4361 [nucl-ex]`.

[50] **STAR** Collaboration, B. I. Abelev *et al.*, "Hadronic resonance production in d–Au collisions at $\sqrt{s_{\rm NN}}$= 200 GeV measured at the BNL Relativistic Heavy-Ion Collider," *Phys. Rev.* **C78** (2008) 044906, `arXiv:0801.0450 [nucl-ex]`.

[51] A. Velásquez, "Mean $p_{\rm T}$scaling with $\rm m/n_q$ at the LHC: Absence of (hydro) flow in small systems?," *Nucl. Phys.* **A943** (2015) 9–17, `arXiv:1506.00584 [hep-ph]`.

[52] **ALICE** Collaboration, B. Abelev *et al.*, "Multi-strange baryon production in pp collisions at $\sqrt{s}$= 7 TeV with ALICE," *Phys. Lett.* **B712** (2012) 309, `arXiv:1204.0282 [nucl-ex]`.

[53] T. Sjöstrand, S. Mrenna, and P. Skands, "A brief introduction to PYTHIA 8.1," *Comput. Phys. Comm.* **178** (2008) 852–867, `arXiv:0710.3820 [hep-ph]`.

Acknowledgements